UNIVERSITY OF CALIFORNIA SAN DIEGO

Fiber optic based platforms for chemical and nanomechanical sensing

A dissertation submitted in partial satisfaction of the
requirements for the degree of Doctor of Philosophy

in

Materials Science and Engineering

by

Yuesong Shi

Committee in charge:

Professor Donald Sirbuly, Chair
Professor Adam Engler
Professor James Friend
Professor Ratnesh Lal
Professor Liangfang Zhang

2020

The Dissertation of Yuesong Shi is approved, and it is acceptable in quality and form for publication on microfilm and electronically:

Chair

University of California San Diego

2020

TABLE OF CONTENTS

LIST OF FIGURES

LIST OF TABLES

ACKNOWLEDGEMENTS

First of all, I would like to thank my advisor, Professor Donald Sirbuly, for granting me this great opportunity for my PhD, his constant support, his patient and continual audience. His guidance made this dissertation possible and my deepest appreciation to him for the trust he held for me that always motivate me to push forward during difficult times. Besides my advisor, I would like to thank the rest of my thesis committee: Prof. James Friend, Prof. Liangfang Zhang, Prof. Ratnesh Lal, and Prof. Adam Engler, for their insightful comments.

I would like show my special appreciation to all of my colleagues and former members in the Sirbuly lab, Dr. Qian Huang, Dr. Josh Villanueva, Dr. Spencer Ward, Dr. Conor Riley, Jamie Middlebrook and Beril Polat. I would also like to show special appreciation to Professor Jesse Jokerst for his support in my final year and guidance on the heparin project. Finally, I would like to thank my parents, my grandmother, and dear friends for their constant support and love. Thank you all for keeping me sane through this journey.

Chapter 2, in part, is a reprint of the material ”Nanoscale fiber-optic force sensors for mechanical probing at the molecular and cellular level” as it appears in Nature Protocol, Yuesong Shi, Beril Polat, Qian Huang, and Donald J. Sirbuly, 2018, 13, 2714-2739. The dissertation author was the primary investigator and author of this material.

Chapter 3, in part, is a being prepared for submission of the material ”Multifunctional microfiber based electrochemical, optical and spectroelectrochemical sensor” with authors of Yuesong Shi, Spencer Ward, Conor Riley, and Donald J. Sirbuly. The dissertation author is the primary investigator and author of this material.

VITA

2010-2014 B. S. in Materials Science and Engineering, Chengdu University of Technology

2014-2015 M. S in Materials Science and Engineering, University of California San Diego

2015-2020 Ph. D. in Materials Science and Engineering, University of California San Diego

PUBLICATIONS

Y. Shi, S. Ward, C.Riley, DJ. Sirbuly, "Multifunctional microfiber based electrochemical, optical and spectroelectrochemical sensor" *in preparation*

Y. Shi, B. Polat, Q. Huang, DJ. Sirbuly, "Nanoscale fiber-optic force sensors for mechanical probing at the molecular and cellular level" *Nature protocols*, 2018, 1.

F. Chen, ER. Zhao, T. Hu, **Y. Shi**, DJ. Sirbuly, JV. Jokerst, "Silicon carbide nanoparticles as a photoacoustic and photoluminescent dual-imaging contrast agent for long-term cell tracking", *Nanoscale Advances*, 2019, 1(9): 3514-3520.

Yen. TM, F. Xin, W. Tao, N. Roshan, **Y. Shi**, YH. Lo. "Reversing Coffee-ring Effect by Laser-induced Differential Evaporation", *Scientific Reports*, 2018, 8, 3157-3157

J. Wang, S. Wagner, W. Chen, **Y. Shi**, A. Ndao, L.Li, B. Kante, DJ. Sirbuly, M. C.Lemme, Vazquez Mena, "Integration of nanomaterials into three- dimensional vertical architectures", *ACS applied materials interfaces*, 2018, 10(34), 28262-28268.

Q. Huang, J. Lee. F. Arce, I. Yoon, P. Angsantikul, J. Liu, **Y. Shi**, J. Villaneuva, S. Thamphiwatana, X. Ma, L. Zhang, S. Chen, R. Lal, DJ. Sirbuly, "Nanofiber optic force transducers with sub-piconewton resolution via near-field plasmon-dielectric interactions", *Nature Photonics*, 2017, 11, 352-357.

Y. Chiu, W. Cai, **Y. Shi**, YH. Lo. "A self-confined single-cell loading platform combining PDMS mesh and patterned Cytop for non-invasive studies of single cell secretions", *2016 IEEE 16th International Conference on. IEEE*, 2016.

ABSTRACT OF THE DISSERTATION

Fiber optic based platforms for chemical and nanomechanical sensing

by

Yuesong Shi

Doctor of Philosophy in Materials Science and Engineering

University of California San Diego, 2020

Professor Donald Sirbuly, Chair

There has been a rising desire for miniaturized sensing platforms for biomedical point-of-care applications. Optical microfiber and nanofibers have drawn great attention in such fields due to their unique light-guiding property and a versatile structure for constructing miniaturized devices. The flexibility and a small footprint of the micro/nano optical fibers allow them to be easily engineered for various sensing platforms with the ultrasensitive modality. One such modality can be achieved through the highly localized optical near-field of a nanofiber with a subwavelength dimension. On the other hand, microfibers with flexible nature yield an adaptable platform that can be easily integrated with other sensing modalities leads to highly localized multifunctional microdevices. In this dissertation, I introduced three fiber optic-

based sensing platforms as a compact solution for biomedical applications. We demonstrated ultrasensitive nanomechanical sensing harnessing the sharp decaying optical field outside a nano-fiber optic; a miniaturized multifunctional electro-optic device for neurotransmitter detection; and a microfiber based electrochemical sensor for anticoagulant drug detection. The proposed device architecture, design, engineering solution for device integration of the fiber-based sensing platforms could provide new directions for future research in miniaturized biomedical sensing technologies.

Chapter 1

Introduction

1.1 Optical fiber-based sensing platforms

1.1.1 Background on Optical waveguides and evanescent field

Optical fiber is at the heart of optical communication system. The ability of guiding light is due to the phenomenon of total internal reflection (TIR). When the ray is incident at the interface of two media with certain incidence angel, there would be no refracted ray and we get total internal reflection. This angle is defined as the critical angel governed by the Equation 1.1

$$\Theta_c = \sin^{-1}\left(\frac{n_2}{n_1}\right) \tag{1.1}$$

Light travelling along the fiber optic due to TIR can also be described as a set of guided electromagnetic (EM) waves called the modes of the waveguide. Each mode is a certain pattern of electric and magnetic field distribution that could satisfy the Maxwell equation, and only a certain number of modes are allowed to propagate along the waveguide [1]. The guided EM wave is consisting of two components: 1) the guided field in the optical core and 2) the exponentially decaying evanescent field in the cladding. **Figure 1.1** shows the field patterns of some lower-order modes and it is clear that the guided modes are not completely confined to the core but extend into the cladding layer with a decaying power. For zeroth order mode, the fields are tightly confined within the core, while for higher order modes, the fields are

distributed toward the edges.

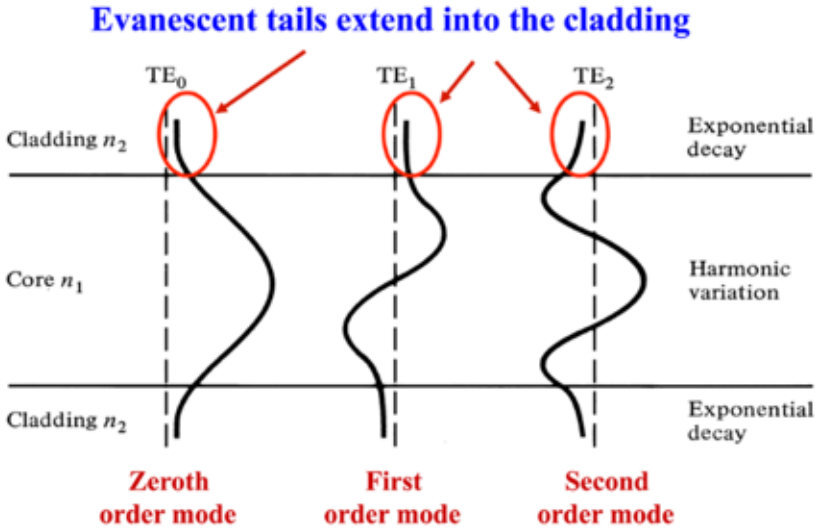

Figure 1.1. Electric field distributions of lower-order guided modes in an optical fiber [1].

Depending on the number of modes that are allowed to propagate along the optical fiber, optical fiber can also be classified into single mode fiber (SMF) and multimode fiber (MMF). In SMF, only the fundamental mode can propagate along the waveguide. V-number is an important parameter to estimate the cutoff condition which is defined by Equation 1.2

$$V = \frac{2\pi}{\lambda_0} a \sqrt{n_1^2 - n_2^2} = \frac{2}{\lambda_0} NA \tag{1.2}$$

Where $n_1$is the refractive index of the core, n_2 is the refractive index of the cladding, a is the core radius and λ_0 is the guided light wavelength. The V-number determines the number of modes that an optical fiber can support and when V <2.405, only one guided mode, the fundamental mode is supported in the waveguide. For the propagated light that extends into the cladding region, the penetration depth d_p describes the distance where the field decrease to 1/e of its value at the core-cladding interface and the evanescent field is described as Equation 1.3

and 1.4

$$E(x) = E_0 \exp(\frac{-x}{d_p}) \tag{1.3}$$

$$d_p = \frac{\lambda}{2\pi\sqrt{n_1^2 \sin^2\theta - n_2^2}} \tag{1.4}$$

1.1.2 Fiber-optic evanescent sensor

Fiber optic evanescent wave (FOEW) sensors utilize evanescent field to sense perturbations in the evanescent filed of the guided modes. A major advantage of these sensors stems from the near-surface nature of the evanescent field excitation, which makes them surface sensitive and help minimized unwanted background signal from a bulk sample. In conventional glass fiber optics, cladding was removed uniformly over a distance to expose the evanescent field to the sensing medium, however the penetration depth is usually too small for sensing. Several works have then been done to increase the penetration depth of the evanescent field and to facilitate mode coupling by tapering [2], bending [3] and changing light launching angle [4]. FOEW platforms based on different detection mechanism have been applied in various chemical and biological sensing applications. In general, FOEW sensors falls into three categories: 1) Absorption based sensor, 2) Fluorescence based sensor, 3) Surface plasmon resonance (SPR) based sensor. In absorption-based FOEW sensors, the power of propagating field depends on the refractive index difference between the core and the sensing medium. Analyte captured or absorbed on the fiber optic surface would change the effective refractive index of the fiber coating, and thus change the power level in the core. This method has been developed for various applications in biosensing and environmental engineering such as glucose sensing [5], PH sensing [6, 7] and gas sensing. Similar to absorption based FOEW, fluorescent-based sensors utilize the evanescent field to excite fluorescent tags attached on the surface and various fluorescence immunoassay [8] and DNA arrays [9] have been developed.

In fiber optic SPR sensors, instead of having the evanescent field to interact with the sample directly, a metal layer coating on the dielectric waveguide was applied to excite surface plasmon waves. When the surface resonance condition is satisfied, surface plasmons excitation at the metal/dielectric interface yields the energy transfer from incident light to surface plasmon and further reduce the intensity of reflected light [10]. Transmitted light is then detected to obtain the SPR spectrum, usually with a dip at the resonance angel or wavelength. This resonance condition is highly dependent on the angle of incidence, wavelength of the incident light, and the materials property of the metal layer coating, so any change in the refractive index would change the resonance condition and could be detected from the SPR spectrum to register analyte binding. SPR based fiber optic sensors have demonstrated large number of applications in protein detection [11], temperature sensing [12, 13], and gas sensing [14].

1.1.3 Fiber optic interferometery-based sensing

Fiber optic interferometry is based on light interference, where two beams of light launched from the same source propagate through space with different optical path, that result in light intensity varying periodically. Thus, very small change in optical path difference can lead to measurable signal change in the intensity of the interference light. Various configurations of fiber optic interferometer sensor has been developed with different operation principles, such as the Fabry-Perot interferometer (FPI) probe, Mach-Zehnder probe, Sagnac probe, and Michelson probe [15]. FPI sensor is generally consist of two parallel reflecting surfaces separated by a distance and interference occur due to superposition of the reflected and transmitted light at the parallel surfaces. Extrinsic FPI sensors use an external cavity formed outside of the fiber, while intrinsic FPI have the reflecting components within the fiber itself as shown in **Figure 1.2**.

Fiber Bragg gratings (FBG) sensor is a widely used type of intrinsic FPI sensor that has been applied to strain and pressure sensing. FBG gratings are obtained through creating periodic pattern in the refractive index of the fiber optic core. When light propagates through

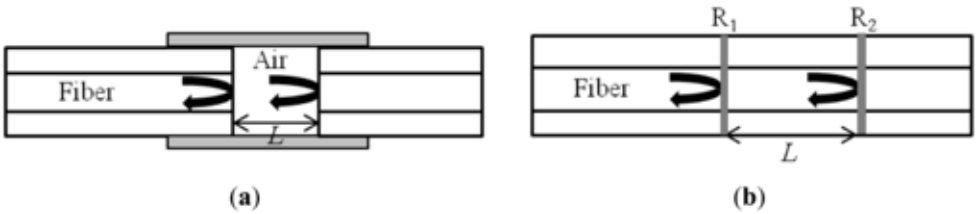

Figure 1.2. (a) Extrinsic FPI sensor with external air cavity. (b) Intrinsic FPI sensor with two reflecting components within the fiber [15].

.

an FBG and satisfies the Bragg condition (Equation 1.5), reflections from each period will be in phase and when light does not satisfy the condition, it would pass through the FBG. and the operating mechanism is shown in **Figure 1.3**.

$$\lambda_B = 2n_{eff}\Lambda \tag{1.5}$$

Where λ_B is the Bragg wavelength, n_{eff} is the effective refractive index of the fiber core and Λ is the grating period. Through monitoring the wavelength shift of the transmitted light, any change of n_{eff} or Λ could be monitored. Fiber FBG sensor has been used widely for tracking physical parameters change, especially as a strain sensor, pressure sensor and temperature sensor.

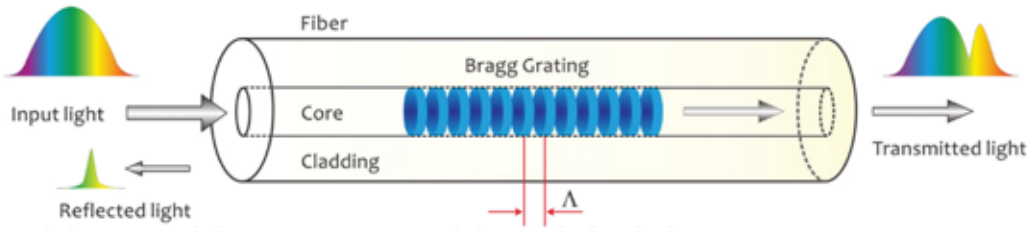

Figure 1.3. Structure of fiber Bragg grating sensor [16].

1.1.4 Fiber optic spectroscopic sensing

Spectroscopy is a powerful tool to interrogate the materials characteristics. On the other hand, optical fibers provide a highly flexible support to deliver light to sample medium and can also be used in a feedback mode to collect light that is reflected, scattered or fluorescently emitted from the sample. Combining the spectroscopic methodologies with the fiber optics offer the detection system with rapid, noninvasive and remote sensing capabilities. Numerous spectroscopic methods have been demonstrated using fiber optic such as fluorescence spectroscopy, elastic scattering spectroscopy (ESS), and diffuse correlation spectroscopy (DCS). In ESS, light hit the tissue components and scattered without changing the energy. The transport mean free path (MFP) of a photon in a turbid media can be described as the following [17]:

$$MFP' = \frac{1}{\mu_a + \mu_s'} \tag{1.6}$$

where μ_a is the absorption coefficient and μ_s' is the reduced scattering coefficient. These parameters are highly dependent on the chemical and structural composition of the tissue sample, which can be acquired in the time domain and frequency domain through reflectance measurements. Usually, reflectance profiles are measured at 6 ~ 9 separated locations, either in a linearly arranged arrays or a circular arrangement [17]. Fiber optic ESS has been extensively used as a minimally invasive diagnostic tool to discriminate normal and abnormal human tissues *in vivo* [18, 19, 20]. Alternatively, DCS uses time-averaged intensity autocorrelation function of a fluctuating light signal to probe the blood flow variations in deep tissue microvasculature. It is usually operated in the NIR range with low tissue absorption for deep penetration. DCS has been used to understand the cerebral physiology of newborn's brains through measuring the hemoglobin concentration, cerebral blood flow [21].

Fiber optic fluorescent sensor has been an essential component in a variety of clinical situations. Even though single-fiber solution is desired with a small diameter, it is still limited

due to the difficulty in reducing back scattered excitation and illumination source at the interface. The multi-fiber probe is usually used for fluorescent imaging. One method is to couple the excitation light source to one arm of a bifurcated fiber bundle and couple the other arm to the spectrometer for emission light collection. Another common method is to use a fiber bundle with the central optical fiber for excitation delivery and the surrounding coaxial fibers for emission light collection. Miniature fiber optic spectrophotometric instrumentation has shown great promise for *in vivo* fluorescent imaging and detection. An early work by Lo et al. demonstrated an needle-type fiber optic probe can be used as an implantable device for continuously monitoring the extravasation of pre-administered fluorescent nanospheres in an anesthetized mice [22]. MMF based endoscope has also been demonstrated for deep brain fluorescence imaging (**Figure 1.4**). Wave-front shaping was used to modulate the light at the proximal side of the fiber and it generate micro-scale spot at the distal side to excite certain fluorescent proteins. The emission could then be collected with the same fiber and image was generated through raster scanning [23].

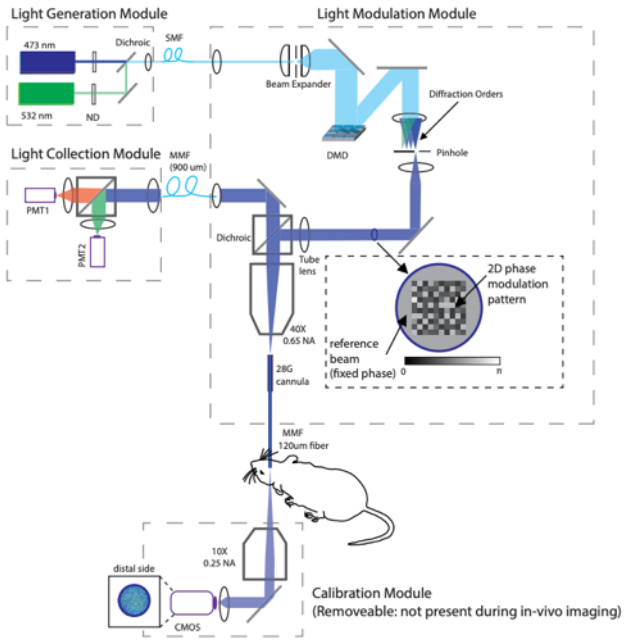

Figure 1.4. Optical system design for deep brain fluorescence imaging using MMF probe [23].

1.2 Nanowire photonics-based sensing platforms

Nanowire photonics, or nanofibers are subwavelength waveguides that have a relatively large aspect ratio and cross-sectional dimensions usually within 2-200 nm [24]. It has drawn great attentions due to its ability to guide tightly confined field in single mode which can be useful in manipulating electrons, photons, and plasmons [24]. With a subwavelength dimension, a nanowire can guide light with a large portion of the power in the evanescent field which allows numerous near-filed interactions of the light with the surrounding medium (**Figure 1.5**). The strong evanescent field enables evanescent coupling between nanofiber and other waveguide structures, and offers a steep optical gradient force for manipulating micro-particles [25]. Besides, due to the very low mass of the free-standing nanowire, the momentum change of the guided light could also induce mechanical movement that can be applied in versatile optomechanical devices [26].

Depending on the type of materials, nanowire photonics can be categorized into two major classes: dielectric nanowire with amorphous structure (e.g., glass, polymer), or semiconductor with crystalline structure (e.g., ZnO, CdS). For the dielectric nanowires, the top-down flame-heated taper drawing method has been widely applied to draw silica nanowire from standard optical fiber with diameter down to few nanometers [27]. In a similar approach, a variety of polymer nanofiber of polystyrene (PS), poly(methyl methacrylate) (PMMA), poly(vinyl alcohol) (PVA), poly(ethylene oxide) (PEO) have also been fabricated with high uniformity through direct drawing from the solvated polymers [28, 29]. Bottom-up chemical synthesis such as 'vapor-liquid-solid' (VLS) growth or chemical vapor transport method are heavily used to create semiconductor nanowires [30]. This fabrication method can grow a large batch of nanowires at one time with controllable parameters through tailoring the bandgap structure and geometry [24].

The motivation towards optical nanofiber sensors stem from an increasing demand on miniaturized sensing platforms at nanoscale. The small dimension of the nanowire sensors

offers high spatial resolution, low sample volume requirement, and a small footprint. The small diameter below the wavelength of the guided light also enables ultrasensitive detection. Various optic nanowire-based sensing platforms have been developed for humidity detection [31], gas sensing [32], flow sensing [33].

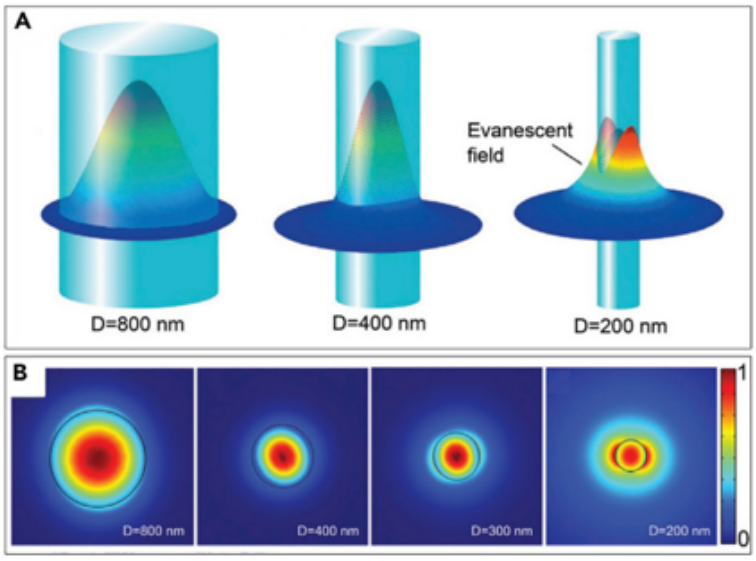

Figure 1.5. Spatial distribution of the optical field guided by silica nanowire with diameter of 800, 400, 200 nm in (a) 3D view and (b) in 2D view [29].

1.3 Fiber optic spectroelectrochemistry

Spectroelectrochemistry(SEC) is the combination of electrochemistry and spectroscopy that allows complete analysis of complex electron transfer process and redox reactions [34]. During SEC measurement, the spectroscopic response is monitored *in situ* while the electrochemical reaction is carried out simultaneously under controlled conditions. In general, the measurements were carried out using the optically transparent electrodes (OTE) to measure the absorbance signal. Two major types of OTE that has been applied are conductive thin film such as indium-tin oxide (ITO) and the mesh metal electrodes such as Au and Pt [35].

Electrochemistry by itself has been utilized to determine the concentration of known

compounds or to elucidate the reaction kinetics. However, it is less suitable for detecting unknown species. Supplementing electrochemical techniques with complementary measurements like spectroscopy imposes several advantages for the sensing platform [36]. First of all, these two types of information are not simply adding together, it also provides synergistic effect between optical and electrical signal that elucidate complex electron transfer process. Besides, obtaining time-resolved spectroscopic information is fundamental to understand many complex redox reactions [37]. Moreover, the combined platform enables higher sensitivity. For example, UV/vis spectroscopy is usually less sensitive than electrochemistry, while combined with other technique the performance could be enhanced since applied potential could preconcentrate analyte on the surface to improve the optical signal and further increase its sensitivity [38]. Third, simultaneously multimodal data acquisition increases the selectivity of the measurement. Through careful selection of specific wavelength for absorption and specific applied potential window for electrochemical reaction, direct interference could be excluded during SEC measurements. Utilizing ion-exchange film on the electrode also offers the third mode for selective chemical sensing from a test mixture, since the analyte would only be registered when it absorbs light at the selected wavelength, has certain redox potential, and carries certain charge for preconcentration on the electrode surface [39, 40]. Additionally, spectral signal is not affected by non-faradaic currents which offers higher sensitivity at situations where the capacitive current is too high that reduce the electrochemical sensitivity [38].

Fiber optic SEC devices offer many advantages as the remote sensing and real-time measurement capability and various configurations for the SEC cell has been developed. Usually, a side polished microfiber with metal deposition was used and the attenuated total reflection (ATR) during a redox reaction was monitored. Imai et al. used a gold mesh covered multimode silica fiber with cladding removed as the working electrode for spectroelectrochemical sensing [41]. Beam et al. used a side polished multimode fiber optic coated with ITO as the working electrode to probe the spectroelectrochemistry of PEDOT [42]. Fiber optic can also be applied

in a thin-layer configuration where the optical path is in parallel with the electrode [43]. While this approach has been challenging due to the difficulty in optical alignment and it could only acquire information in the diffusion layer. Fiber bundle has also been used as a reflective probe for both light delivery and measurement, which avoids the requirement of using an OTE as the working electrode [44].

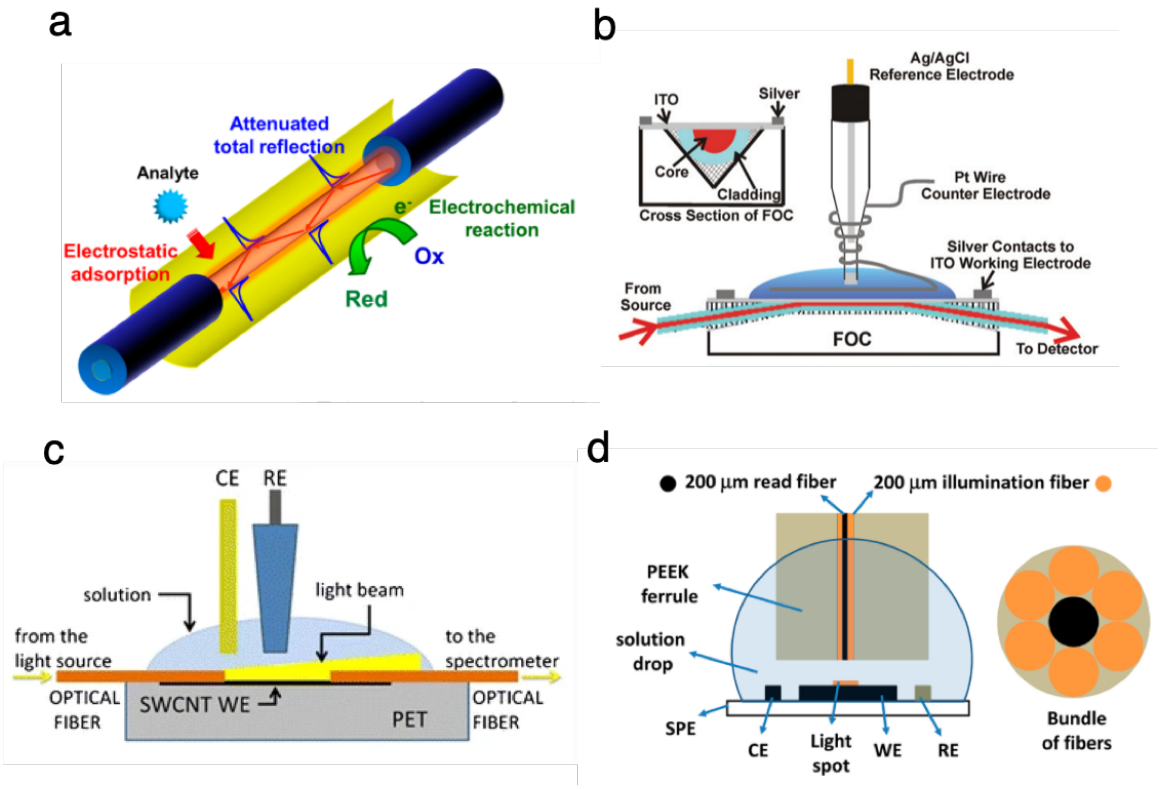

Figure 1.6. (a) Schematic setup for the fiber-optic SEC sensor using gold mesh covered multimode fiber [41]. (b) Schematic setup for side polished fiber-optic coated with ITO [42]. (c) Schematic setup for fiber-optic SEC with optical path in parallel with the electrode [43]. (d) Schematic setup for fiber-optic SEC in normal reflection mode [44].

1.4 Outline of the thesis

Fiber optic waveguides and nanowire photonics offer a versatile platform with small footprint, which is highly suitable to interface with the biological system. The unique optical and mechanical properties provide various sensing modalities that could be integrated with other system as well. This disseration details three sensing platforms using optical waveguides of different dimensions for nanomechanical or chemical sensing.

In Chapter 2, I describe the design, structure and the sensing mechanism of a nanofiber optic force transducer using SnO_2 nanofiber. The designed transducer is based on a thin layer of compressible polymer layer grafted in the near field of the SnO_2 nanofiber. Using gold nanoparticles as the optical transmitter and compressible polymer cladding as a pseudo-spring, the strong plasmonic-dielectric coupling in the evanescent field renders strong distance dependent far-field scattering which can be converted to a unit of force. We've characterized the mechanical property of the polymer thin film through AFM nanoindentation in order to quantify the force response. Using this nanofiber optic force transducer, we were able to capture acoustic wave of ˜ 163 pW.

In Chapter 3, I describe a microfiber based electro-optical microprobe that could carry out multimodal measurements of both electrochemical detection of neurotransmitters as well as localized spectroscopy reading. The microprobe is constructed on a coaxial structure containing a silica micro fiber core as the optical channel, and platinum coating as the electrical channel. A conductive polymer coating was applied to improve the electrochemical sensing capability. The dual modality of the microprobe was demonstrated with a study on the electrochromic behaviour of redox active materials.

In Chapter 4, I describe the initial work on a microfiber optic based electrochemical sensor for heparin detection. The electrochemical response of various cationic dyes and heparin interaction was first evaluated. Then, different dye immobilization strategy on the microfiber electrode was investigated and discussed.

Chapter 2

Nanofiber optic platform for nanomechanical detection

There is an ongoing need to develop ultrasensitive nanomechanical instrumentation that has high spatial and force resolution, as well as an ability to operate in various biological environments. In this chapter, we introduce the design and operation mechanism of a compact nanofiber optic force transducer (NOFT) that paves the way to the probing of complex mechanical phenomena inside biomolecular systems. The NOFT platform comprises a SnO_2 nanofiber optic equipped with a thin, compressible polymer cladding layer studded with plasmonic nanoparticles (NPs). This combination allows angstrom-level movements of the NPs to be quantified by tracking the optical scattering of the NPs as they interact with the near-field of the fiber. We've demonstrated the nanomechanical sensing capability of the proposed platform for acoustic wave detection.

2.1 Nanofiber optic platform introduction

2.1.1 Background and motivation

Underlying most biological processes exist unique nano-biomechanical events that help drive reactions and guide chemical pathways. These small mechanical cues can be subtle and difficult to track, but they are an intricate part of environmental responses and sustaining life. With the continued advancement of ultrasensitive nanomechanical instruments, it has been an

ongoing goal to observe, measure and manipulate these mechanical processes in vitro or even in vivo in order to get a more complete understanding of biomechanical phenomena. Presently, it is possible to gain real-time information on systems that range from small sizes such as single molecules up to larger cellular structures and tissue; however, it remains challenging to scale down the size of the nanomechanical transducer due to mechanical feedback mechanisms and active components. Having a compact force transducer can open up countless capabilities including intracellular monitoring, minimally invasive probing, and high-resolution detection. Ideally, the transducer would be small enough to minimize inflammatory responses and at the same time have high resolution and the ability to simultaneously track multiple mechanical events. Equally important to size is the capacity to operate in different modes and detect various types of nanomechanical signatures. For example, in direct contact mode the transducer would be able to feel small forces acting on it, but it would also be advantageous to have a touchless mode where the transducer detects signals such as acoustic waves originating from a volume change or moving mass. To do this, the transducer would have to be engineered to interact with sound waves and produce a detectable signal above the noise level. The aforementioned wish list for novel ultrasensitive force transducers requires new approaches and innovative engineering.

Nanomechanical tools such as the atomic force microscope (AFM) [45, 46] and optical/magnetic traps [47, 48, 49] have been the work horse instruments for measuring nanoscale forces with high resolution. For example, state-of-the-art AFM platforms can now reach sensitivities below a piconewton and sampling throughput can be increased significantly using dynamic imaging modes. Whereas optical traps utilizing a single nanoparticle transducer have not only been shown to reach force sensitivities of a few femtonewtons [50, 51], but can also be designed to detect acoustic waves in solution with a sensitivity of – 60 dB [52]. Even though AFM systems use a micron scale cantilever equipped with a sharp nanometer-sized tip to detect nanomechanical events, and traps leverage beads (typically with micron sized diameters) to

locally measure forces and displacements, these platforms actually utilize similar strategies (e.g., optical scattering/interference) to gain feedback on the position and forces acting on the transducers. These mechanical feedback mechanisms, as well as the actual transducer itself, are typically much larger than the system being probed, which makes it difficult to carry out measurements inside the body or cell. Furthermore, the light sources required to trap and/or track the transducers can interfere with, or even damage, the biological specimen due to the high photon flux at the focal point. In addition to these methods, there have been advancements in other nanomechanical techniques which include needle manipulation, fluorescent biosensors [53, 54], biomembrane and molecular force probes [55, 56, 57], and fluid-based measurements. Although these strategies have been used to measure and observe single molecule events in complex biological systems, some of the challenges with these techniques include the ability to carry-out high-throughput studies within a small area and being able to detect other mechanical modes such as acoustic waves. The complex mechanical feedback mechanisms of these systems can also hinder their speed and limit real-time analysis *in vivo*.

2.1.2 NOFT system operation mechanism

This nanofiber optic force transducer (NOFT) platform is made possible by the strong distance-dependent scattering of plasmonic nanoparticles embedded in the near-field of the fiber [58]. Evanescent field near the optical nanofiber (100-500 nm in cross section and millimeters in length) is excited using a 325 nm laser coupled in free-space. A compressible cladding layer such as polyethylene glycol (PEG) or polyelectrolyte multilayers (PEM) can be grafted on the oxide surface of the nanofiber. 80 nm sensing gold NPs are covalently linked on top of the cladding layer that provides far-field optical readout under modulation. Reference gold NPs are linked electrostatically on bare nanofiber that act as a baseline for total guided power in the system. Mechanically compressible cladding layers between the sensing gold NP and the waveguide surface provide the mechanical resistance to movement which helps us monitor

forces/pressures within the environment. If the mechanical properties of the claddings are well characterized, and the scattering intensity is properly profiled as a function of distance, it is possible to convert the far-field scattering signals of the gold NPs to a unit of force. Nanomechanical measurements can be made via pure optical read-outs in the far-field while keeping a small transducer footprint and a fiber geometry that facilitates minimally invasive probing.

The working mechanism of the NOFT platform is based on Hookes' Law (**Figure 2.1a**) where a force acting on a spring can be extracted if the spring constant and displacement are known. The polymer cladding can be treated as a nonlinear spring that has an increasing spring constant as it becomes more compressed. The mass of the nanoparticle is too small to have gravimetric effects on the spring, so any force that causes the nanoparticle to move can be quantified by tracking the optical scattering signal and knowing the mechanical response of the compressible cladding. There are three critical components when building the NOFT platform that need to be well-understood and properly designed in order to back out quantitative nanomechanical data using the system: (1) the sharp decaying near-field of the optical waveguide, (2) the optical transmitter, and (3) the compressible cladding layer. The decaying near-field exposes objects outside of the waveguide to a different optical intensity depending on their distance from the waveguide surface and is used to excite the optical transmitter. The optical transmitter should provide a stable, distance-dependent optical signal when interacting with the near-field and should be easy to chemically functionalize so that it can be linked to the compressible cladding layer. The compressible cladding layer should be thin (< 20 nm) enough to be within the near-field, have a uniform thickness, and have tunable mechanical properties. The overall workflow for preparing the NOFT platform is illustrated in **Figure 2.1b**. In brief, the workflow comprised of the following steps: the SnO_2 waveguide synthesis; creation of a compressible polymer grafting layer; attachment of gold NPs; and far-field imaging, data acquisition, and analysis.

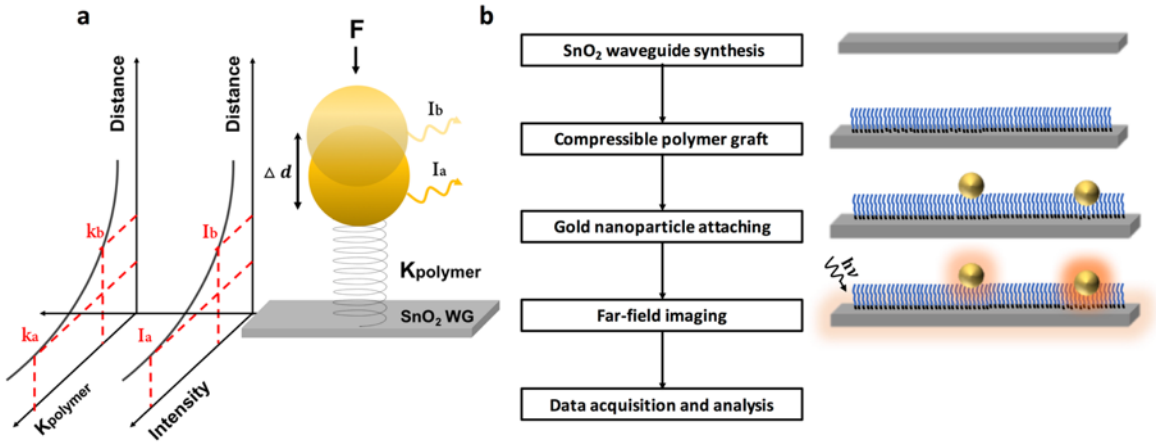

Figure 2.1. NOFT system overview. (a) Hooke's law can be used to model the response of the NOFT platform. The spring constant of the polymer cladding, as well as the scattering intensity of the NP, increase as the films are compressed. I_a, scattering intensity of the gold NP close to the WG surface; I_b, scattering intensity of the gold NP far from the surface; hv, UV excitation; $K_{polymer}$, spring constant of the polymer cladding at a given distance; WG, waveguide; K_a, spring constant of the polymer cladding when compressed; K_b, spring constant of the polymer cladding in an uncompressed state; Δd, change in distance of the gold NP; F, force acting on the gold NP. (b) Overall workflow for preparing a NOFT device.

2.1.3 SnO_2 nanofiber

Tin dioxide (SnO_2) nanofiber waveguides (WGs) were chosen for the NOFT platform since they have a wide band gap of 3.6 eV and a large refractive index (n = 2.1 in the visible) which allows passive waveguiding of wavelengths up to the band edge and strong confinement of the light in liquids, respectively [59]. The SnO_2 nanofibers are also single crystalline, growing along the $< 101 >$ direction of the rutile crystal structure with quasi-rectangular cross-sections ranging from 100 – 500 nm and lengths up to millimeters, which makes them mechanically flexible at the nanoscale. The nanofibers are synthesized using a chemical vapor transport method run at a temperature of 1000 °C [59, 60]. The nanofibers can be dry transferred to secondary substrates, including microfluidic chips with trenches to enhance surface area contact with the solution, via micromanipulation. To couple light into the nanofibers, an above band-edge laser source such as the 325 nm (3.8 eV) line from a continuous wave helium-

cadmium (HeCd) laser, is focused on one of the end facets of the nanofiber at an incident angle of 45° relative to the sample plane while the sample is positioned under the objective of an upright microscope. Due to the dipole-forbidden band edge transition in the SnO_2 crystal, only white defect emission (originating from crystal defects such as oxygen vacancies) is generated when excited by the ultraviolet light. The white light is trapped in the fiber and guided down to the opposing end facet which can be tracked and measured using the collection optics [61, 62].

2.1.4 Gold nanoparticle attachment and plasmon-dielectric coupling

The optical transmitter is a critical component for the force transduction mechanism as it provides the optical feedback necessary to correlate displacement with force. There are various options for the optical transmitter including quantum dots, fluorescent molecular species, but the stable light-matter interactions achieved with plasmonic NPs are preferred. This is because the collected far-field optical signals from the transmitters are directly related to the force acting on it and fluorescent molecules/quantum dots can show intermittent (i.e., blinking) optical signals and/or unstable fluorescence caused by photodegradation. In addition to providing stable optical signals, plasmonic NPs such as gold or silver show a strong plasmon-coupling which enhances the distance-dependent scattering intensity.

When a plasmonic NP is in close proximity to a dielectric surface and a plasmon is excited, the dipole formed in the metal induces a dipole in the dielectric. (**Figure 2.2**).

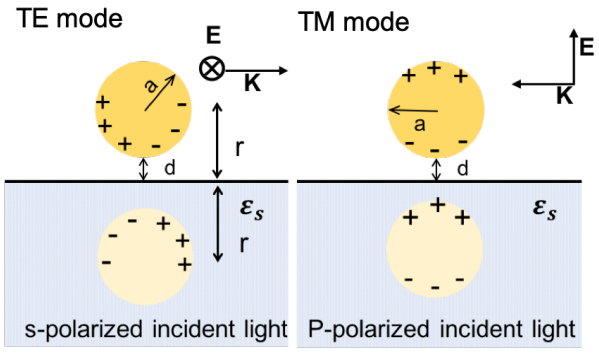

Figure 2.2. Coupling of probe dipole p and image dipole p' with perpendicular and parallel electric field E.

When E is perpendicular to the sample surface, the electric field of the induced dipole can be described as [63] :

$$E_{dipole}(r) = \frac{p}{2\pi r^3} \tag{2.1}$$

This electric field induces surface charges and can be descried by an image dipole with dipole moment of $p' = \beta p$, where $\beta = (\varepsilon - 1)/(\varepsilon + 1)$. The incident field is enhanced by this image dipole and the actual dipole moment becomes [63]:

$$p = \alpha\left(E + \frac{p'}{16\pi r^3}\right) = \frac{\alpha}{1 - \frac{\alpha\beta}{16\pi r^3}}E \tag{2.2}$$

The coupling of the dipoles results in a larger effective polarizability $|\alpha_{eff}|$ of the metal NP due to the superposition of both probe and image dipole with the expression as [63]:

$$\alpha_{\perp}^{eff} = \frac{\alpha(1+\beta)}{1 - \frac{\alpha\beta}{16\pi r^3}} \tag{2.3}$$

$$\alpha = 4\pi a^3(\varepsilon_p - 1)/(\varepsilon_p + 2) \tag{2.4}$$

where ε_p is the complex dielectric constant of the dielectric probe and this enhancement is non-negligible at short distances when d $\leq$a. When E is parallel to the sample surface, the

electric field of the induced dipole is:

$$E_{dipole}(r) = -\frac{p}{4\pi r^3} \tag{2.5}$$

The effective polarizability can then be expressed as:

$$\alpha_{\parallel}^{eff} = \frac{\alpha(1+\beta)}{1-\frac{\alpha\beta}{32\pi r^3}} \tag{2.6}$$

Mie theory states that the scattering cross-section of the NP is proportional to $|\alpha_{eff}|^2$, so the enhanced effective polarizability significantly enhanced the optical scattering.

$$C_{sca} = \frac{k^4}{6\pi}|\alpha_{eff}|^2 \tag{2.7}$$

This coupling component adds to the exponentially decaying optical intensity of the near-field and produces a strong distant-dependent scattering. There are various approaches to experimentally profile the NP scattering intensity as a function of distance. Previously in our lab, we have used polyelectrolyte coatings to controllable separate the NP from the waveguide surface, and we have utilized NP-terminated AFM tips to precisely move the NP within the near-field [62, 64]. Both experiments and simulations [e.g., finite-difference time-domain (FDTD)] confirm the strong distant-dependent scattering of gold NPs near a SnO_2 surface (**Figure 2.3a**). In fact, the combination of the decaying evanescent field and the plasmon-dielectric coupling effects boosts the sensitivity of spatially monitored NPs by ~ 10x and allows angstrom-level separation changes between the NP and WG to be tracked. For parallel polarization, the original dipole and the image dipole are antiparallel so they nearly cancel in the total scattering on the gold NP, so the TM mode excitation in the SnO_2 nanofiber produce the dominant scattering signal on the nanofiber. The primary optical transmitters used in the initial NOFT system were 80 nm gold NPs given their strong optical resonances at ~ 570 nm and simple chemistries

available to attach the NPs to the waveguide. However, the platform is general and other plasmonic NPs such as silver can be used. On each NOFT, there should be ideally 2-3 reference nanoparticles attached directly to the SnO_2 surface and multiple sensing nanoparticles are linked to the compressible cladding (**Figure 2.3b**). The reference nanoparticles are attached to the waveguide electrostatically (via amine functionalization of the SnO_2) prior to depositing the compressible cladding and serves as a baseline for the guided power (allows any laser fluctuations to be removed from the collected scattering data). After depositing the polymer cladding, the sensing nanoparticles are covalently or electrostaticlly linked to the polymer cladding.

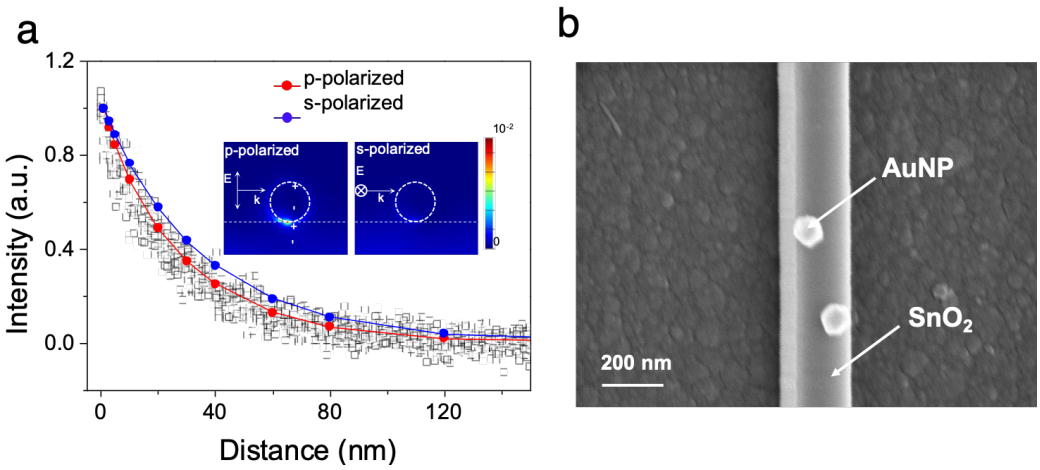

Figure 2.3. (a) Experimental and simulated gold NP scattering intensity decays verse distance using a NP-terminated AFM tip [64]. (b) SEM images showing the gold NP attached on the SnO_2 WG.

2.2 Compressible polymer cladding and characterization with AFM

2.2.1 Overview

The compressible polymer cladding serves as a mechanical resistor (i.e., spring) for the NP and converts the distance-dependent optical scattering signals to a force. Ideally,

this cladding layer should be thin, with a total thickness <20 nm, to be within the steepest part of the decaying evanescent field and should cause strong plasmon–dielectric coupling effects. Different polymer cladding system has been developed for the NOFT system. PEG was initially chosen for the NOFT platform, given its extensive use as an antifouling film for proteins and other biomolecules, as well as its ability to be grafted in thin, dense monolayers to oxide surfaces. PEM is another choice that can be integrated with the NOFT system due to its simple procedure to prepare with the layer-by-layer (LbL) deposition. In this section, PEM was selected as the compressible cladding and its mechanical properties were evaluated experimentally by utilizing tools like AFM to create nanoindentations on the as-prepared films to extract its mechanical properties.

2.2.2 Tunable Polyelectrolyte multilayer

Polyelectrolyte multilayer (PEM) is formed based on electrostatic interactions between sequentially deposited polyelectrolyte with alternating charge. One of the great benefits of using PEM films is that the architecture can be modified with nanometer precision to meet different requirements such as thickness, controlled permeability and biocompatibility [65]. The high versatility in the polyelectrolyte selection such as synthetic or natural, and deposition parameters such as PH, salt concentration, polyelectrolyte concentration, collectively facilitate the construction of the highly tunable PEM layers. Additionally, PEM is applicable on different platforms like colloidal particles, or dielectric substrate. A large library of PEM structures has been developed as a promising biomaterial coating in biosensors, drug delivery and controlled drug release [66, 67].

Mechanical properties of PEM films can be modulated in several ways as shown in **Figure 2.4**. For native films, ion exchange mechanism dominates the PEM formation, during which the polyelectrolyte-counterion (extrinsic charge compensation) pairs are replaced by polyelectrolyte-polyelectrolyte pairs (intrinsic charge compensation) [68]. Thus, pH and ionic

strength of polyelectrolyte solutions could significantly alter the final structure. In general, if the polyelectrolyte was deposited in a charged state or if the ionic groups are not compensated due to the absence of enough salt ions, the film would be thinner and more rigid. While if the polyelectrolyte was deposited in neutrality or higher ionic strength, the film would be thicker with an interpenetrated structure. This offers one way to modulate the mechanical property of the PEM film. However, native PEM governed by ionic crosslinking has a dynamic structure which is sensitive to local solution environment and can also easily break and re-form during the swelling process. Another strategy to tune the mechanical property and enhance the stability of the PEM film is to form chemical or physical cross-links between the polymer chains [67]. The carbodiimide chemistry has been widely applied as a chemical crosslinking method for stabilizing PEM. The amine and carboxylic groups can be linked covalently through 1-ethyl-3-(3-dimethylamino- propyl) carbodiimide (EDC). NHS is usually included as well to prevent the rapid hydrolysis of the intermediate byproduct. The chemically crosslinked PLL/HA film was measured with AFM and appears to be 6 - 8 fold stiffer than the native film [69].

In this chapter, we choose hyaluronan (HA) as polyanion and poly(allylamine hydrochloride) (PAH) as polycation to construct the (HA/PAH) film as our PEM system. HA is a natural biopolymer found in human body and is highly hydrated surrounded by 20 - 30 water molecules per disaccharide unit [70].

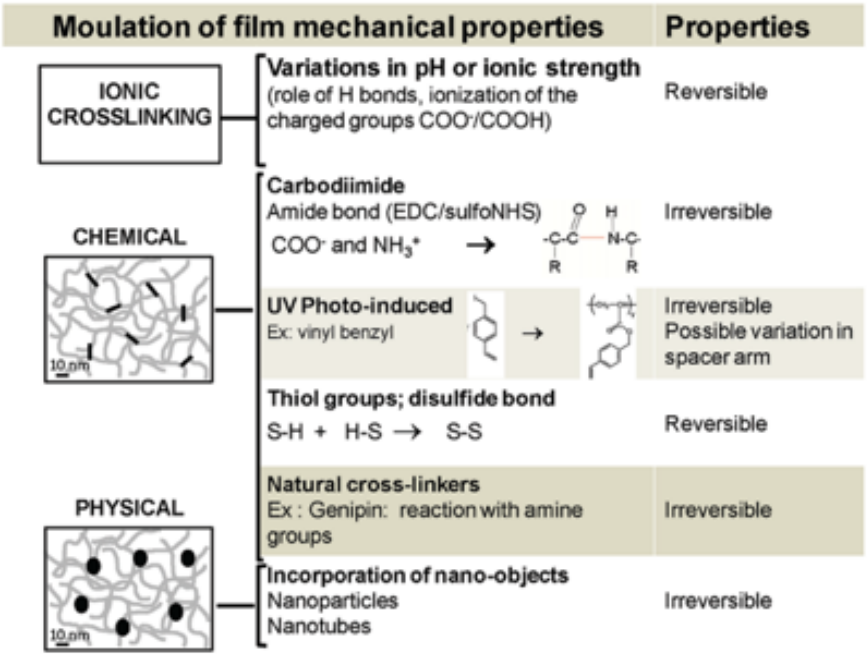

Figure 2.4. Overview of strategies to modulate mechanical properties of PEM films [67].

2.2.3 PEM layer preparation and AFM nanoindentation

PEM layer was first prepared on silicon substrate for AFM characterization. Silicon substrate was diced into 2cm x 2cm pieces and cleaned with RCA and Piranha solution sequentially at first. The substrate was then placed in the oxygen plasma cleaner using a base pressure of 200 mTorr and cleaned for 10 mins. The substrate was then rinsed with DI immediately after the plasma treatment to render the chip hydrophilic and hydroxylates the surface. Prepare the silanization solution in a glove box with the humidity controlled, by adding 4 mL of anhydrous toluene and 0.8 mL (3-Aminopropyl)trimethoxysilane (APTMS) to a small glass vial. Vapor-phase silanization step was carried out on a hot plate set at 100 °C for 1 hour. PAH and HA solution with a concentration of 1 mg/mL was prepared in 150 mM NaCl and 20 mM HEPES buffer. The mixture was stirred at 400 rpm overnight for better dispersion. The solution was then filtered through the nylon filter and a droplet of the HA solution was put on the substrate and sit for 1 min. The substrate was then rinsed in fresh salt bath (150 mM

NaCl) for 3 times. Then a droplet of PAH solution was put on the substrate and let sit for 1 min, followed by the same rinsing procedure. These steps were repeated for 2 times to construct the 2.5 multilayer with the final structure of (HA/PAH/HA/PAH/HA). Prepare the cross-linking solution containing 50 mg/mL EDC and 11 mg/mL NHS in the 150mM NaCl salt solution, immerse the substrate in the cross-linking solution at 4 °C and incubate overnight.

AFM nanoindentation experiment was carried out using a multimode AFM (Veeco Nanoscope IV). Triangular SiN MLCT probe (Bruker) with a tip radius of r = 30 nm was used to acquire the force curve. The AFM cantilever was cleaned in the piranha solution before each measurement to clean the contaminations and to render the tip hydrophilic. The force-indentation curve was acquired in 1xPBS solution in a fluidic cell to mimic the condition of polymer cladding in a biological environment. Force sensitivity was first calibrated by indenting the tip on a hard silicon substrate in 1xPBS. The acquired force curve was then analyzed using the Nanoscope software.

2.2.4 Determination of elastic modulus of PEM

Force indentation curve of native PEM film and the chemically crossed-linked film were acquired as shown in **Figure 2.5**. The PEM film with chemical cross-links shows a significant different force response compared to the native PEM film. This indicates the mechanical property could be successfully modulated using the chemical cross-link approach. To carry out detailed studies on the elastic properties of the films, simple mechanical models such as the Hertz model cannot be used. In the Hertz model, the indentation is assumed to be negligible compared to the film thickness. However, this is not the case with the compressible polymer thin film, which causes the model to fail because of the substrate interference effects. Instead, we can use the Dimitriadis model, which includes substrate effects and produces Young's moduli for the PEG films after fitting the force indentation curves [71].

$$F = \frac{4E}{3(1-\nu^2)} R^{1/2} \delta^{3/2} \left[1 - \frac{2\alpha_0}{\pi}\chi + \frac{4\alpha_0^2}{\pi^2}\chi^2 - \frac{8}{\pi^3}\left(\alpha_0^3 + \frac{4\pi^2}{15}\beta_0\right)\chi^3 + \frac{16\alpha_0}{\pi^4}\left(\alpha_0^3 + \frac{3\pi^2}{5}\beta_0\right)\chi^4 \right] \tag{2.8}$$

where $\chi = \sqrt{R\delta}/h$, δ is the indentation depth, R is tip radius, h is film thickness, α_0 and β_0 are functions of thin film's Poisson's ratio ν. When the thin film is bonded on the substrate, they can be expressed as:

$$\alpha_0 = -\frac{1.2876 - 1.4678\nu + 1.3442\nu^2}{1-\nu}$$
$$\beta_0 = \frac{0.6387 - 1.0277\nu + 1.5164\nu^2}{1-\nu} \tag{2.9}$$

Assuming $\nu = 0.5$, the Equation 2.8 can be written as:

$$F = \frac{4E}{3(1-\nu^2)} R^{1/2} \delta^{3/2} \left[1 + 1.133\chi + 1.283\chi^2 + 0.769\chi^3 + 0.0975\chi^4 \right] \tag{2.10}$$

For each point of the force curve, the Young's Modulus (E) was determined by fitting the curve with the Dimitriadis model (**Figure 2.6**). $(HA/PAH)_{2.5}$ film with 25 mg/mL crosslinker concentration yields an average of 189.93 kPa Youngs' modulus, while the PEM film with 50 mg/mL crosslinker concentration renders a 413.96 kPa Young's modulus. These values are also quite similar to the chemical property of cross-linked $(PLL/HA)_n$ film [72]. To further test the model fidelity, the force curve was also fitted with the Hertz model to compare the fitting results. As shown in **Figure 2.7**, Hertz model failed to converge at higher indentation depth value due to the breakdown of the model.

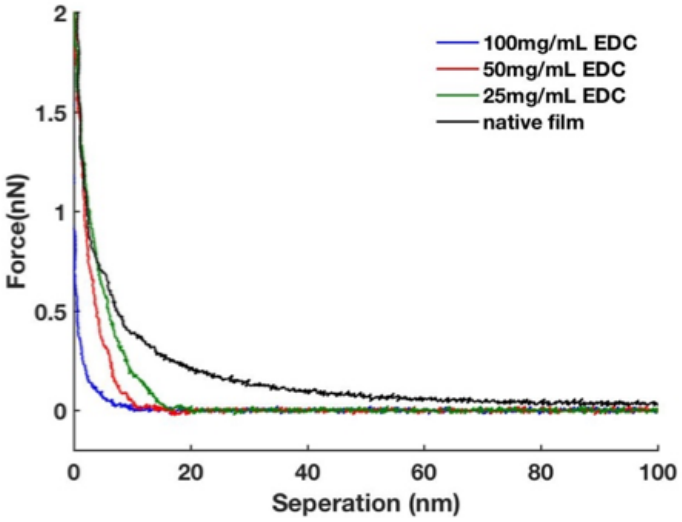

Figure 2.5. Force separation curve acquired from AFM nanoindentation for $(HA/PAH)_{2.5}$ film without chemical crosslink and with different concentration of EDC crosslinker.

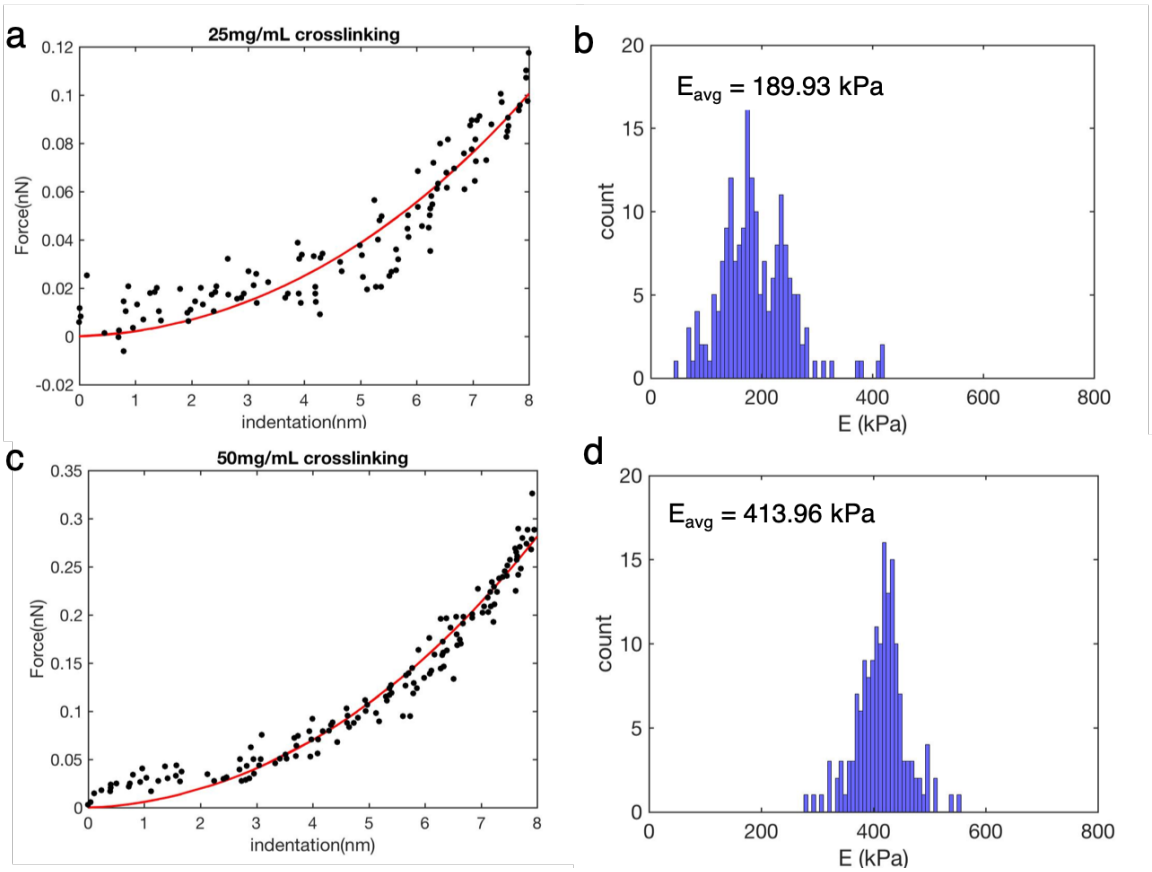

Figure 2.6. (a,b) Force indentation curve on PEM with 25 mg/mL crosslinkers fitted with Dimitriadis model and histogram of the fitted Young's modulus result for each point after indentation renders an average Young's modulus of 189.9 kPa. (c,d) Force indentation curve on PEM with 50 mg/mL crosslinkers fitted with Dimitriadis model and histogram of the fitted Young's modulus for each point after indentation renders an average Young's modulus of 413.96 kPa.

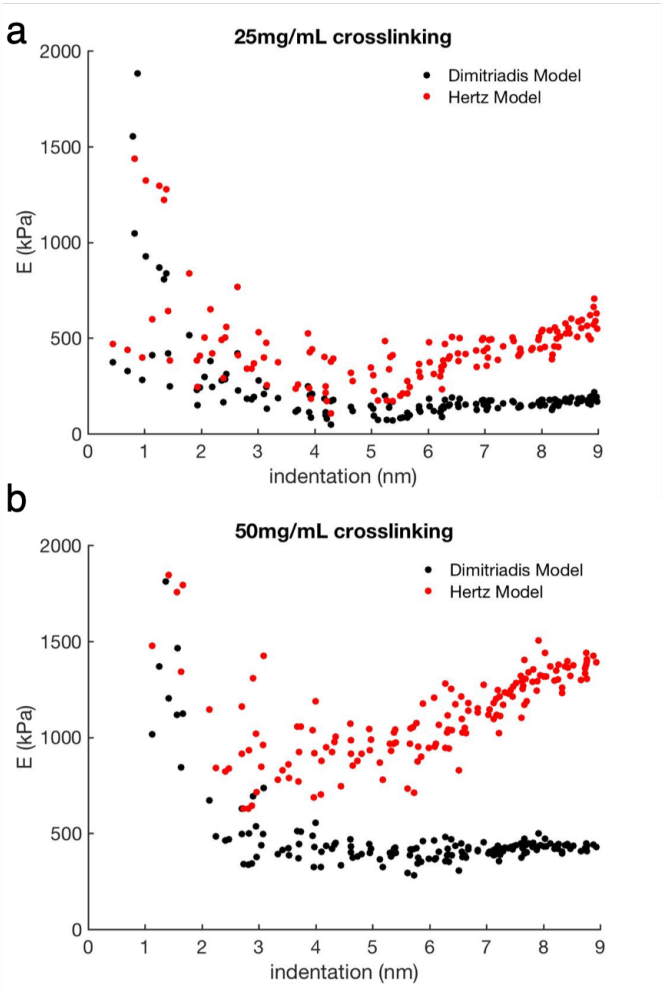

Figure 2.7. (a) Model comparison for the extracted Young's modulus for $(HA/PAH)_{2.5}$ film with 25 mg/mL crosslinkers. (b) Model comparison for the extracted Young's modulus for $(HA/PAH)_{2.5}$ film with 50 mg/mL crosslinkers.

2.3 Acoustic wave sensing

2.3.1 Overview

Acoustic wave is a mechanical wave that carries important information for communication in our daily lives. The frequency range could span from infrasound (<20 Hz) to ultrasound (>20 kHz) and acoustic waves in different frequency bands have been applied in several imaging and diagnostic technologies such as sonar, ultrasound medical imaging and building

structure monitoring [73]. Generally speaking, sound is the energy transfer through particles vibration in the medium that would create local regions of compressions and rarefactions. The sound wave comprises repeating patterns of high-pressure and low-pressure regions through a medium and an acoustic sensor is designed to detect the fluctuations in pressure as the sound impinge upon the device. The most common acoustic sensing technology is centered around the piezo ceramic (PZT) hydrophones that could convert acoustic wave into an output voltage, while it has limited applications in harsh environments due to corrosion in water.

Among all sensing platforms for pressure wave detection, fiber optic acoustic sensor has drawn great interests due to its advantages of anti-electromagnetic interference, remote sensing capability, and convenient installation with a compact structure [73]. Currently, most optical acoustic sensors are based on fiber-optic interferometry that can be further classified into two categories: the quasi-distributed fiber sensor such as fiber Bragg grating (FBG), Fabry-Perot interferometer (FPI) and the distributed optical fiber, where each point on the fiber is a sensor that could achieve continuous sensing over long distance. The distributed optical fiber system includes the Mach-Zehner Interference (MZI), Michelson Interference (MI) and Sagnac Interference (SI) [73]. Recent years, diaphragm based FPI sensor has been very popular due to its compactness and ultra-high sensitivity, in which an air pocket is formed between the fiber optic tip and the diaphragm. The sensitivity is dependent upon the diaphragm thickness and Young's modulus and numerous materials have been developed as the diaphragm such as thin layer silver [74], UV adhesive [75], and graphene [76]. However, it usually involves complex micro-fabrication procedures and the air pocket is prone to rupture under critical point.

Optical trap has also been used for acoustic sensing. Alexander et al. has proposed that an optically trapped gold nanoparticle can be used to optically readout acoustic waves generated in the liquid with the sound power level down to -60 dB [52]. When the sound was turned on, the pressure wave would exert additional driving force on the trapped particle that cause an elongation of the nanoparticle's position distribution. Due to the longitudinal nature

of the acoustic wave propagation in liquid, the motion of the nanoparticle in the direction orthogonal to the connecting line between particle and the sound source is not affected by the sound. So, the sensor could also be used for determination of the sound source.

On the other hand, sound is a ubiquitous signature in the biological system that leads to metabolic pathways regulation and specific gene expression patterns. Emission and receipt of sound have been involved in intercellular and inter-organismal signaling [77]. Certain bacterial cells treat sound signal as a growth-regulation. For example, *B subtilis* were found to emit sound waves of frequencies between 8 - 43 kHz and *B.carboniphilus* were found to form colonies when subjected to acoustic waves between 6 - 38 kHz [78]. When outer hair cells of guinea pigs were subject to ultrasonic waves, overstimulation leads to an increased concentration of calcium influx [79]. Thus, developing miniaturized acoustic wave sensor that could probe into the biological system would offer new pathway to monitor nanomechanical events to understand certain cellular behaviours.

2.3.2 Materials and Experimental part

Z-cut quartz substrate was first cleaned with RCA and piranha solution. The SnO_2 nanofibers were then selected and transferred to the cleaned quartz substrate. Choosing the appropriate nanofiber is critical. Using the UV laser, excite the end of a potential nanofiber and observe the emission exiting the other end facet. Blue wavelengths, as compared with green or white emission, indicate a smaller cross-sectional dimension. Select fibers that have strong blue or green emission; these typically have cross-sectional dimensions between 200 and 400 nm. This will allow more of the guided modes to interact with the plasmonic NPs and generate a higher SNR. The nanofibers can have various lengths. Choose nanofibers with lengths of at least 300 μm to separate the excitation and collection regions in the field of view and reduce the amount of signal collected from the excitation spot while the objective is positioned over the NP or opposing end facet. The PEM film was then deposited on the substrate with the

nanofiber as described in the previous section. Sensing gold NP was prepared by diluting the citrate gold solution (Sigma Aldrich) 100 times. 0.04-inch-thick PDMS sheet was cut into a 15 x 15 mm size with a 5 x 5 mm square hole in the middle which serves as the reservoir that hold the NP solution during the attachment procedure. 50 μL of the prepared gold NP solution was added to the PDMS chamber and the nanofiber was excited with the UV laser to monitor the attachment process. Once the desired amount of gold particles is observed (3 ~ 4), immediately pipette out the gold NP solution and replace it with DI water, repeating multiple times to stop the attachment process (**Figure 2.8**). Take image of the excited nanofiber using the EMCCD camera (Andor) and label the positions of defects and gold NP attached for reference.

The PZT disk with a resonant frequency of 2.3 MHz was selected as the acoustic source. Two pogo pin was attached on the surface for connection. The PZT disk was first connected to a mini-circuits amplifier, then connected to the function generation (SG382, Stanford Research Systems). The power response of the PZT disk with amplifier was first calibrated using LDV and oscilloscope. Setup to integrate the NOFT substrate for acoustic sensing was shown in **Figure 2.9**. The prepared NOFT substrate with gold NPs was placed inversely on a silicon rubber that act as a damping material to remove vibration from the acoustic source. Due to the detection limit of the EMCCD camera, the function generator was set at the resonant frequency of 2.3 MHz, with an amplitude modulation with the frequency in the range of (100Hz ~ 200 Hz). The optical intensity change of the end facet of the nanofiber was recorded with the EMCCD camera and the time-course intensity could be extracted for analysis.

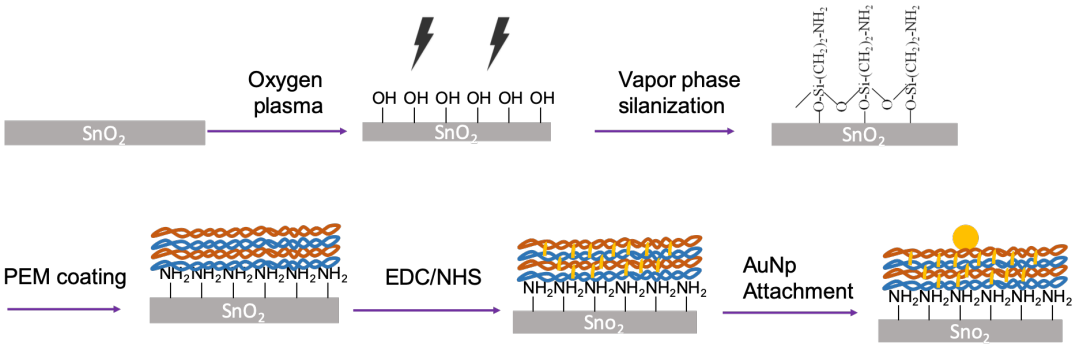

Figure 2.8. Schematic of PEM film deposition and gold NP attachment process to prepare the NOFT substrate

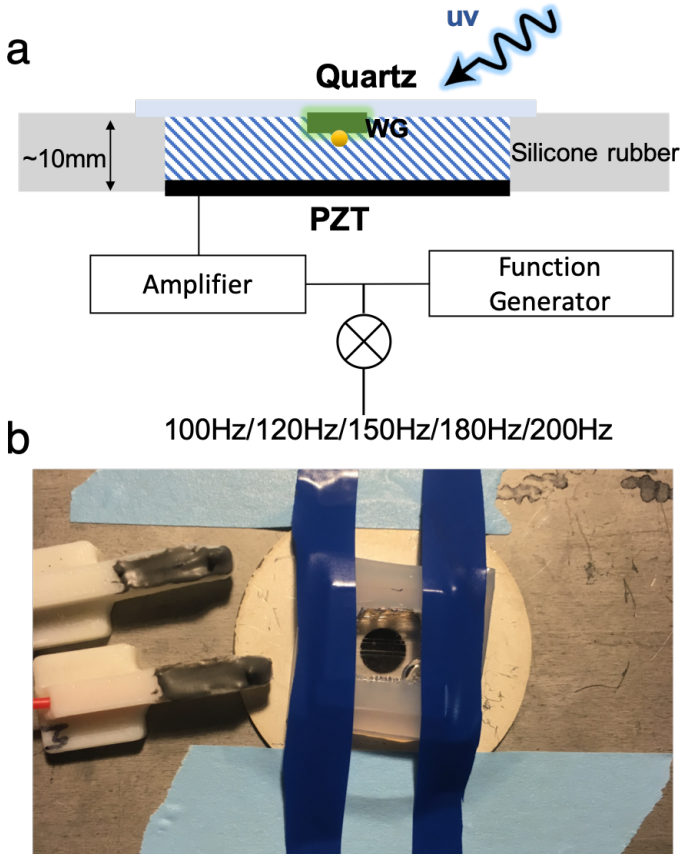

Figure 2.9. (a) Schematic setup for the acoustic wave sensing. (b) Photo of an actual setup.

2.3.3 Results and discussion

Figure 2.10a shows the optical scattering image acquired from the EMCCD camera before and after the sensing gold NP attachment at the final stage. Boxes are drawn to define the region of interest (ROI) to extract the intensity data for analysis. The red box shows the appearance of additional scattering event on the fiber after gold NP attachment process. Technically, each gold NP can act as an individual sensor that is sensitive to the acoustic wave and assuming all particles vibrate in phase, the collective movement can also be tracked through monitoring the intensity change of the fiber output (white box). **Figure 2.10b** shows the time series of optical scattering from the end facet of the nanowire and **Figure 2.10c** shows the Fast Fourier Transforms (FFT) results of the intensity data to extract the frequency dependent information. It is clear that a pronounced peak exists in the FFT spectrum at the driving frequency of the PZT disk. Analyzing all 47 measurements from 2 different nanofibers driven at different frequency, we could find out the FFT peak intensity is strongly correlated with the average gold NP scattering intensity (**Figure 2.10d**). This is expected as the ROI that has higher signal-to-noise ratio would show higher amplitude. The output signal intensity is related to the number of gold NP attached, laser intensity and nanofiber waveguiding property. **Figure 2.10e** shows the FFT peak response at different frequency without significant partiality (one-way ANOVA) indicating a uniform response within the modulating range.

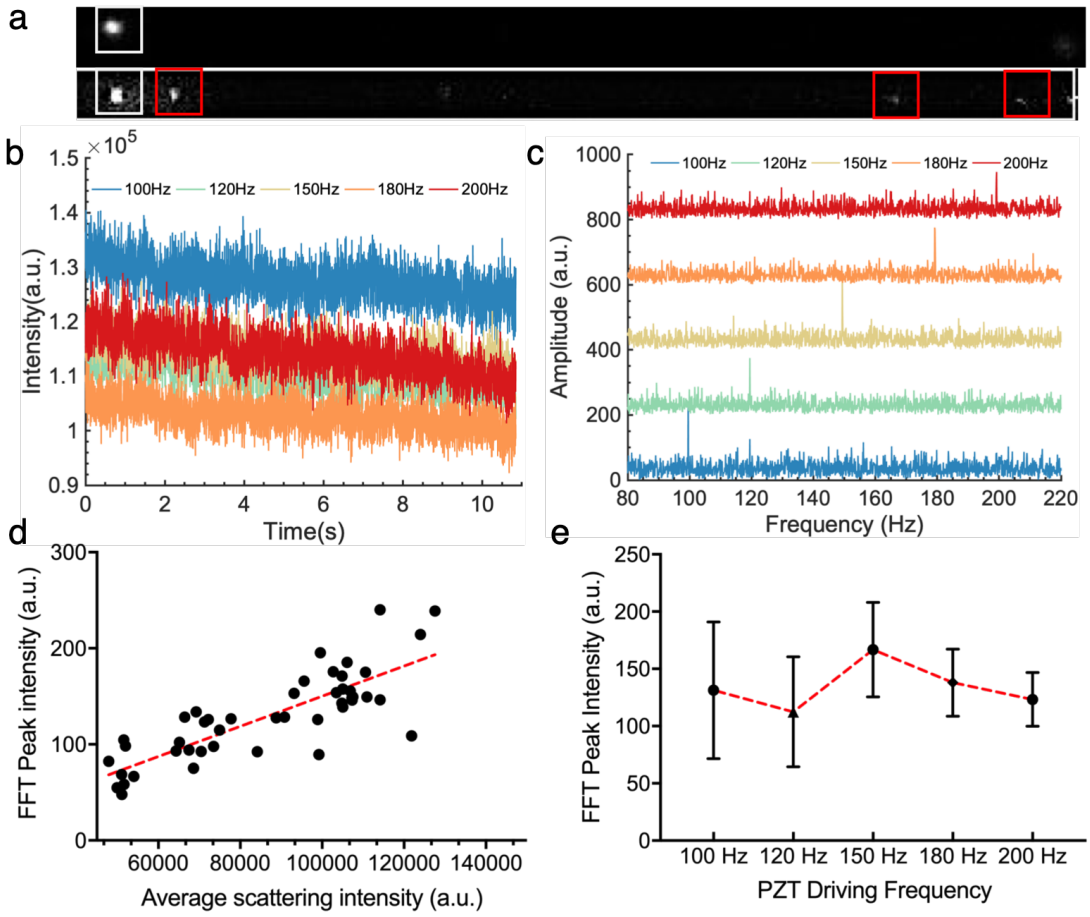

Figure 2.10. (a) Optical scattering of SnO_2 nanofiber while being excited by the 325 nm laser before and after sensing gold NP attachment. The white box is an ROI of the nanofiber output where the signal is extracted and process. The red box indicates the scattering from sensing gold NP. (b) Time series of the optical scattering intensity from the end facet of the nanofiber while the PZT is driven at various frequency. (c) FFT of the nanofiber output scattering data showing the pronounced peak at the PZT driving frequency. (d) FFT peak intensity as a function of average optical scattering intensity, dotted line is the linear fit. (e) FFT peak intensity versus PZT driving frequency shows uniform response and no significant difference (one-way ANOVA).

Control experiments were also carried out to validate the sensing mechanism, that the nanoparticle embedded in a compressible cladding is responsible for the transduction mechanism. Two schemes were performed. In the first scenario, the sensing gold NP was linked onto the nanofiber directly without the compressible cladding. In the second scheme,

no sensing gold NPs were attached on the compressible cladding. No observable peak was detected under both schemes further verify that the modulation is indeed coming from the thickness change of a compressible cladding under periodic compression from the sound wave (**Figure 2.11**).

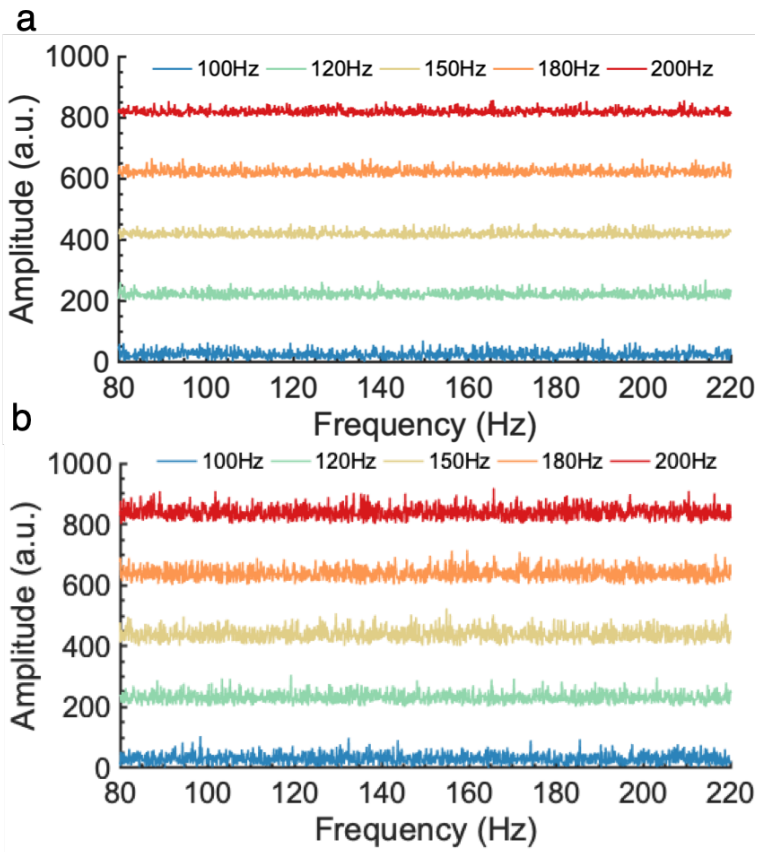

Figure 2.11. (a) FFT of the nanofiber output scattering data without the compressible cladding (b) FFT of the nanofiber output scattering data without sensing gold NP attached on the fiber.

In order to quantify the energy transmitted from the vibrating PZT disk to the gold NP, the power output of the PZT disk was first calibrated using an oscilloscope with both voltage and current probe. The surface displacement and particle velocity of the PZT disk while being modulated at the resonant frequency were monitored simultaneously using the laser doppler vibrometer (LDV). The combined results were summarized in **Table 2.1**. In a homogeneous,

isotropic fluids in which the speed of sound is a constant, the acoustic pressure of a plane wave could be described as the following [80]:

$$p = \rho_0 cU = 0.25\ MPa \tag{2.11}$$

where $\rho_0 = 10^3\ kg/m^3$, is the fluid density, $U = 0.17\ m/s$ is the particle velocity of the acoustic wave at the surface of the PZT disk measured with LDV, $c = 1500\ m/s$ is the sound velocity. The acoustic intensity could be then be extracted :

$$I = p^2/(2\rho c) = 20833\ W/m^2 \tag{2.12}$$

this leads to the power acting on the gold NP as $W = AI = 163\ pW$, where $A = 7.84^{-15}\ m^2$ is the gold NP area.

Table 2.1. PZT disk power calibration

Applied voltage (V)	Frequency (Hz)	Measured Voltage (V)	Measured Current (A)	Displacement (nm)	Velocity (mm/s)	Power (W)
0.1	2.3*10^6	1.65	0.27	1.55	22.38	0.4455
0.2	2.3*10^6	3.14	0.51	3.7	54.33	1.6014
0.3	2.3*10^6	4.7	0.77	5.29	75	3.619
0.4	2.3*10^6	6.15	1.01	7.28	105.16	6.2115
0.5	2.3*10^6	7.8	1.39	8.8	125.79	10.842
0.6	2.3*10^6	8.6	1.73	10.023	145.45	14.878
0.7	2.3*10^6	9.2	2.09	11.02	158	19.228
0.8	2.3*10^6	9.6	2.37	11.39	162.66	22.752
0.9	2.3*10^6	10.1	2.61	11.84	170.29	26.361

2.4 Conclusion

2.4.1 Limitations and future work

While we have demonstrated using NOFT platform for acoustic wave sensing, there are still certain restrictions that limit the overall application of NOFT. For example, the SnO_2 nanofibers must be visually screened one by one from a large mass of synthesized nanofibers. This serial approach to fabricating the devices can limit the reproducibility of the transducer as well as the large-scale fabrication of it. The hysteresis response of polymers can also restrict the use of NOFT to lower frequencies, so it's of interest to characterize the polymer response modulated at higher frequency. Right now, we are using AFM force indentation to probe the mechanical property of the polymer cladding, while the force response was acquired in a relatively low frequency regime (0.1 Hz ~ 10 Hz). It would be of interest to use NOFT as a contact-free tool to investigate the dynamic mechanical property of polymer thin film modulated at much higher frequency (>kHz) with a high-speed camera.

In addition to the synthetic and fabrication limitations, coupling light into and detecting light out of the NOFT devices can impose restrictions on how these sensors are integrated with other optical systems. In current configuration, a free-space coupling method is used that uses a focused 325-nm laser to excite white defect emission in the SnO_2. In certain applications, free-space coupling may not be possible, so other coupling strategies would have to be developed. For example, a direct fiber optic-to-nanofiber coupling could be designed that would allow the user to eliminate the UV light source and inject a wavelength of choice directly into the NOFT. Coupling from a bulk fiber to the nanofiber can be achieved either by a butt-coupled (i.e., a nanofiber bonded to the core of a cleaved silica fiber) or a side-by-side (e.g., tapered silica fiber evanescently coupled to the nanofiber) geometry. Because the nanofibers act as passive dielectric waveguides up to the band edge of SnO_2, any wavelength in this range can be used; however, to achieve the highest spatial sensitivity from the plasmon–dielectric coupling

effects, the wavelength should be resonant with the metal NP. **Figure 2.12a** shows the spectra of a single AuNP attached on the SnO_2 nanofiber with a peak intensity at λ~540 nm which is close to the plasmon resonance of the 80 nm gold NP. The spectra of the SnO_2 nanofiber output was also acquired before and after the gold NP attachment. As shown in **Figure 2.12b**, spectra of the guided mode under UV excitation shows two peaks at ~ 500 nm and ~ 560 nm before attachment, while there's a significant decrease in the higher wavelength peak and a blueshift in the first peak after gold NP attachment. This further confirms that scattering from the gold NP majorly comes from the interaction with the guided mode at its resonance frequency. Thus, in order to enhance the gold NP scattering intensity, and increase our signal-to-noise ratio, we could use SnO_2 as a passive waveguide to guide through 543 nm laser, which is close to the gold NP resonance wavelength. **Figure 2.12c** shows a proposed free-standing structure through butt-coupling between SnO_2 nanofiber and a cleaved silica fiber. The assembly could then be fixed on a T-junction trench for gold NP attachment and the scattering could also be monitored in the far-field via the EMCCD camera. **Figure 2.12e** shows the gold NP attachment process and the scattering events from gold NP were compared using UV light source excitation verse passively waveguiding 543 nm green laser. The scattering power could be extracted through quantifying the scattering intensity using the equation:

$$eV = (cts/g) * (S/QE) * 3.65 \tag{2.13}$$

where cts is the counts extracted from the EMCCD camera, g is the gain, S is the EMCCD sensitivity (12.6), QE is the quantum efficiency (92.5%), 3.65 is the physical constant for electron creation in silicon sensor. After conversion, we could backout the power from a single AuNP is of 1.1 pW for butt-coupling using a 543 nm light source, and 0.3 pW while excited using the UV laser. This indicates a three times enhancement in the scattering power using the direct coupling method.

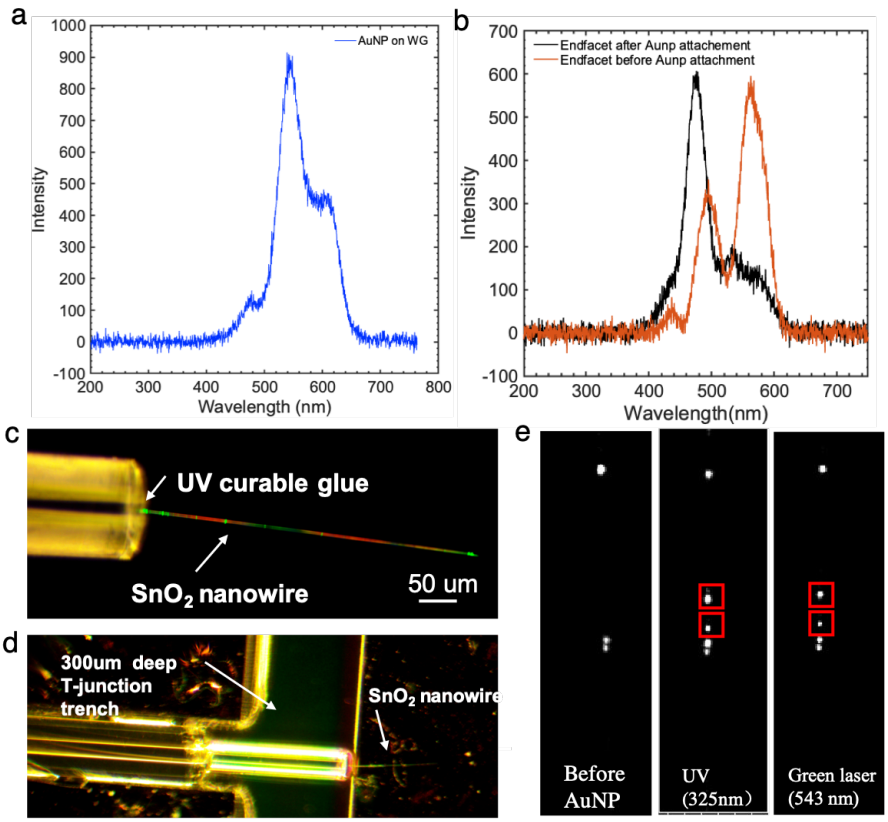

Figure 2.12. Free-standing SnO_2 nanofiber configuration (a) Spectra captured from a single AuNP excited with the evanescent field of the SnO_2 nanofiber. (b) Spectra captured from the SnO_2 nanofiber output before and after the AuNP attachment. (c) Optical image of the free-standing SnO_2 nanofiber butt-coupled with a silica fiber. (d) Optical image of the free-standing structure fixed in a trench for AuNP attachment. (e) Optical scattering of SnO_2 nanofiber before and after AuNP attachment being excited by 325 nm laser or as a passive waveguide guiding 534 nm green light. Red boxes indicate the attached AuNP.

2.4.2 Summary

In this chapter, we introduced a nanofiber optic force transducer for acoustic wave sensing. The compressible polymer coating and the distance dependent near-field scattering of a plasmonic particle together provide the force feedback, which could be monitored through far-field optical tracking. The compressible polyelectrolyte multilayer was controllably grafted on the SnO_2 nanofiber and was characterized through AFM nanoindentation to extract its mechanical property. The force sensing capability was then demonstrated for acoustic wave

sensing using a PZT disk source. The power actuating on a single particle was calculated to be 163 pW. The versatile platform could also be transformed to a free-standing structure through butt coupling with a silica fiber and passive-waveguiding the light at the resonance frequency of the gold NP.

2.5 Acknowledgement

Chapter 2, in part, is a reprint of the material ”Nanoscale fiber-optic force sensors for mechanical probing at the molecular and cellular level” as it appears in Nature Protocol, Yuesong Shi, Beril Polat, Qian Huang, and Donald J. Sirbuly, 2018, 13, 2714 - 2739. The dissertation author was the primary investigator and author of this material.

Chapter 3

Multifunctional microfiber based electrochemical, optical and spectroelectrochemical sensor

Developing microdevices with the capability to carry out multifunctional measurement is of great interest for understanding disease and accelerating drug discovery. Microscale endoscope based on fiber optics allow minimally invasive probing of activities inside the biological environment. In this chapter, we introduced a compact multimodal micro probe with small footprint (~ 10 μm), low electrical impedance (~ 10 $k\Omega$ at 1 kHz), and high optical spatial resolution for both electrical and optical measurements. We were able to demonstrate the selective electrochemical detection of dopamine and serotonin, with a limit of detection of 800 nM and 1.2 μM respectively. The multimodality of the microprobe was demonstrated through spatially localized spectroelectrochemical probing of the electrochromic behavior of PEDOT and Methylene blue (MB). The multifunctional microprobe with simultaneous electrochemical and optical sensing capability shows great promise for *in vivo* access to electrical and optical monitoring or stimulation at the single-cell level.

3.1 Introduction

3.1.1 Motivation for multifunctional microdevices

There has been an increasing effort in developing micro sensing devices to shift from bulky analytical approaches as chromatography and mass spectrometry. Recent years, devel-

opment of miniaturized sensors has largely expanded research in preventive medicine and point-of-care devices due to its noninvasive nature [81]. Reducing the sensor dimension to microscale has also offered unique functionalities such as high spatial resolution [82], non-invasive implantation [83], and decreased power consumption [84]. While currently, most micro sensing platforms are single-mode device that transduce only one type of signal, either electrical, optical, or mechanical. This approach imposes some major limitations such as the sensitivity-dynamic range trade off and limited specificity provided from a single pathway [85]. On the other hand, integration of disparate sensing modes offers several benefits through bridging the performance gap from each mode. First, the multi-modal measurements provide the cross-validation of fidelity between two signal pathways that increase the signal reliability and accuracy. Second, the synergic operation of dual modes expands the functionalities of the sensor that enables possibilities to probe unique materials properties like electrochromic behavior. Moreover, the limitations come from one modality such as low signal noise ratio or suppressed resolution could be compensated by using another pathway [86]. These merits could expand the overall operation dynamic range of the sensing platform.

However, there has been challenges for downsizing a multimodal device due to the difficulty in complex microfabrication for multifunctional device integration, read-out signal interrogation, and suppressing interference and excess noise at the micro scale. Our lab has developed an ultracompact electro-optic microprobe for optogenetic study with both electrical and optical modality. In this chapter, we further expand the functionality of the system and demonstrate its electrochemical sensing capability for neurotransmitters detection as well as the localized fluorescence spectroscopy recording. The combined modality was demonstrated through a spectroelectrochemical platform for probing the electrochromic behavior.

3.1.2 Neurotransmitter electrochemical sensing

Neurotransmitters (NT) are neuroactive substances that are secreted by neurons and relay messages to target cells. Chemical signaling through the release of NT into the extracellular space is the primary path for communication between neurons and this chemical synaptic transmission has proven to be important for understanding brain functions and treatment of a broad type of disorders [87, 88, 89, 90, 91]. For example, dopamine is one of the NTs with great clinical importance for motor function and motivational behaviors. The decreased level of dopamine will cause uncontrolled motor function and Parkinsonian symptoms [92].

Being able to directly access chemical communication between neurons and achieve real-time NT sensing is a long-standing aim. The desired NT sensor should have the following characteristics: (1) High sensitivity: The concentration of these NT in the brain is usually very low and produced sparsely in specific region (**Table 3.1**). (2) High Selectivity: The main electroactive interference in the extracellular fluid of the is ascorbic acid, which is usually 100 ˜ 1000 times more concentrated than dopamine in the brain [93]. There are also other electroactive molecules including DOPAC and UA that can be oxidized at a similar potential as dopamine. Being able to distinguish the NT of interests from other interference molecules is crucial for acquiring reliable measurements. (3) High temporal resolution is required to capture the transient extracellular concentration change: dopaminergic neurons fire action potentials in two patterns, tonic and phasic. The tonic firing happens at 2˜5 Hz resulting a steady-state basal level of extracellular dopamine. The phasic firing happens at 15˜ 100 Hz that leads to transient fluctuation in dopamine concentration [94]. After the exocytosis occurs, dopamine rapidly diffuses out of the synaptic, captured by receptors and degraded on the femtosecond scale [95]. Thus, a high temporal resolution, ideally around sub-second, is desired for real-time measurements. (4) Long-term *in vivo* monitoring without compromised performance: It is highly desirable to design a miniaturized sensor with either wireless operation or detachable connecting wire for long-term measurements in behaving animals as this would

help to correlate NT concentration fluctuations with specific behaviors. (5) Multi-analyte detection: The complex interplay between different NTs has also been responsible for various neural disease. For example, the motor function in striatum is related to the equilibrium between dopamine and acetylcholine and a disruption of the balance would lead to Parkinson's disease [96]. Therefore, the simultaneous detection of multi analytes *in vivo* is highly desired to better understand the progression of common mental disorders.

Compared to traditional methods for NT detection such as liquid chromatography and microdialysis, electrochemical sensing has the advantages of rapid, sensitive, selective and low-cost detection of biomolecules and a variety of voltammetry techniques have been utilized to directly detect electroactive neurotransmitters. Most of the traditional electrochemical sensors fabricated are bulky in size which is not ideal for implantation purpose due to the induced tissue damage. Thus, tremendous efforts have been made to develop miniaturized electrode sensors for neurotransmitter sensing. Microelectrodes ($< 25\ \mu$m in at least one dimension) impose several advantages for *in vivo* neurotransmitter sensing such as: (i) reduced immune response for chronic implantation, (ii) superior electrochemical characteristic with high steady-state current density and high mass transfer rate [97], (iii) high spatial selectivity since neurotransmitter release has shown to be heterogeneous within a single brain area [98]. However, microelectrode-based electrochemical sensing still remains challenging due to its low sensitivity and poor surface biofouling resistance. Carbon-fiber microelectrodes have been extensively used for neurotransmitter detection and served as the standard tool for detection [99]. While it requires tedious fabrication method, suffers from biofouling and is limited with a single read-out mode [100]. **Table 3.1** summarizes the electrochemical property and biological functions of some common NT and other electroactive molecules coexist in the brain.

Table 3.1. Summary of common neurotransmitters and other electroactive molecules in the brain [101, 102]

	Molecule	Redox-reaction	Localization	Concentration	Role and Pathology	Approximate oxidation potential (vs Ag/AgCl)
Neurotransmitters	Dopamine	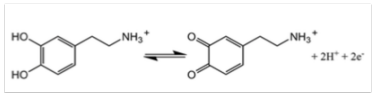	Hypothalamus, substantianigra of midbrain	26 nM, 40 nM	Parkinson's disease and schizophrenia	+0.2 V
	Serotonin	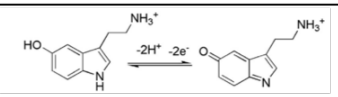	Midbrain, hypothalamus, limbic system, spinal cord	70 nM	sleep, schizopherenia, anxiety and depression	+0.35 V
	Norepinephrine	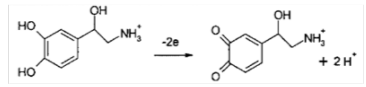	Locus coeruleus of the midbrain, brain stem, limbic system.	12 nM, 2.49 nM	Good feeling, depression	+0.2 V
	Epinephrine	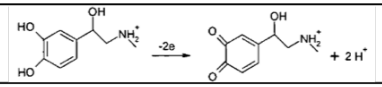	Tegmental and medulla	0.46 nM	Fight-or flight response	+0.2 V
Other electroactive molecules	Ascorbic acid	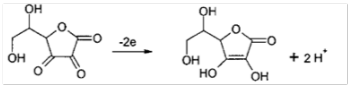	\	0.5 mM	\	+0.2 V
	DOPAC	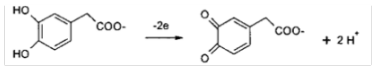	\	\	Dopamine metabolite	+0.2 V
	Uric acid		\	\	Purine metabolite	+0.3 V

3.1.3 Localized spectroscopy and spectroelectrochemistry

On the other hand, spectroscopy has also shown great promise by its ability to selectively identify biomolecules and determination of constituents of unknown species [103]. Flexible fiber-optic devices have enabled remote sensing and imaging under conditions not allowed through conventional light microscopy. Characteristics like high aspect ratio and the small size of fiber optics have allowed their applications as implantable device for long-term chronic imaging studies [104]. The small core of fiber-optic also act as a pinhole that reduce the background noise by eliminating the out-of-focused fluorescence emission [105] and allows remote high-spatial resolution imaging. The benefits of both electrochemistry sensing capability and spectroscopy can be leveraged by combining both techniques to provide unique signatures of redox active materials, known as spectroelectrochemistry. It has the advantage of acquiring the time-resolved in situ spectroscopic characteristics of materials undergoing electrochemical reactions. Using the optical response to record neuroelectrical activities has also shown great potential to interface with the nervous system [106]. Conventional spectroelectrochemical configuration usually includes bulky optical transparent electrode (OTE) such as indium tin oxide (ITO) which limits their application *in vivo* [107]. Fiber-optic based spectroscopic device offers ease for coupling light in and out for remote sensing. While currently most fiber optic based spectroelectrochemical platform are based on side-polished fiber platforms over 200 μm in dimension [42]. To date, no noninvasive spectroelectrochemical probe with remote sensing capability has been developed of sub-10 μm scale.

Our multifunctional microprobe is comprised of a microfiber optic coated with a conductive layer, passivation layer and a final conductive polymer coating using poly(3,4-ethylene dioxythiophene) polystyrene sulfonate (PEDOT:PSS). We were able to achieve a high aspect ratio assembly with small footprint (~ 10μm), low electrical impedance (~ 10 kΩ at 1 kHz), and high optical spatial resolution. We've demonstrated its electrochemical sensing capability by selective and sensitive detection of dopamine and serotonin while maintaining

its electrochemical integrity during consecutive measurements through an anodic treatment method. With a small probe size and precise control of the applied potential, localized change of optical property could be acquired simultaneously. The multi-modal capability was then demonstrated through the spectroelectrochemical probing of electrochromic materials. It is to our knowledge, the smallest scale for a fiber coupled spectroelectrochemical platform. This compact multifunctional microprobe design has many desired characteristics for *in vivo* detection of electroactive molecules and paves the path for versatile applications.

3.2 Materials and experimental parts

3.2.1 Electro-optic microprobe preparation and fabrication

Microfibers were first collected from a fiber bundle (Schott, Part No. 1573179) and micromanipulated over the edge of a silicon substrate. These microfibers were then coupled to a single mode fiber of 125 μM diameter (Thorlabs S405-XP) with maximum optical coupling achieved through active alignment with a UV-adhesive (Norland Optical Adhesive) securing the alignment. This optical assembly was then coated with a thin ($<$10 nm) adhesive layer of titanium (Denton 18, 2.5 mTorr, 5 s, 200 Watts), a 300 nm platinum as the conductive layer (Denton 18, 2.5 mTorr, 15 min, 200 Watts), and 2 μm parylene C as the encapsulation layer (2.5g Parylene, SCS Labcoater Deposition System; Specialty Coating Systems). To characterize each device and expose the optical channel, a focused ion beam (FEI Scios Dualbeam) was used to mill the tip of the microprobe using 5 nA of current at 30 kV.

3.2.2 PEDOT:PSS deposition

25 μM PSS was dissolved in deionized water and 1 μL/mL EDOT was added. The mixture was sonicated in water bath for 2 hours before deposition to allow uniform dispersion. PEDOT was electropolymerized on the microelectrode via a three-electrode system using electro-optic probe as the working electrode at 1.056V vs Ag/AgCl for 15s. The immersion

depth is monitored via a side-view stereoscope to control the depth for a localized PEDOT deposition.

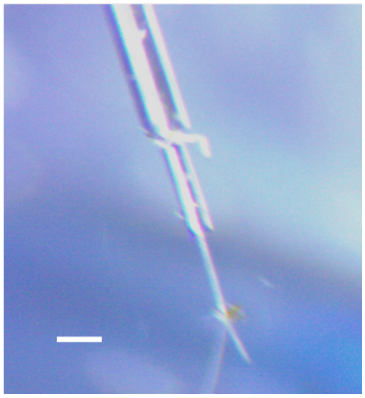

Figure 3.1. Optical image of electro-optic microprobe immersed in polymerization solution for PEDOT:PSS deposition. Scale bar is 200 μm.

3.2.3 Electrochemical and electrical performance characterization

Electrochemical performance of the microprobe was evaluated in 1x PBS solution using a versaSTAT 4 Potential/Gavanostat (Princeton Applied Research) via a three-electrode system. A platinum wire counter electrode, and Ag/AgCl reference electrode were purchased from CHI Instruments. Electrical impedance spectroscopy (EIS) was performed in potentialstatic mode at 0 V from 10 Hz to 10^6 Hz. During cyclic voltammetry (CV) test, the microprobe working electrode was swept from 0.6 V to - 0.6 V at a scan rate of 100 mV/s. The charge storage capacity (CSC) could then be derived from the time integral of a CV cycle. Equivalent circuit modeling of the EIS data was done through Zsimp software. Electrochemical detection of dopamine and serotonin was performed via square wave voltammetry (SWV) with the following parameters: 50 mV amplitude, 20 Hz frequency, and 2 mV pulse increment. A three-order polynomial baseline was fitted and subtracted from the pulse voltammetry signal for data analysis. Anodic treatment at 0.6 V for 30 s was performed in 1x PBS between SWV measurements to clean the electrode. Microprobe sensitivity was determined by the linear slope of the calibration plot. Fresh dopamine solution and serotonin solution was prepared at various

concentration in the interference solution containing 10 μM Ascorbic Acid, 10 μM Uric Acid and 10 μM DOPAC in 1xPBS. All measurements were carried out in a home-built faraday cage for electrical shielding.

3.2.4 Thin layer spectroelectrochemical cell setup

A Xenon fiber light source was introduced from the bottom through a glass slide. A 650 nm short pass filter (FES0650, Thorlabs) was positioned on top of the light source to eliminate higher wavelength interference due to the small diameter of the microfiber probe. A 1 mm thick PDMS spacer was placed on the glass slide to form the sample well and to hold the electrolyte. Microfiber probe was attached in a custom-designed probe holder (**Figure 3.2**) for electrical connection and back-end optical coupling to the Acton SP2358 spectrometer (Princeton Instruments). The probe holder was mounted on a Z translational stage and gradually lowered into the solution of 10 μm depth monitored through a side-view stereo-scope. Ag/AgCl reference electrode and Pt wire counter electrode were placed in close proximity. The spectrums were acquired continuously with 100 ms exposure time. All measurements were carried out in a home-built faraday cage for electrical shielding.

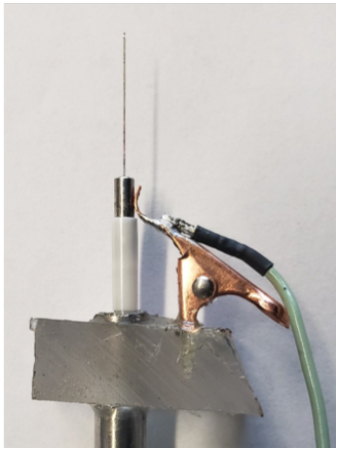

Figure 3.2. Custom probe holder for SEC experiments.

3.3 Results and Discussion

3.3.1 Electrochemical characterization of PEDOT:PSS coating on the microprobe

The electro-optic microprobe was fabricated with a coaxial structure and the fabrication process is discussed in the experimental section. The final structure of the electrode has an aspect ratio over 100 as shown in **Figure 3.3a**. **Figure 3.3b** shows the tip of the microprobe revealing the optical core, electrical layer, and the final encapsulation layer. Morphology change at the tip of the microprobe after PEDOT:PSS deposition with a rough and uniform surface structure was captured as shown in **Figure 3.3c**.

The final PEDOT:PSS coating is a crucial step that could significantly decrease the electrode impedance, increase the electrode surface area, and increase the capacitance for microelectrodes. Electrochemical performance of the microprobe was evaluated using Electrochemical impedance spectroscopy (EIS) and cyclic voltammetry (CV) using the electro-optic microprobe as the working electrode. As shown in **Figure 3.4a**, there were 4 orders of magnitude decrease of impedance at 1 kHz from 16156.11 $k\Omega \pm 7083.30$ $k\Omega$ to 11.26 $k\Omega \pm 1.09$ $k\Omega$. The significantly reduced overall impedance is associated with the increased surface area and an enhanced conductivity that significantly boosts the diffusional pseudo capacitance. Charge storage capacity (CSC) derived from the integrated area under CV spectra also indicates 50 times improvement compared to the bare electrodes. The enhancement compared to the bare electro-optic microprobe arises from the ion-exchanging property of PEDOT:PSS coating as well as the increased surface area (**Figure 3.4b**). Improvement of electrochemical sensing capability was then verified using the common redox couples of ferrocyanide/ferricyanide. **Figure 3.4c** shows the representative CV curve in a 5 mM ferrocyanide/ferricyanide solution at a scan rate of 0.1 V/s. The sigmoid shape in the voltammogram is indicative of a microelectrode response and the development of steady state diffusion [108]. The PEDOT:PSS microprobe demonstrates superior electrochemical sensitivity with more than 50-fold enhancement in the

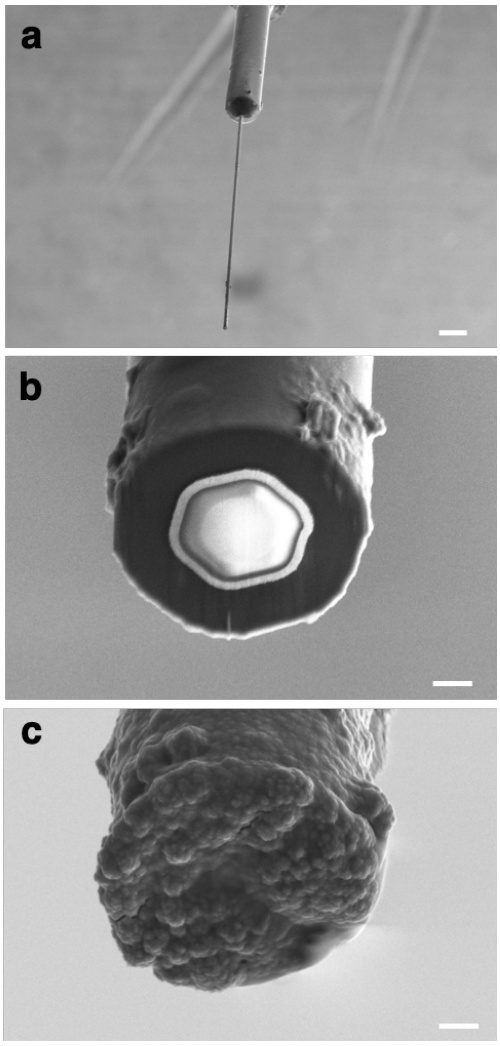

Figure 3.3. SEM image of the PEDOT:PSS coated electro-optic microprobe. (a) SEM image of the final structure of the fabricated microprobe. Scale bar is 200 μm. (b, c) SEM image of the fabricated microprobe tip before and after the PEDOT:PSS deposition shows a rough and uniform surface structure. Scale bar is 2 μm.

anodic peak current compared to the bare electrode. It is also desired to use the microprobe for neural activity modulation through the electrical stimulation process. Thus, it's important to evaluate its charge injection capacity (CIC) which indicates the maximum amount of charge that can be injected through the electrode within the water electrolysis window, typically requires a value beyond 0.5 mC/cm^2 for clinical stimulation [109]. Here, we derived the CIC value for the PEDOT:PSS coated microprobe from the voltage transient measurement with a value of 2.9

mC/cm^2 (**Figure 3.4d**).

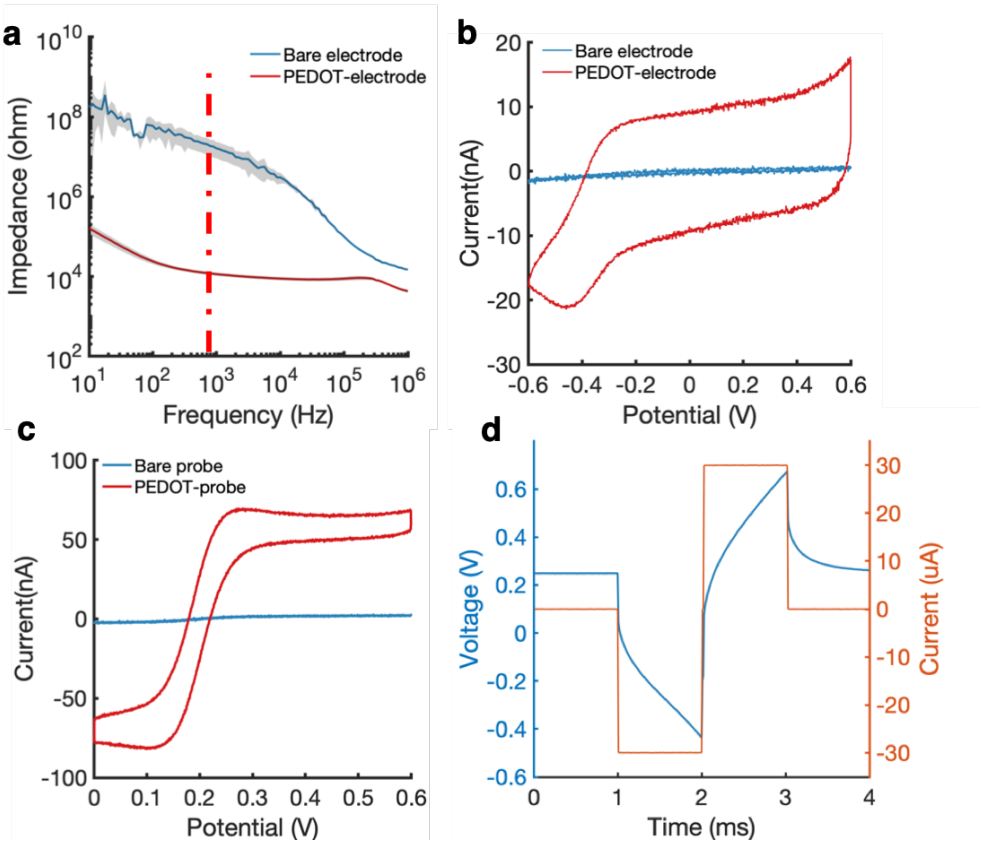

Figure 3.4. Electrochemical characterization of the PEDOT:PSS coated electro-optic microprobe. (a) EIS of the microprobe shows significant reduction in overall impedance after PEDOT deposition, red dashed line marks the 1 kHz impedance which was reduced by four orders of magnitude. (b) CV in 1xPBS solution at a scan rate of 0.1 V/s shows PEDOT:PSS coating significantly increase the capacitance. (c) CV in 0.5 mM FeCN solution at a scan rate of 0.1 V/s shows enhanced anodic peak current after PEDOT:PSS deposition. (d) Voltage transient in response to injected current with PEDOT:PSS coating shows a maximum injected current of 30 μA within the water electrolysis window.

3.3.2 Electrochemical detection of dopamine and serotonin

Neurotransmitter (NT) detection capability of the fabricated electro-optic microprobe was demonstrated for multiplex detection of dopamine and serotonin. Highly selective and sensitive neurotransmitter sensor is desired due to other interfering electroactive endogenous substances such as UA (uric acid), ascorbic acid (AA) and 3,4-Dihydroxyphenylacetic acid

(DOPAC). These molecules coexisted with dopamine and serotonin at a much higher concentration and are typically oxidized at similar potentials which leads to poor selectivity and sensitivity of the measurements [110, 111]. We first evaluated the selectivity of the microprobe towards dopamine and serotonin over the interference from AA, UA and DOPAC using square wave voltammetry (SWV). **Figure 3.5a** shows minimum current response from UA (10 μM), DOPAC (10 μM), and AA (10 μM) and a higher sensitivity towards dopamine (10 μM). This is likely due to the negatively charged PSS doped inside the PEDOT:PSS film which further repel these anionic interferences approaching the electrode. In vitro detection of dopamine and serotonin concentration was then performed in 1xPBS containing the aforementioned interference species to construct the calibration plot. Potential was held at 0.6 V in 1x PBS for 30 seconds to clean the electrode between different measurements. Baseline removed SWV peak current shows a linear response with NT concentration with a limit of detection of 800 nM for dopamine and 1.2 μM for serotonin (**Figure 3.5b,c**). **Figur 3.5d** demonstrates the microprobe capability of multiplex detection of dopamine and serotonin simultaneously, where individual redox peak could be resolved respectively. This multi-analyte sensing capability is also highly desired due to the complex system *in vivo*.

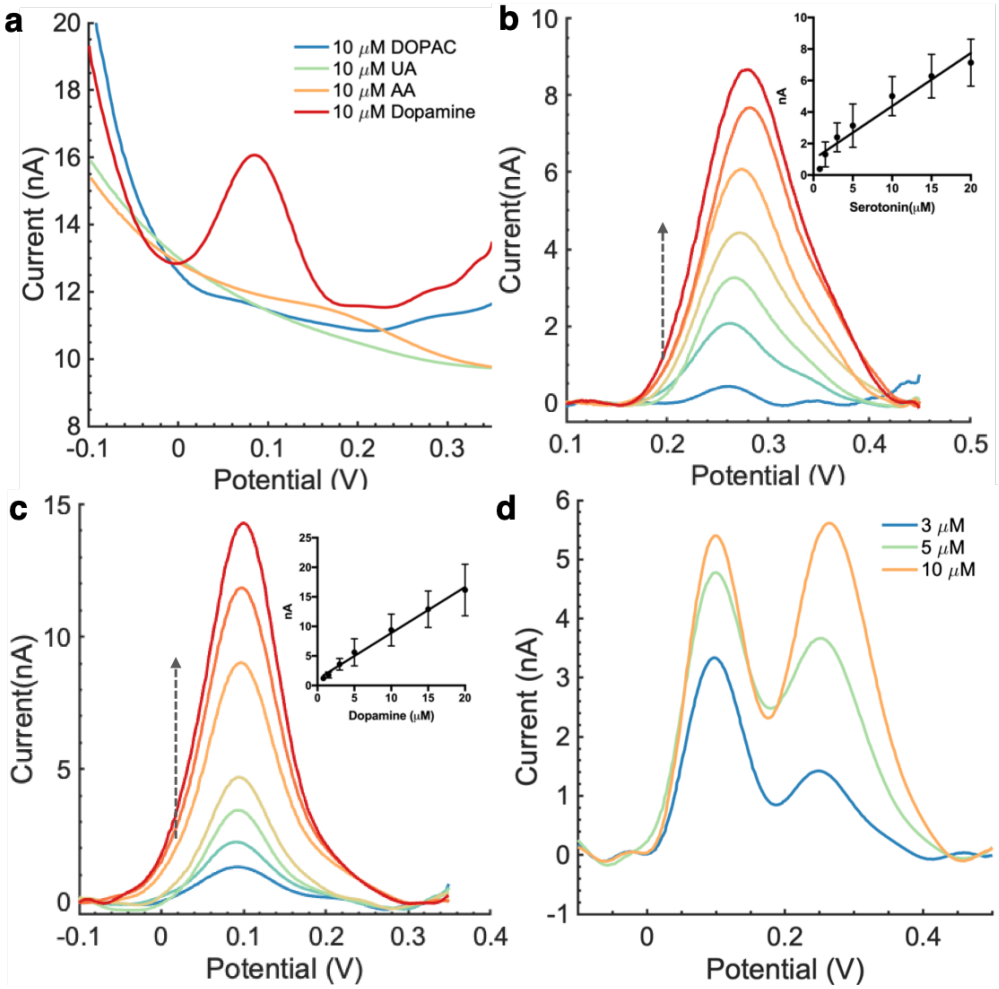

Figure 3.5. Electrochemical detection of dopamine and serotonin using SWV voltammograms. (a) SWV for 10 μM dopamine, UA, AA, DOPAC in 1x PBS solution. (b) SWV of serotonin with various concentration in the interference solution, arrow indicates increasing concentration. Inset shows the linear relationship between serotonin concentration with peak current (Y = 0.3368*X + 1.006), error bar comes from 3 individual probe. (c) SWV of dopamine with various concentration in the interference solution, arrow indicates increasing concentration. Inset shows the linear relationship between dopamine concentration with peak current (Y = 0.7779*X + 1.092), error bar comes from 3 individual probes. (d) Simultaneous detection of serotonin and dopamine in the interference solution with various concentration.

3.3.3 Stability and reusability of PEDOT/electro-optic microprobe for serotonin and dopamine

Reusability and stability of the electrode has been a huge challenge for NT sensing. Electrode fouling due to the strong adsorption of the oxidized byproduct of neurotransmitter

leads to electrode deactivation and increase of impedance which prevents reusable sensor after multiple measurements [112]. Here we investigated the stability of the PEDOT:PSS coated microprobe for NT detection and demonstrated the ability of using anodic treatment to improve its reusability as well as antifouling property. To first access the microprobe stability, 10 consecutive measurements were carried out in dopamine solution (100 μM) and serotonin solution (10 μM). We noticed a minimal change of current after 10 consecutive measurements (**Figure 3.6**). While serotonin shows a higher rate of fouling at higher concentration of 20 μM. This is due to the complex fouling mechanism of serotonin under oxidation which usually makes it much more difficult to detect than dopamine [113]. Serotonin undergoes free-radical polymerization and the oxidation side-product creates a non-conductive coating which blocks further electron transfer [114]. The significant fouling due to site-blocking adsorption of reaction byproducts can also be confirmed via the EIS where nearly 6 times increment of impedance at 1 kHz was observed after testing in serotonin solution (**Figure 3.7**).

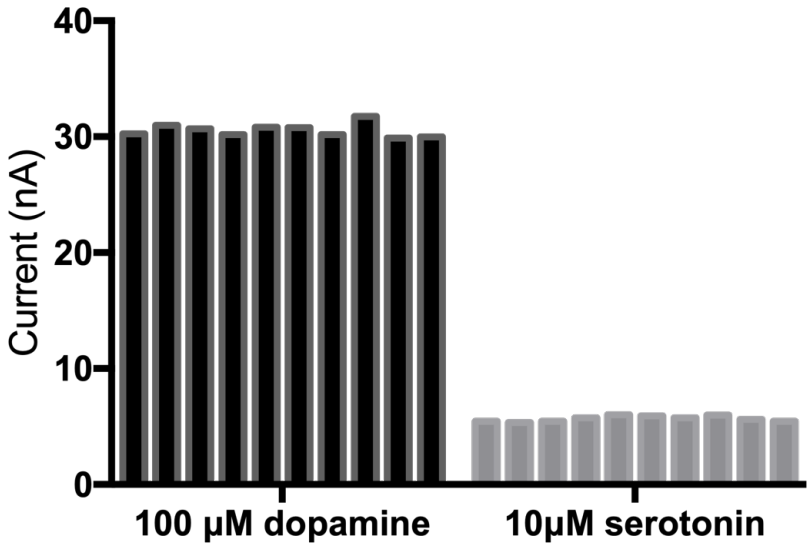

Figure 3.6. SWV peak current for 10 consecutive measurements in 100 μM dopamine solution and 10 μM serotonin solution shows minimal change.

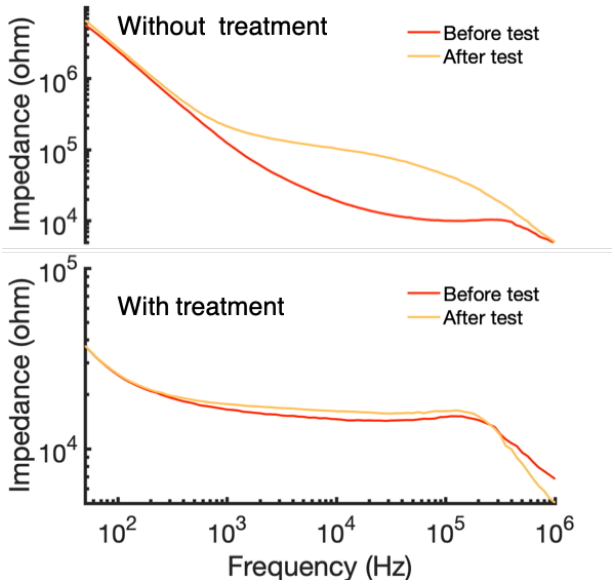

Figure 3.7. EIS before and after 10 consecutive measurements in 20μM serotonin solutions. Upper panel shows nearly 6 times increment of impedance at 1kHz without any treatment. Lower panel shows minimal change of impedance with anodic treatment at 0.6V for 30s in 1x PBS solution between each measurement.

Previously, Nafion or carbon-nanotube (CNT) doped PEDOT has been explored as an anti-fouling coating [113, 115, 116]. However, it's hard to achieve a uniform coating of Nafion on microelectrodes and CNT impose difficulties in processing for uniform dispersion due to its hydrophobicity. Electrochemical activation using single anodic/cathodic potentials or certain pulse trains has also been explored to clean the electrode surface [117]. Duran et al. reported that cathodic treatment for 180s at 250 mA/cm^2 can reactivate diamond microelectrodes for serotonin measurements due to the removing of site-blocking surface carbon-oxygen functionalities [118]. Takmakov et al adopted a repetitive voltammetry sweeping method to cause oxidative etching of carbon microelectrodes to reactivate the surface in fast-scan cyclic voltammetry [119]. However, no detailed work has been done on how conductive polymer coating could be reactivated using electrochemical treatment for microelectrodes. Here, we found the PEDOT:PSS coated microprobe could be reused and reactivated through anodic treatment at 0.6 V which restores both the SWV peak current as well as the impedance of the

microprobe after serotonin fouling.

Figure 3.8a shows the decreasing SWV peak current over consecutive measurements in 20 μM serotonin solution, indicating gradual blocking of electrode surface. The SWV signal was then recovered after reactivating the microprobe in 1xPBS at 0.6V for 30 s. The impedance spectra were also acquired to investigate the activation and desorption process on the electrode during anodic treatment. **Figure 3.8b,c** shows the gradual recovery of impedance while holding the potential at 0.6 V over 470s of treatment. Equivalent circuits have been used to model the electrode-electrolyte interface impedance and different models have been developed for the conductive polymer coating [120, 121, 122]. Modify the conventional Randles circuit with additional diffusion elements were usually used to account for the ionic diffusion and charging of the conductive polymer film [120]. The impedance spectra data were fitted with the proposed equivalent circuit as shown in **Figure 3.8b inset**, where Rs is the electrolyte and contacts resistance, C_{dl} is the double layer capacitance at the electrolyte/PEDOT interface, R_{ct} is the charge transfer resistance, CPE is the constant phase element of the PEDOT coating, Z_D is the finite-length Warburg diffusion element with the following expression [123] :

$$Z_D = \frac{1}{Y_0\sqrt{i\omega}} coth[B\sqrt{i\omega}] \tag{3.1}$$

where Y_0 and B can be acquired through fitting to the equivalent circuit model. The diffusional coefficient could be determined with the following equation: $D/L^2 = 1/\tau_t$ where L is the diffusion length and τ_t is the diffusional time constant. Based on the theoretical expression of the finite-element diffusion element, the diffusional time constant can also be expressed as $\tau_t = B^2$. **Figure3.8d** summarized the trend based on fitting results indicates a decreasing R_{ct} value and an increasing $1/\tau_t$ during the period of anodic treatment. The reduced R_{ct} value over time is likely due to the byproduct desorption process. The fitting result also indicates a faster ion diffusion and exchange within the polymer film that decrease the diffusional time constant which could reactivate its electrochemical property. Using the anodic treatment between or after

measurements, we were able to maintain the electrochemical performance of the microprobe after multiple measurements with minimal change of impedance (**Figure 3.7**)

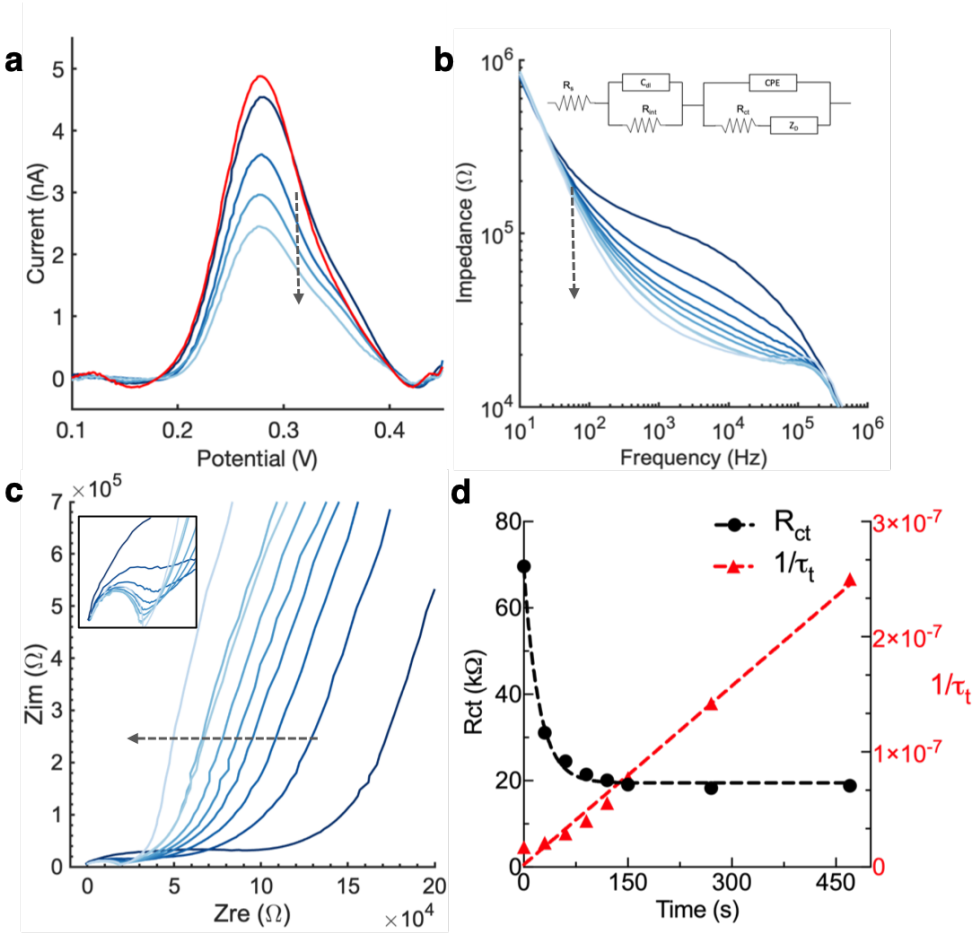

Figure 3.8. EIS and SWV shows microprobe reactivation process through anodic treatment. (a) SWV voltammograms in the 20 μM serotonin solution over multiple measurements with arrow indicating a decreasing current. The signal was then recovered after anodic treatment at 0.6V for 30 s indicated in the red curve. (b) EIS change over time while holding the microprobe at 0.6 V with arrow indicating a decreasing impedance over time. Inset: equivalent circuit model. (c) Nyquist plot change over time while holding the microprobe at 0.6V with arrow indicating a decreasing semicircle diameter. Inset: zoom in area at high frequency region. (d) R_{ct} value and diffusional time constant extracted from the equivalent circuit model plotted as a function of time of anodic treatment shows decreasing electron transfer resistance (R_{ct}) and increasing diffusion constant ($D \propto 1/\tau_t$).

3.3.4 Localized spectroscopic recording

We then evaluated the localized spectroscopic recording capability of the microprobe. Localized light collection was first demonstrated by lowering the microprobe into the fluorescein salt solution excited by a 442 nm laser. The microprobe was mounted on a probe holder precisely controlled by a micro manipulator. Once the microprobe was elevated from the solution by 2 μm, drastic change of spectrum was observed as shown in **Figure 3.9a**. This result confirmed that the microprobe could carry out fluorescent collection and the spectrum acquired was localized at the tip of the microprobe. We then experimentally profiled the optical spatial resolution of the microprobe by scanning it across a single fluorescent bead (d = 45μm). The fluorescent bead was first dried on the glass slides. A thin PDMS spacer was placed on top of it with a thin layer of water to reduce the mismatch of refractive index for light collection purpose. The microprobe was precisely controlled with a micro manipulator and the position while moving was monitored. Fluorescent intensity was then integrated from 450nm to 500nm from the acquired spectrum (**Figure 3.9b**). Figure 4b shows the normalized intensity profiled along one axis with a full width half maximum (FWHM) of 22μm.

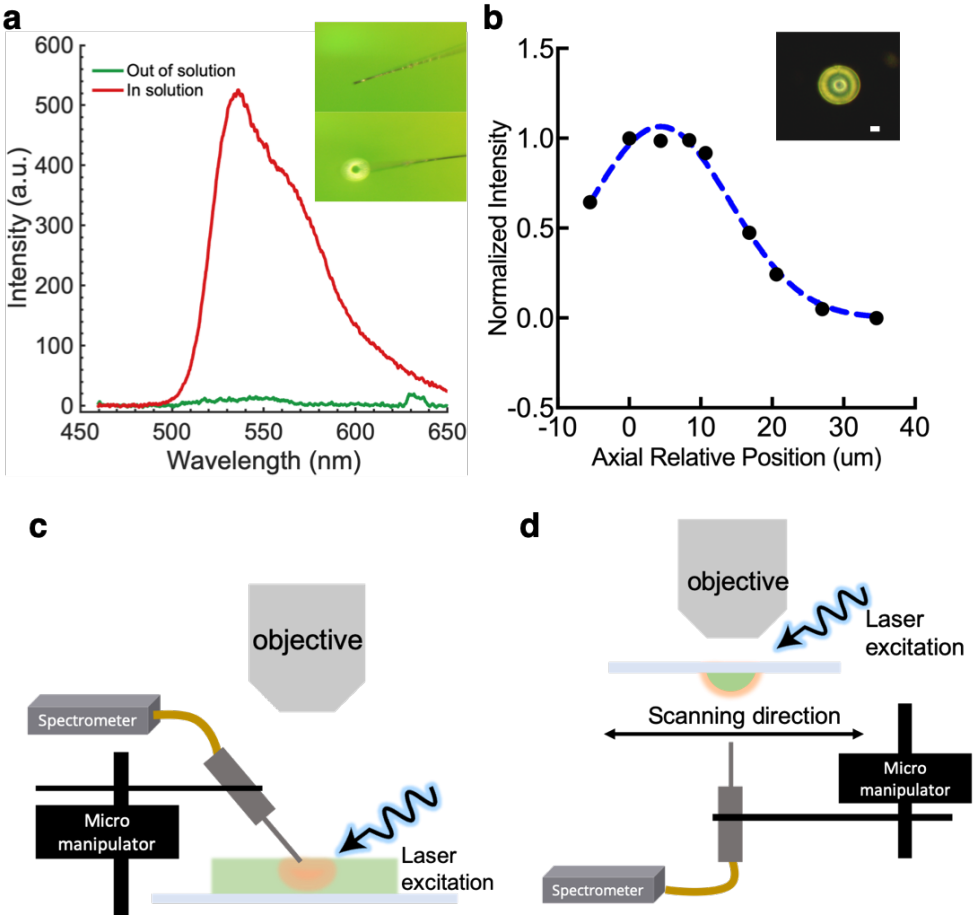

Figure 3.9. Localized optical spectroscopic recording of the microprobe (a) Fluorescent spectrum in 1mM fluorescein salt solution recorded with the microprobe. Inset: optical image shows the microprobe in and out of the fluorescein solution with 2μm in height difference. (b) Normalized fluorescent intensity profiles as a function of axial displacement from a single micro fluorescent bead. Inset: optical image of the microbead, scale bar is 10 μm. (c) Setup for fluorescent measurement in the fluorescein salt solution. (d) Setup for profiling the spatial resolution of the microprobe along a fluorescent microbead.

3.3.5 Spectroelectrochemical sensing of electrochromic materials

Finally, we demonstrated the capability of using the electro-optic microprobe as a spectroelectrochemical (SEC) sensor, using the electrochromic behavior of PEDOT and MB as our model systems. Electrochromic behavior of PEDOT coating on the microprobe end facet was evaluated as our first model system. Neutral PEDOT shows strong absorption in the visible wavelength due to the $\pi - \pi^*$ inter-band transition, producing a deep blue color. Upon

oxidation, low energy charge carriers shift the absorption to IR region and the film turns light blue [124]. While applying voltage, ion transport from electrolyte to the polymer matrix alters the doping level and the color contrast between the undoped and the doped state is related to the polymer band gap [125, 126, 127]. **Figure 3.10** shows the SEC cell setup in a homebuilt faraday cage, in which a Xenon fiber light source was introduced from beneath through a glass slide. A 650 nm short pass filter was placed on top of the light source to eliminate higher wavelength interference due to the small diameter of the microfiber optic. Potential was applied in a three-electrode setup and the spectrum was acquired simultaneously.

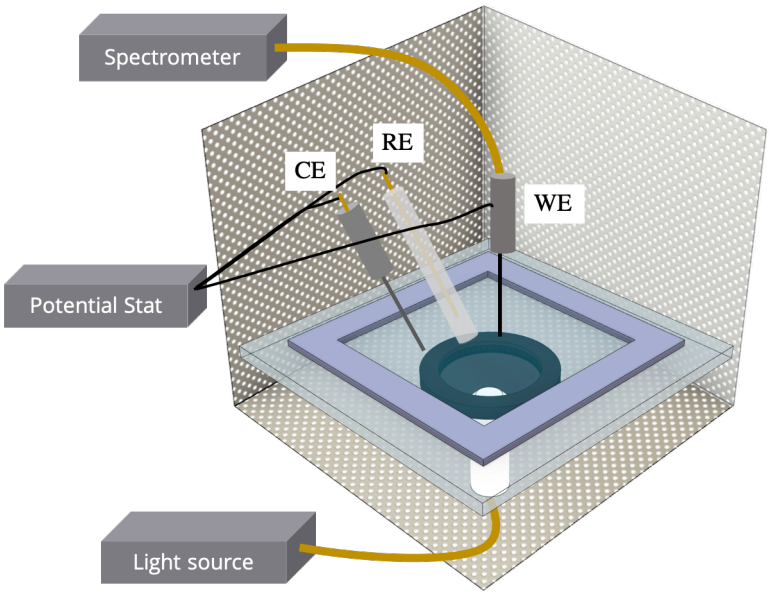

Figure 3.10. Schematic of the SEC setup using the microprobe as the working electrode and for spectral recording at the same time. A 650 nm short pass filter was placed on top of the light source to eliminate higher wavelength interference.

The microprobe was able to capture the reversible spectral change through repeated doping and de-doping process over multiple CV cycles under different potential waveform (**Figure 3.11**). **Figure 3.12** shows the relative transmittance change at different applied potential from -0.6 V (de-doping state) to 0.6 V (doping state) in 1x PBS solution. We were also able to derive a switching time of 2.05 s for 90% change of transmittance from de-doped

state to the doping state in the square wave modulated spectral change. CV rate dependent transmittance change was then investigated. **Figure 3.13** shows the rate dependent change of relative transmittance over 4 CV cycles. Charge intensity was derived through integration of the CV curves at different scan rate and shows a proportional change with the optical contrast (**Figure 3.13b**). The results indicate that higher charge injected at lower scan rate could increase the optical contrast.

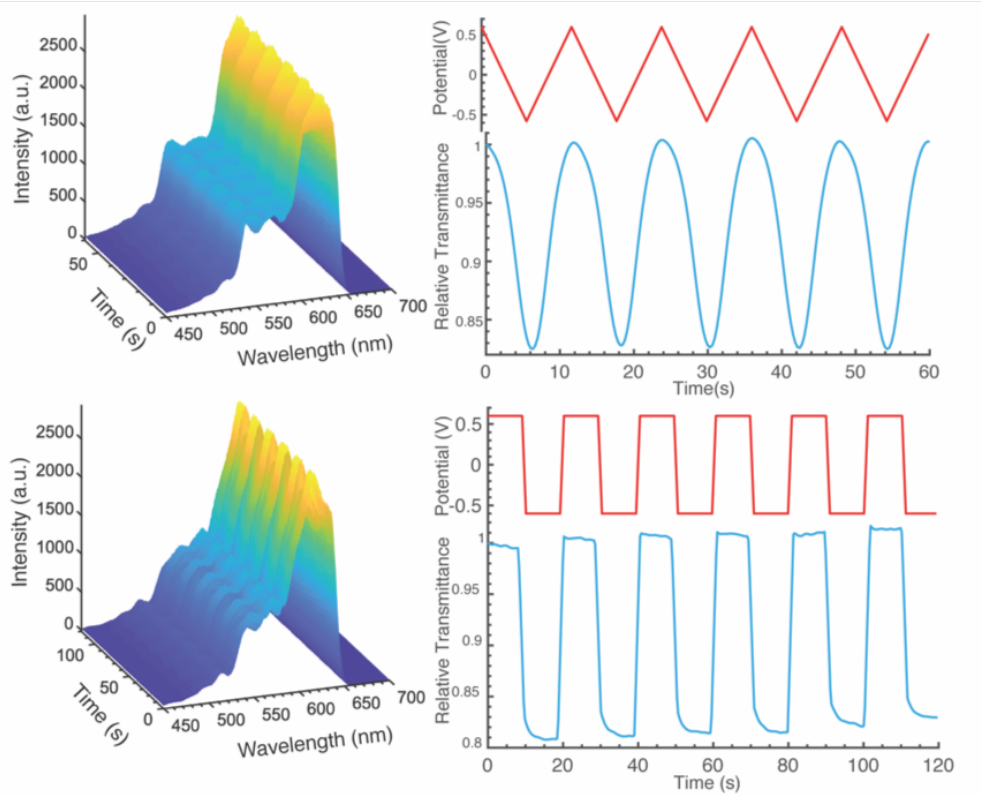

Figure 3.11. Reversible spectral change over multiple potential sweeping cycles using triangular wave (up) and square wave (bottom). The red curve is the applied potential during 5 cycles and the blue curve is the relative transmittance change acquired from the peak intensity of the spectrum.

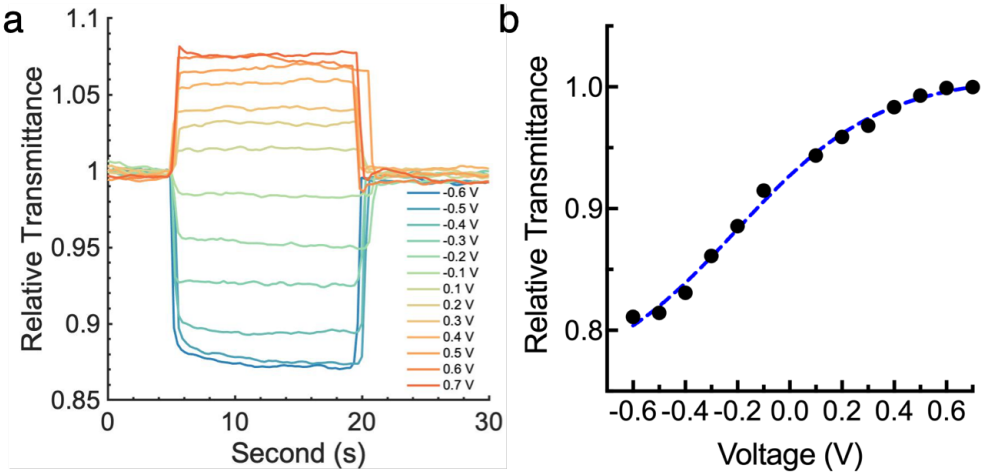

Figure 3.12. Relative transmittance as a function of applied potential. (a) Relative transmittance change over 15 seconds hold at various potentials. (b) Relative transmittance as a function of applied potential.

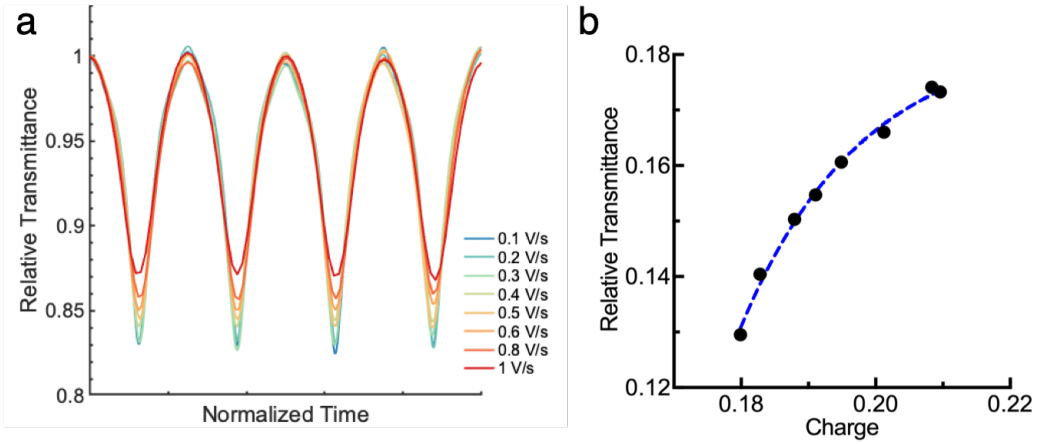

Figure 3.13. Relative transmittance as a function of sweeping rate. (a) Relative transmittance change over multiple cycles at different sweeping rate. (b) Optical contrast at various scan rate as a function of total charge injected in each cycle.

Methylene blue (MB) was then selected to interrogate the spectroelectrochemistry response of the microprobe in a free solution. When applied negative potential, MB was reduced to leucomethylene blue and switched from colored state to the colorless state [41]. Applying cyclic potential from 0.6 V to -0.6 V at a rate of 0.2 V/s and evaluating both

the spectral properties along with the cyclic voltammogram provides information about the mixed electrochemical behavior of MB on PEDOT. **Figure 3.14a** shows the spectral response composed of four regions in each cycle. **Figure 3.14b** shows the well-defined oxidation and reduction peaks that corresponded to the MB redox reaction. In region I (0.6V ˜ 0 V), decreasing transmittance arise from the reduction of PEDOT film which gradually turned into a colored state. In region II (0V ˜ -0.38V), first peak starts to arise due to the reduction of MB to a colorless state that increased the overall relative transmittance. In region III (-0.38V ˜ -0.6V ˜ -0.47V), MB was depleted near the electrode surface and PEDOT reduction takes the dominant role which keeps decreasing the transmittance. In region IV (-0.47V ˜ 0.6V), increasing transmittance was due to the mixed behavior of PEDOT oxidation (colorless state) and MB oxidation (colored state). Rate dependent spectral change was also investigated as shown in **Figure 3.14c**. Both peak1 (region II) and peak2 (region II) change proportionally with the scan rate (**Figure 3.14d**). At a higher scan rate, optical signal modulation increased for peak1 while decreased for peak2 because of more MB involved in the electron transfer process with a decreasing diffusion layer. The rate-dependent study indicates the inherent difference of the electrochromic mechanism between a conjugated polymer (PEDOT) and a redox dye (MB). The optical modulation for PEDOT is majorly dependent on the amount of charge carrier introduced which alters the doping level and further change the optical contrast, while for MB, the optical modulation is majorly dependent on the amount of MB being reduced or oxidized near the electrode surface.

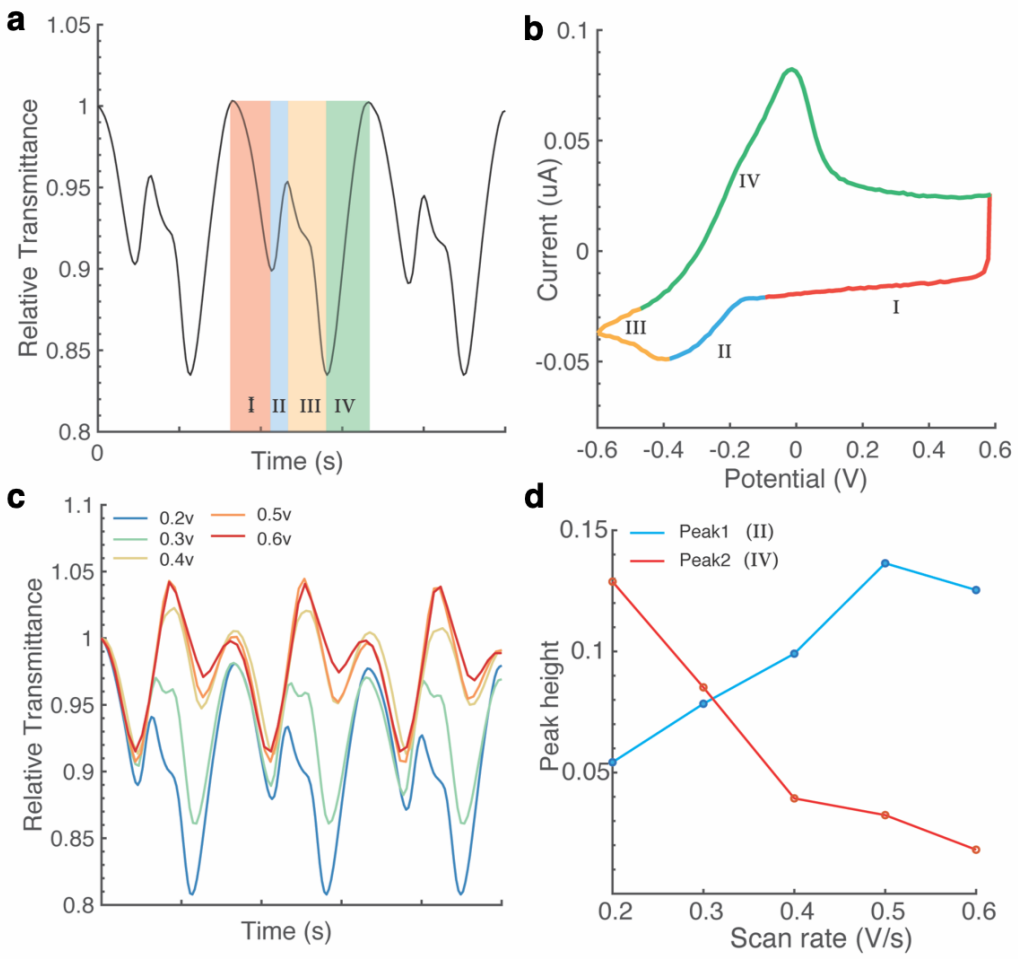

Figure 3.14. Spectroelectrochemical measurement in MB solution (a) Relative transmittance change over 3 cycles of CV in MB solution from 0.6V to -0.6V (scan rate 0.2 V/s) shows four regions of change. (b) Cyclic voltammogram for one CV cycle in MB solution shows well defined redox peaks. (c) Relative transmittance change at different scan rate during 3 CV cycles. (d) Peak height extracted from region II and region IV as a function of scan rate.

3.4 Conclusion

3.4.1 Limitation and future work

We have demonstrated localized fluorescence spectroscopy recording and SEC sensing capability of the multifunctional electro-optic microprobe. Currently it still requires an external light source for excitation or light delivery. We hope to further expand this work to simultaneous

delivery and collection of the light, which could be achieved using a y-splitter fiber coupler with one leg connected to the laser/excitation source and another leg connected to the spectrometer. While several issues need to be resolved before continuing with the new configuration. In most y-splitter couplers, an internal termination is installed at the junction to reduce back reflection of the laser source that would reduce the light collection efficiency. Nevertheless, considerable amount of light from the excitation source would still be reflected back to the spectrometer and contribute to the noise level as well. Thus, certain filter should be placed before the final spectra collection port to increase the signal-to-noise ratio of the acquired data, as well as to protect the CCD camera in the spectrometer from photo damage due to the much higher power of the laser source. **Figure 3.15a** shows the setup that could be applied to acquire fluorescence spectrum using a y-splitter, in which a 460 nm long-pass filter was positioned in front of the spectrometer entrance slit and the input fiber bundle was fixed on a X-Z translational stage to align the fiber with the entrance slit. Mercury pen lamp was used to calibrate the spectrum and to align the fiber bundle with the entrance slit at first. **Figure 3.15b** shows the acquired fluorescence spectrum using the electro-optic microprobe in the 1mM fluorescein salt solution. The 442 nm laser was coupled to one leg of the y-splitter, and the other leg was connected to the fiber bundle that goes into the spectrometer. In order to improve the coupling efficiency, other wavelength division multiplexer that could combine or split light at two different wavelengths could be used to further improve the signal-to-noise ratio.

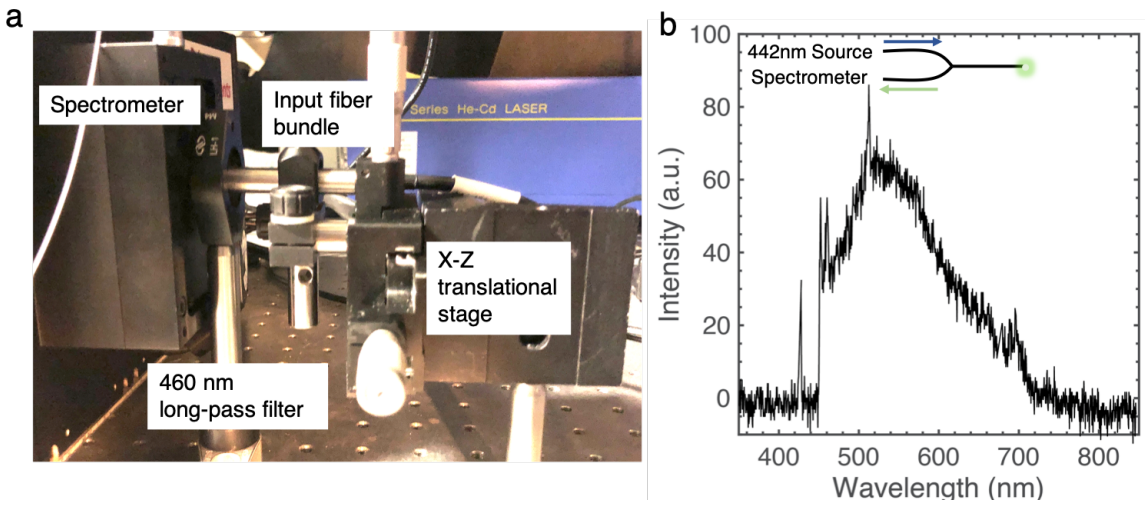

Figure 3.15. (a) Photo of spectrometer setup for simultaneous excitation and emission using a y-splitter coupled electro-optic microprobe. (b) Fluorescence spectrum acquired in fluorescien salt solution while simultaneous excited using a y-splitter coupler.

3.4.2 Summary

In this chapter, we developed a multifunctional microprobe of small footprint (˜ 10 μm), with the ability to carry out electrochemical neurotransmitter detection and localized spectroscopic recording. The transparent PEDOT:PSS coating significantly enhanced the electrochemical performance of the microprobe that allows sensitive and selective neurotransmitter detection. We were able to achieve a LOD of 800 nM, and 1.2 μM for dopamine and serotonin respectively with a minimal electrode fouling using an anodic treatment method. Merits of the multifunctional sensing pathways were demonstrated through a microfiber based spectroelectrochemcial platform that could capture the spectral change during an electrochemical process for various redox active species. We hope to further expand this work to simultaneous delivery and collection of the light using a y-splitter fiber coupler. This would eliminate the use of an external light source and translate the readily characterized platform to more versatile in vivo applications.

3.5 Acknowledgement

Chapter 3, in part, is a being prepared for submission of the material ”Multifunctional microfiber based-electrochemical, optical and spectro-electrochemical sensor” with authors of Yuesong Shi, Spencer Ward, Conor Riley, and Donald J. Sirbuly. The dissertation author is the primary investigator and author of this material.

Chapter 4

A fiber-based electrochemical sensor for heparin detection

The ability to rapidly and accurately maintain the anticoagulant heparin in the therapeutic window is critical in a variety of inpatient settings. Unfortunately, this is quite challenging due to the narrow therapeutic window and heterogenous molecular weight of heparin; thus, heparin dosing is the second most common intensive care unit (ICU) medication error. Common detection methods suffer from long turnaround times and indirect measurements of heparin activity. Electrochemistry has allowed simple electrical readout and rapid in-situ detection. The objective is to develop a miniaturized and flexible electrochemical sensor for the detection of heparin. With the combination of a reduced electrode size, the goal is to explore applications for real-time in vivo sensing of heparin.

4.1 Introduction

Heparin is a widely used anticoagulant in surgery, intensive care, and thrombosis [128]. Heparin is attractive because of its short circulation half-life, easy access, and low cost [129]. However, heparin has a very narrow therapeutic window, a broad range of molecular weights (3-30 kDa), and widely varying pharmacokinetics [129, 130, 131]. Thus, maintaining heparin in the therapeutic window is challenging, and mismanagement can lead to hemorrhage or thrombosis. The most commonly used method to monitor the effect of heparin is the activated

partial thromboplastin time (aPTT), but this is an indirect measurement of heparin's in vivo activity [132]. Furthermore, the aPTT has a fluctuating baseline range and exhibits poor correlation with the actual dose [133]. The activated clotting time (ACT) has utility during surgery but is operator-intensive and requires large blood volumes [134]. Other tools like anti-factor Xa offer more functional insight but are rarely used in routine clinical practice [135]. Importantly, all of these in vitro diagnostic tests suffer from a long turnaround time and require invasive blood sampling [136]. Thus, there is an unmet need for rapid and accurate tools to monitor heparin during anticoagulation therapy—needs that electrochemistry readily satisfies. Several groups have reported the electrochemical detection of heparin but relatively few have demonstrated sensing capability under biologically relevant conditions or in whole blood [137, 138, 139, 140]. Other electrochemical approaches either require ferricyanide in the test solution as a redox indicator [141, 142], an external protamine sulfate titration with lengthy assay time [143], or involve complex fabrication using bulk planar electrodes as a support [144]. These requirements limit their utility for real-time on-site measurements. Cationic dye binding heparin assays have been used in biochemical and clinical laboratories. The transduction mechanism is based on the electrostatic interactions between a positively charged phenothiazinium dye molecule and the polysulfated heparin backbone. Given the electrochemical activity of these dyes, we investigated the electrochemical response for heparin detection. Although heparin alone is not a redox active species, the interaction between heparin and a cationic dye can be expected to alter the electrochemical response compared to the free dye and allow rapid monitoring of heparin concentrations.

4.2 Electrochemical response of dye-heparin interaction in buffer, plasma and blood

4.2.1 Materials and Experimental part

A various of phenoxazine dyes were tested in buffer solution and plasma including: Methylene blue (MB), Nile blue (NB), Azure A, Azure B, Azure C, 1,9-dimethyl-methylene blue (DMB) and Toluidine blue (TBO). All dyes were prepared at a concentration of 0.5 mM in either pH = 5.8, 0.1M phosphate buffer solution or pooled human plasma (Innovative Research), or human whole blood. Blood was obtained from a healthy donor according to IRB guidelines.

4.2.2 Results and Discussion

We first used square wave voltammetry (SWV) to investigate the interaction of the phenoxazine dye molecule with heparin using a glassy carbon electrode (GCE). The heparin-dye complex is non-electroactive which resulted in a decrease of peak current from the voltammetry. **Figure 4.1** shows the chemical structures of heparin and 7 cationic dyes used in the experiment and **Figure 4.2** shows the SWV electrochemical response of different cationic dyes to heparin in buffer solution at various concentration. It is evident that with heparin titration, the SWV peak current start to decrease, while the sensitivity and initial peak current is different for different dyes tested. In order to further understand how other charged species in plasma would interfere with the response, the electrochemical response was also evaluated in human pooled plasma. **Figure 4.3** summarized the calibration plot for all dyes tested in the buffer solution and in the pooled human plasma.

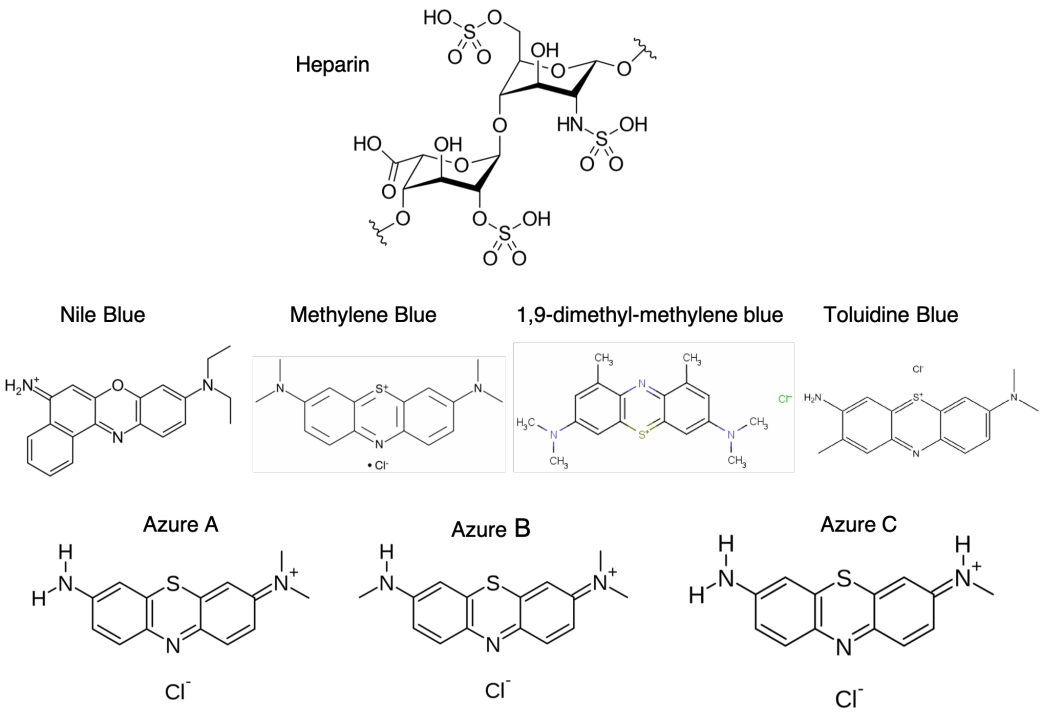

Figure 4.1. Chemical structure for Heparin and 7 cationic dyes tested in the experiments

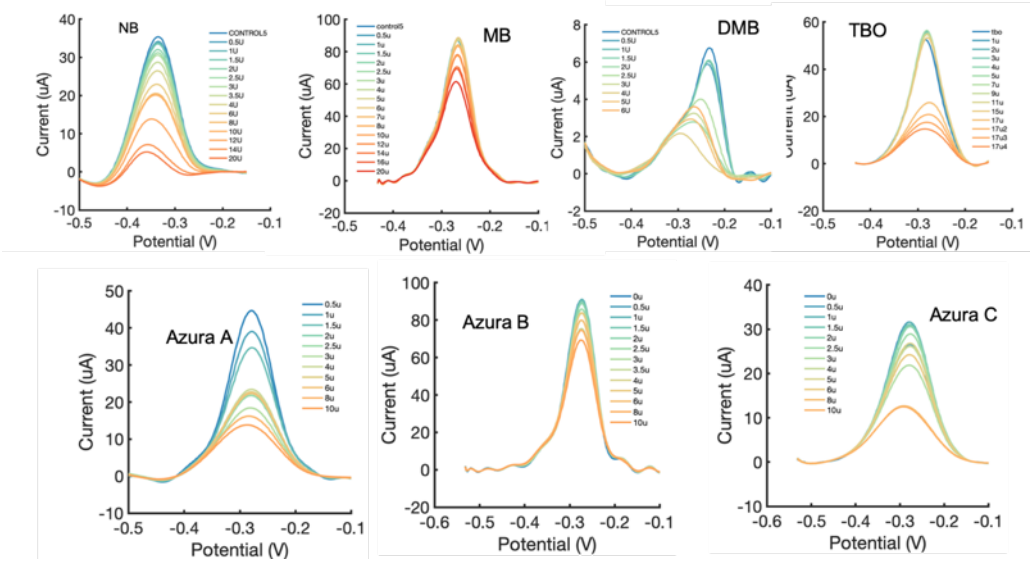

Figure 4.2. SWV response to heparin at various concentration for 7 cationic dyes tested in pH = 5.8 phosphate buffer using a GCE electrode.

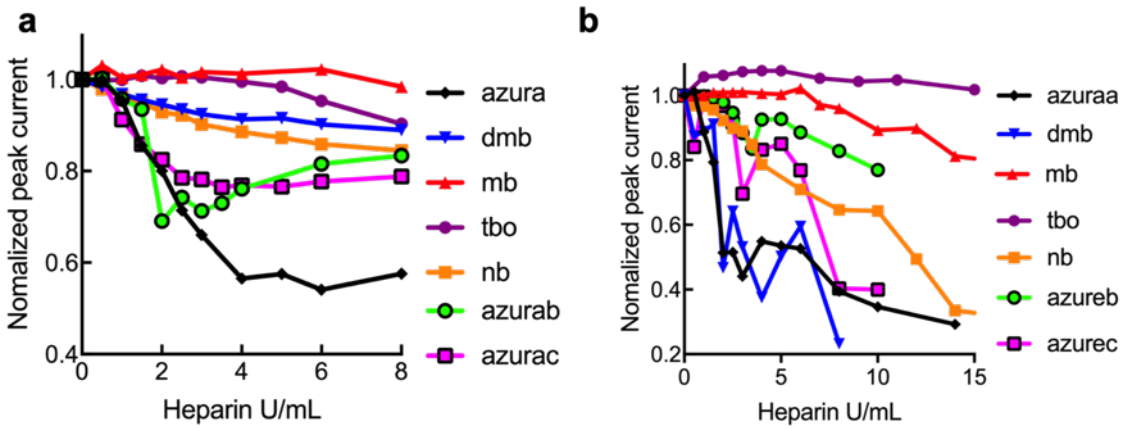

Figure 4.3. Calibration plot of different cationic dyes to heparin. (a) Electrochemical response to heparin in the human pooled plasma. (b) Electrochemical response to heparin in the buffer solution.

Sensitivity to heparin of different dyes in plasma and buffer solution were then acquired from the calibration plot. As shown in **Figure 4.4a**, Azure A shows the highest sensitivity to heparin in plasma in the range of 0 U/mL ~ 4 U/mL. TBO and MB were not sensitive to heparin in either plasma nor buffer solution within the same dynamic range. Heparin response at higher concentration in the buffer solution was also evaluated as shown in **Figure 4.4b**. Azure A, NB and DMB shows higher sensitive below 4 U/mL, while MB and TBO are only sensitive to heparin above 4 U/mL. In general, sensitivity in buffer shows a higher sensitivity than plasma, due to the less interference and charged agents in the environment for competitive binding.

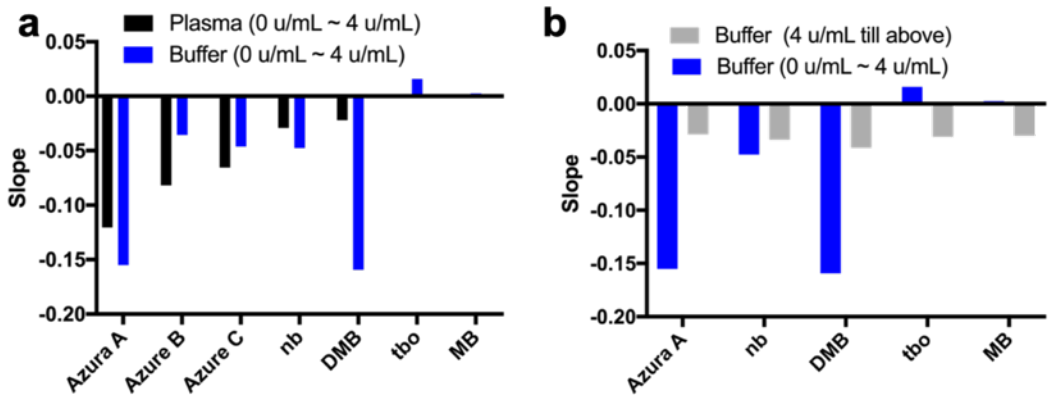

Figure 4.4. Slope of calibration plot within different dynamic range for various dyes.

Azure A was then selected to test in blood due to its higher sensitivity, and more linear response to heparin in the plasma solution. The hematocrit level of the whole blood was also adjusted to evaluate its response. **Figure 4.5** shows the SWV response of Azure A to heparin in human whole blood. **Figure 4.6** summarized and compared the response curve to heparin in whole blood of different hematocrit level. The results indicate that the response decrease with higher concentration of red blood cells. This could be due to the following reasons: 1) The higher hematocrit blood has higher viscosity and the Azure A was not dissolved uniformly. 2) The higher viscosity of high hematocrit blood needs longer incubation time for heparin and dye binding due to suppressed diffusivity. 3) High RBC level decrease the ionic strength for the sample and has the lowest peak which renders lower sensitivity.

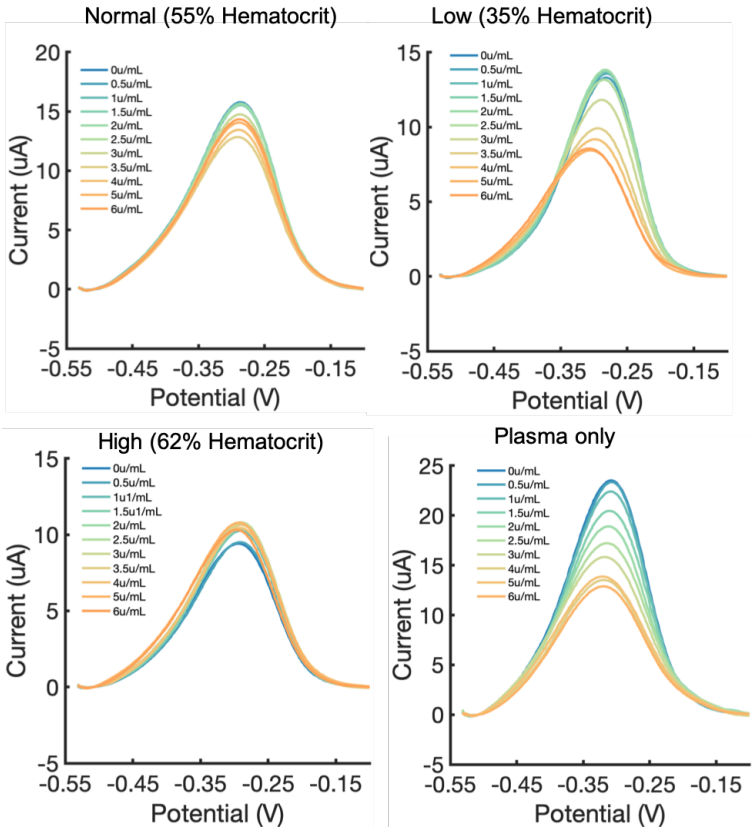

Figure 4.5. SWV response of Azure A to heparin at various concentration in blood and plasma using the GCE electrode.

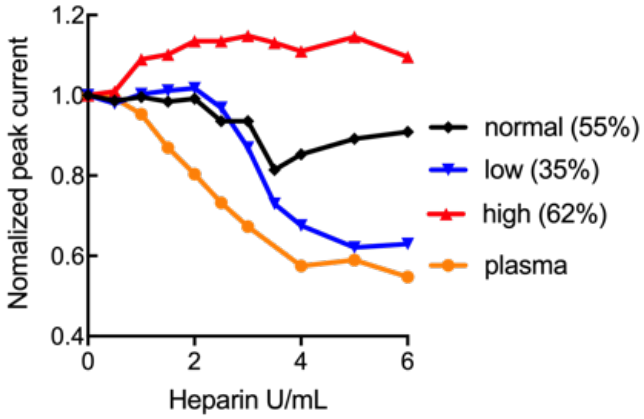

Figure 4.6. Calibration plot of Azure A to heparin in blood of different hematocrit level and plasma.

4.3 Dye immobilization method and stability evaluation on miniaturized fiber electrode

4.3.1 Overview

To move away from the requirement of having free dye in solution near the electrode, direct immobilization of the dye on a flexible microfiber electrode was investigated. This could be achieved through a conductive layer of PEDOT:PSS or PEDO-CNT:PSS coating on a flexible micro fiber optic, which offers a porous medium for ion transport and facilitates the immobilization of the heparin-complexing cationic dyes. The dye immobilization methods and its stability are evaluated in this section.

4.3.2 Fiber electrode fabrication

Flexible electrodes were fabricated using a multimode fiber optic (FG105UCA, Thorlabs) with a 250 μm diameter. The desired length was cleaved with a ceramic fiber scribe before metal deposition. The fibers were first activated and cleaned with oxygen plasma (Plasma Etch PE100) at a power of 100 W for 3 mins and then placed vertically in a sputtering chamber (Denton 18). Next, 200 nm of Pt was deposited using a 20 nm thick Cr adhesion layer. For PEDOT: PSS coating, 25 μM PSS solution was sonicated for 1 hour and then the EDOT solution (1 μL/mL) was added. For PEDOT-CNT:PSS coating, 1 mg/mL CNT was additionally added to the mixture. The polymer solution was sonicated for another 2 hours to ensure a uniform dispersion. The composite was electropolymerized on the metal coated fiber working electrode potentiostatically at 1.056 V (reference to Ag/AgCl) for 40 seconds. The depth of the probe in the polymer and NB solution during the fabrication process was monitored via a side-view stereoscope to control the amount of deposition on the probe.

4.3.3 Active dye immobilization and characterization

Direct immobilization of the dyes in the porous electrode layer could be achieved through multi-cycle cyclic voltammetry. As the working electrode is cycled, conductive composite layer would help facilitate transport of ions and other molecules from the bulk electrolyte onto the electrode surface. **Figure 4.7a** shows the progressively increasing current at -0.25 V during NB cycling with PEDOT-CNT/PSS coating indicating that the dye is accumulating on the electrode surface. For the bare electrodes, steady current was observed during 30 cycles further confirms that PEDOT layer serves as an essential supporting matrix for effective dye loading (**Figure 4.7b**). Successful NB loading was verified through square wave voltammetry (SWV) in blank PBS buffer (**Figure 4.7c**) where a significant peak was observed after NB accumulation. To quantify the NB loading concentration, the electrode was immersed in methanol for 10 mins to release the NB into solution, so UV-Vis absorption spectroscopy could be performed. The absorption data strongly correlates with the SWV peak current (**Figure 4.7d**) and using a standard curve for NB of known concentration in methanol we estimate that 0.92± 0.1 nmol of NB is adsorbed on the electrode (n = 3 electrodes). After removing the probe from methanol, NB can be quickly re-adsorbed following the same multi-cycle CV protocols (**Figure 4.7e**).

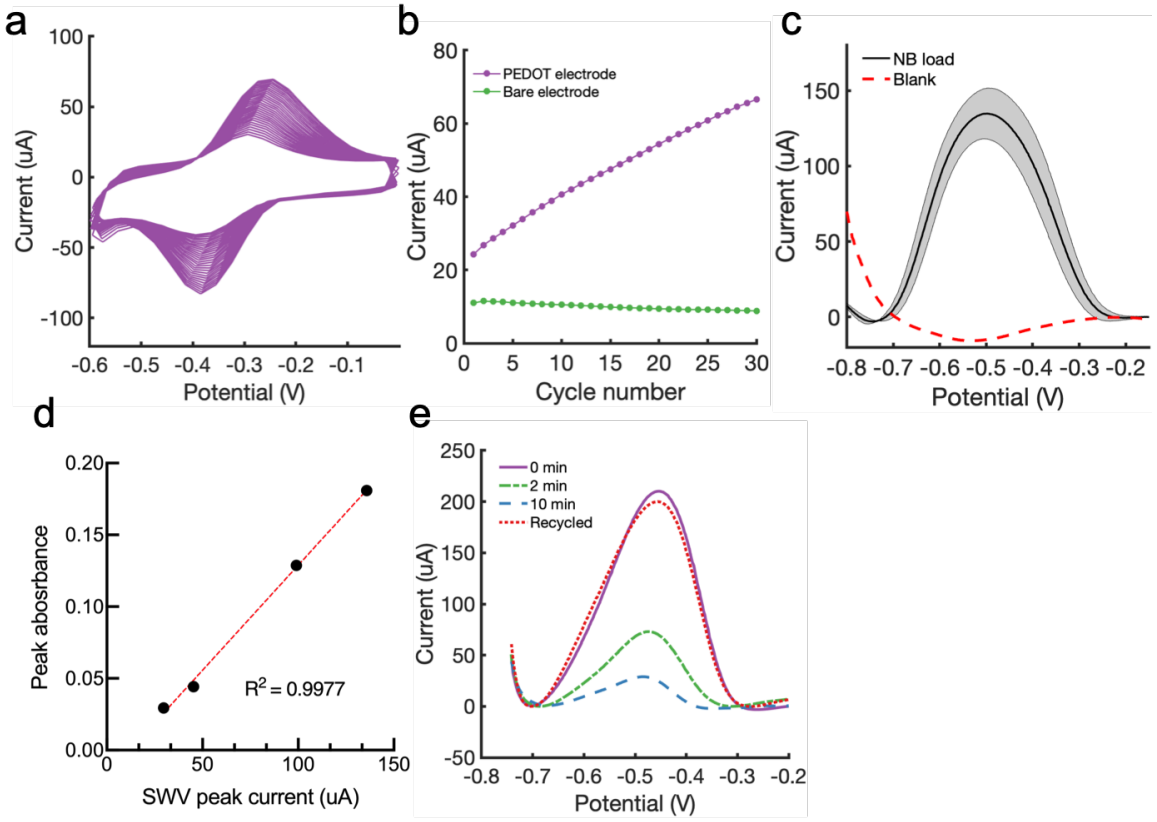

Figure 4.7. Dye immobilization on fiber electrode (a) Progressive cyclic voltammograms over 30 cycles with PEDOT-CNT/PSS coating in 0.5 mM NB solution at a scan rate of 0.1 V/s. Increasing current indicates the inclusion of NB. (b) Peak current change over 30 cycles for PEDOT coated electrode and the bare electrode. (c) SWV in PBS after NB accumulation where the shaded area indicates the standard error from 3 electrodes. The red dashed line represents the blank baseline before NB loading. (d) UV-Vis absorbance of the release NB is highly correlate with SWV peak current. (e) Release of NB as a function of time in methanol. The NB can be re-loaded by removing from the methanol and repeating the multi-cycle CV (red dashed line).

PEDOT-CNT:PSS film thickness could also be controlled through varying the electropolymerization time and we noticed that the NB loading concentration is independent of the film thickness. **Figure 4.8a-d** shows the SEM images of the fiber electrode cross-section with the PEDOT-CNT:PSS deposited for different length of time (8s, 20s, 40s, 60s) with 60 nm, 83 nm, 115 nm, and 208 nm of thickness respectively. As shown in **Figure 4.8e**, probe insertion depth into the NB solution was stringently controlled through a fitted stopper to

eliminate variation from immersion depth. **Figure 4.8f** shows that the SWV peak current in blank PBS buffer after following the same NB accumulation procedure is independent of the electropolymerization time. This result suggest that the dye molecules are likely strongly absorbed on the surface of the electrode and were not penetrated through the film.

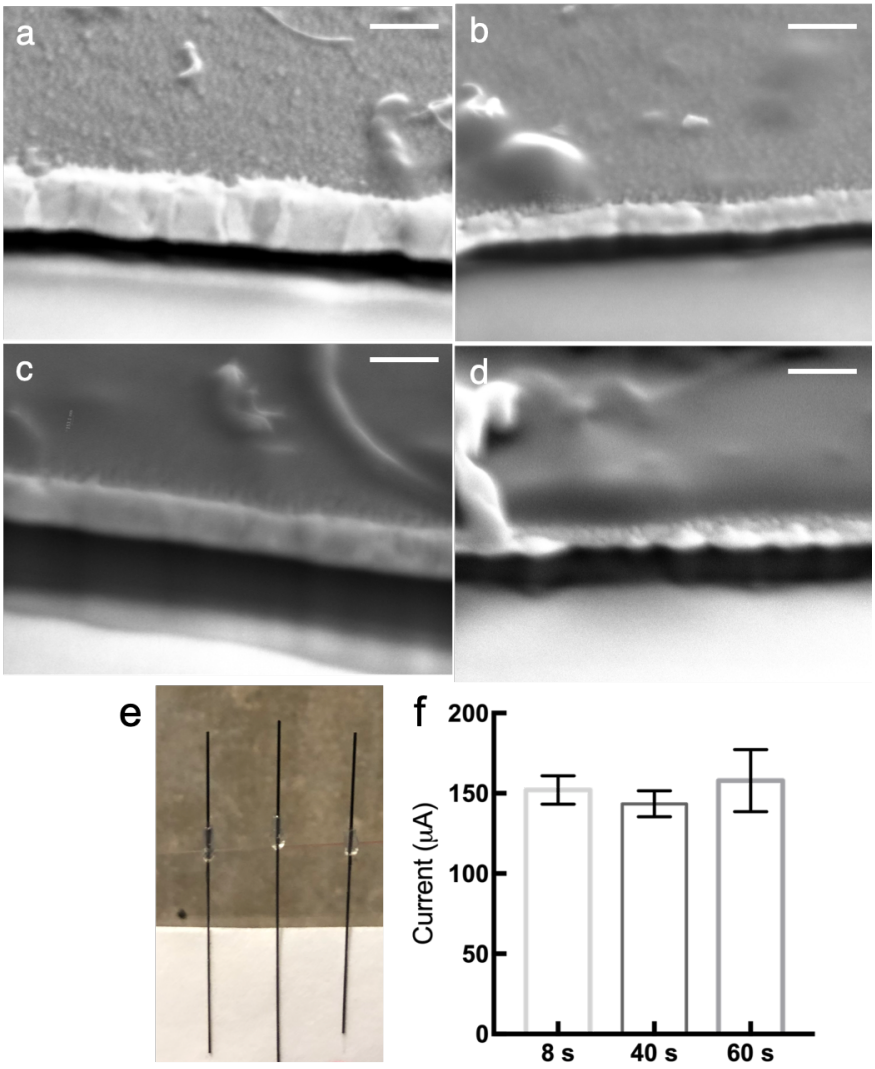

Figure 4.8. (a-d) SEM images of PEDOT-CNT film cross-section with different electropolymerization time (8s, 20s, 40s, 60s). Scale bar is 500 nm. (e) Photo of test probes with threaded tubing to control the insertion depth. (f) SWV peak current of NB loaded on PEDOT-CNT film with different electrodeposition time.

Electrochemical kinetic studies of the accumulated NB were then analyzed through

CV. **Figure 4.9a** displays the CVs of a representative PEDOT-CNT/NB fiber electrode in a 0.1 M PBS solution at various scan rates. Log-log plots of the scan rate versus peak current were used to better analyze the electrochemical kinetic experiments (**Figure 4.9b**). A slope of 0.5 and 1.0 indicates a diffusion-controlled and an adsorption-controlled reaction, respectively, while a slope in between indicates that the reaction has a mixed behavior of both processes [145]. The latter is what we see in our data (slopes of 0.65 and 0.63 for the cathodic and anodic peak currents, respectively) after subtracting the capacitive current, indicating our modified electrodes have a mixed behavior of adsorption and diffusion-controlled processes with a lean towards diffusional kinetics. Integrating the cathodic peaks can be used to estimate the coverage of NB on the electrode which yields a density of 14 $nmol/cm^2$. This concentration is 20% lower than that determined by the UV-Vis measurements. The discrepancy likely comes from the fact that not all of the densely adsorbed NB molecules contribute to the redox reaction (e.g., dye molecules further away from the electrode surface). The electron transfer rate (K_{ET}) can be determined using the equation:

$$K_{ET} = \frac{\alpha n F v_c}{RT} = \frac{(1-\alpha) n F v_a}{RT} \tag{4.1}$$

where R is the ideal gas constant, T is the temperature, v_a and v_c are the x intercepts of the anodic and cathodic curves (from **Figure 4.9c**), respectively, and α is the electron transfer coefficient (derived from the slope of log(v) vs E_{pc} and found to be 0.64) [146, 147]. Using this expression, a rate of 509 s^{-1} and 171 s^{-1} was derived for the cathodic and anodic reactions, respectively. These values are much larger than the values reported for NB adsorbed on graphite or gold electrodes (19 ~ 31 s^{-1}) [148, 149]. These results indicate that the PEDOT-CNT coating can facilitate fast electron transfer between the redox molecule and the electrode even with a dense NB loading—this is likely due to the high interconnected network of channels within the electrode layer that enhance ion transport and surface redox activity.

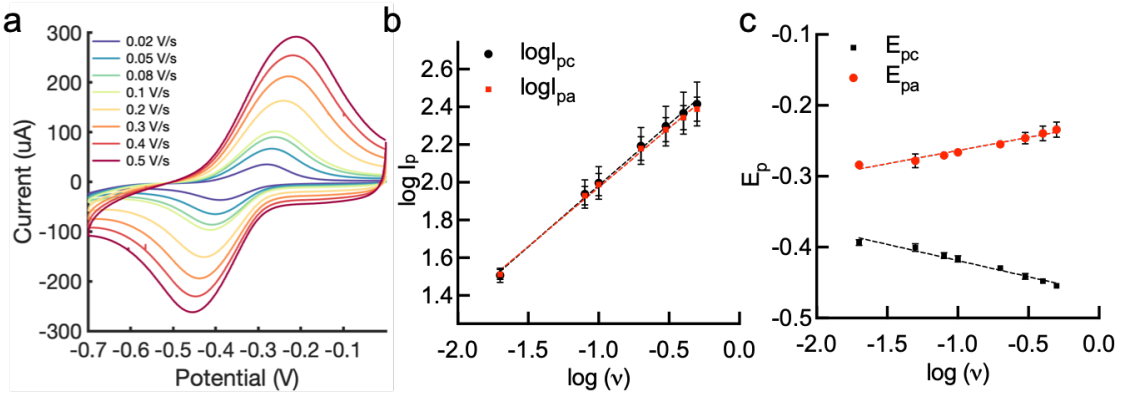

Figure 4.9. Electrochemical kinetics of immobilized dye on fiber electrode. (a) CVs of the PEDOT-CNT/NB fiber electrode at various scan rate. (b) Log-log plot of the anodic I_{pa} (linear fit Y = 0.63*x + 2.60, R^2= 0.99) and cathodic I_{pc} (linear fit Y = 0.65*x + 2.63, R^2 = 0.99) peak currents vs. scan rate. (c) Semi-log plot of anodic E_{pa} (linear fit Y = 0.037*x - 0.23, R^2 = 0.97) and cathodic E_{pc} (linear fit Y = -0.046*x - 0.46, R^2 = 0.97) peak potential vs. scan rate. Error bars represent the standard deviation from 3 measurements using a different fiber electrode.

Dye stability is an essential criterion that needs to be evaluated first in order for the proposed probe to operate as designed. We've utilized different methods to evaluate the stability of dye immobilization on the electrode: 1) Active cycling through cyclic voltammetry in the test solution, 2) active pipetting to mimic the perturbation of heparin spiking with pipette, during which gentle pipette near the electrode was performed, wait for 1 minute, then acquire the SWV signal, 3) passive loss by just immersing the electrode in the test solution. Active cycling dye stability of different dyes was evaluated through 20 CV cycles active cleaning as shown in **Figure 4.10**. The peak current after cycling in 1xPBS drops to 97%, 85%, 80%, and 83% for NB, Azure A, MB and TBO respectively. NB shows the highest stability in 1xPBS due to the extra benzene ring that reduce its solubility.

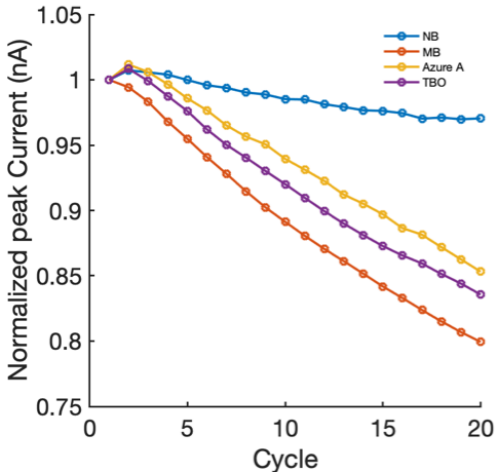

Figure 4.10. Normalized peak current change over 20 CV cycles active cleaning in PBS solution.

Next, dye stability was tested in plasma solution where we noticed a higher loss through pipetting near the electrode surface over multiple SWV measurements. As shown in **Figure 4.11a**, the peak current drops to nearly 30% over 50 times pipetting in the solution over 2 hours period. The decay rate gradually decreases over time and could be fit with a one phase decay equation: Y = 0.879*exp(-0.05*X+0.22). We also noticed that the loss could not be completely eliminated even after overnight incubation of the electrode in the plasma, hoping to reach a saturation point (**Figure 4.11b**). This indicates the fundamental noise floor of our measurement system using the electrochemical station, as well as the baseline loss inherent with the dye immobilization techniques. In order to reach a heparin responsive sensor, we need to either further minimize this loss, or to increase the dye sensitivity towards heparin.

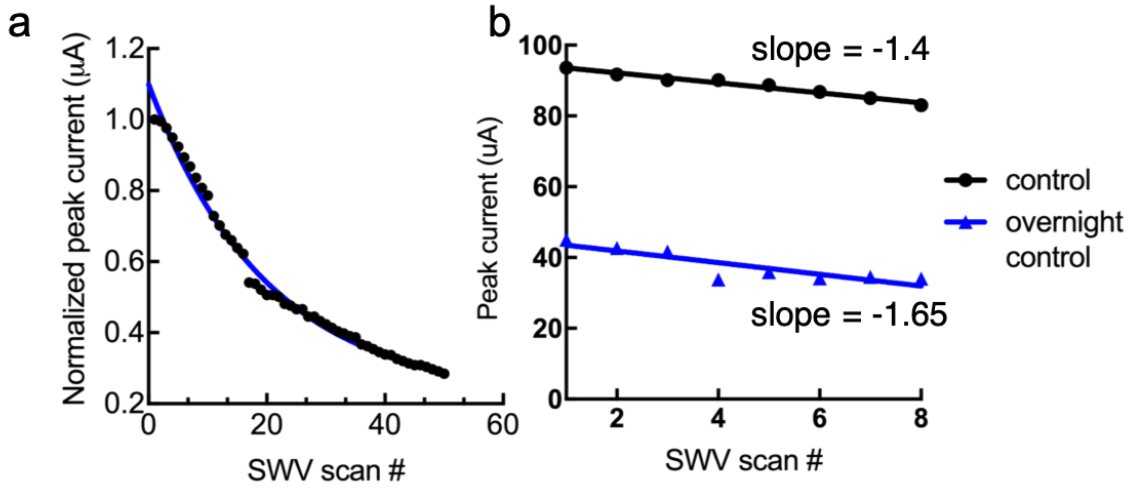

Figure 4.11. (a) Normalized peak current change in plasma over 50 times pipetting shows a decreasing loss rate. (b) Peak current response for pipetting control, and pipetting control after overnight incubation.

4.4 Agarose gel coating for dye immobilization

4.4.1 Materials and Experimental part

Agarose gel was prepared at 0.1 wt% in 10 x PBS buffer solution. The gel was extruded from a syringe tube into a microfluidics tubing of different diameters. The Fiber electrode was fabricated as in previous section and then inserted in the microfluidics tubing and the assembly was cooled down at 4-degree C for 15 mins for gelation. PEDOT: PSS was deposited through electro polymerization as described in the previous section on the agar coated electrode.

4.4.2 Results and Discussion

Dye immobilization methods and stability within the agarose gel were first investigated and summarized in the **Table 4.1**. The direct dye/agarose mixing approach has the lowest resting stability and the dye would leach out immediately after immersing in the buffer solution.

Next, using cyclic voltammetry to incorporate dye was investigated with and without the PEDOT coating. As shown in **Figure 4.12**, the fiber electrode with PEDOT coating shows

Table 4.1. Dye loading methods and stability

	Method	Resting stability	Cycling stability
a. Direct dye/agarose mixing	0.5mM AzureA was mixed with hot agarose directly and then cast on the fiber electrode for gelation	-	/
b. Active dye loading on gel with cyclic voltammetry without PEDOT: PSS	0.5 mM AzureA was loaded on to the agarose gel through 20 cycles cyclic voltammetry at 0.1 v/s	+	-
c. Passive dye loading on gel with PEDOT: PSS	PEDOT: PSS was electropolymerized on the agarose gel encapsulated fiber electrode first. The electrode was then immersed in 0.5 mM AzureA solution for 20 mins for dye loading	+	-
d. Active dye loading on gel with PEDOT: PSS with cyclic voltammetry	PEDOT: PSS was electropolymerized on the agarose gel encapsulated fiber electrode first, then 0.5 mM Azure A was loaded through 20 cycles cyclic voltammetry at 0.1 v/s	++	+

a darker color after 20 CV cycles of dye loading and remains a similar color after 20 CV cycles cleaning in the PBS solution. While the fiber electrode without PEDOT coating shows poor cycling stability and the color was completely lost after 20 cycles cleaning in PBS. This result suggests that PEDOT:PSS film plays two roles in our probe design: 1) facilitate ion transport from solution to the agarose gel, 2) stabilize the dye within the agarose gel after immobilized, likely due to the negatively charged PSS molecules incorporated in the matrix. We also hypothesized that the PEDOT:PSS was deposited within the gel matrix to stabilize the dye.

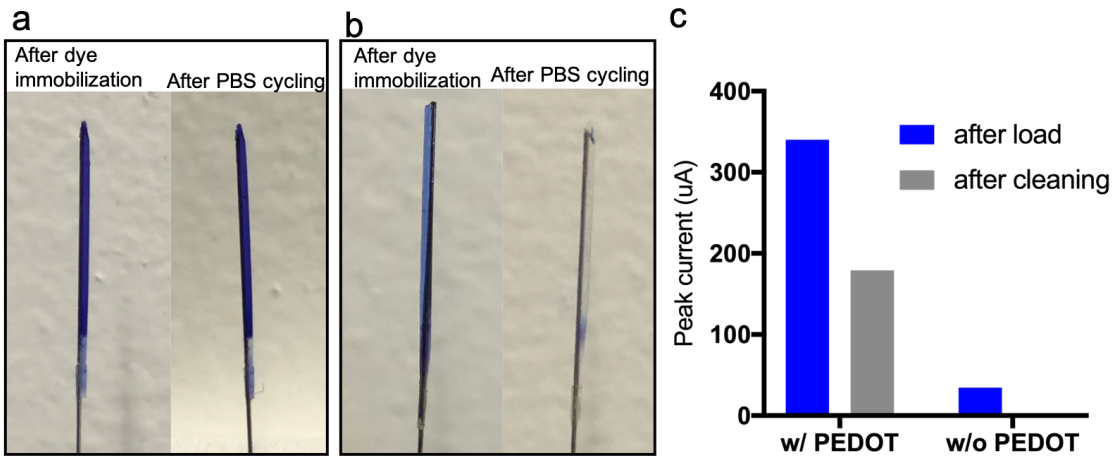

Figure 4.12. Immobilized dye stability in agarose gel. (a) PEDOT deposition within the agarose gel before and after 20 CV cycles cleaning in the PBS solution. (b) No PEDOT deposition within the agarose gel before and after PBS cleaning. (c) SWV peak current of the fiber electrode in the PBS solution before and after PBS cleaning shows that fiber electrode with PEDOT coating has 10x higher peak current after loading and better cycling stability after cleaning.

Next, loading efficiency using thick and thin agarose gel as well as active or passive loading were evaluated. As shown in **Figure 4.13**, thick-gel probe takes longer time to incorporate the dye near the electrode surface. Even though the thick-gel probe shows a similar color, the SWV peak current is only about 11% of the thin-gel probe which indicates most of the dye are distributed in the gel matrix far from the electrode surface, which is expected since the electrochemistry is only the readout of redox reaction at the electrode surface. Passive loading by immersing the gel-probe in dye solution for 20 minutes was also evaluated and the SWV peak current is about 17% of the active loading method. This result shows that potential sweeping plays a critical role to provide the drive force for effective and time-efficient dye loading into the gel matrix.

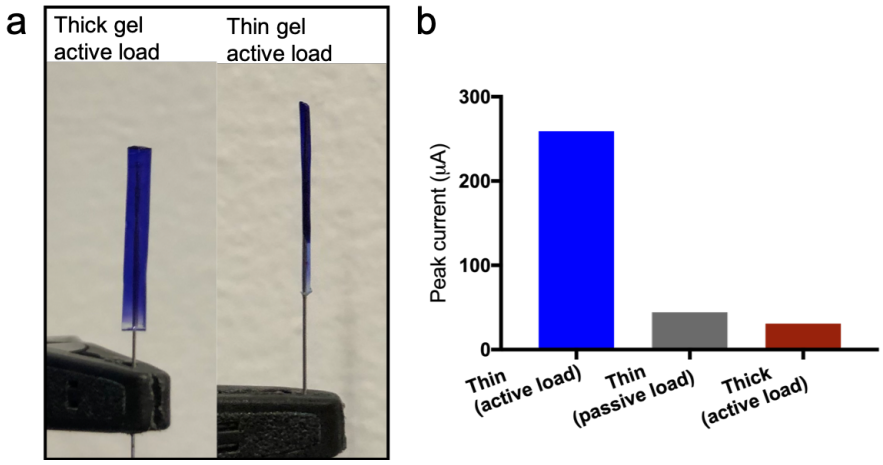

Figure 4.13. (a) Thick and thin agarose gel loaded with dye through 20 CV cycles. (b) SWV peak current of the fiber electrode after dye loading in the PBS solution.

The prepared agarose gel coated electrodes with Azure A dye immobilzied were stored in 1xPBS solution and the incorporated dye was stable with reserved color up to 2 weeks. The response to heparin was then tested with photoacoustic imaging as shown in **Figure 4.14a**. The heparin-dye aggregate have a higher photoacoustic activity and the change in photoacoustic signal can be correlated with the amount of heparin added. **Figure 4.14c** indicates that the thin-gel probe has a linear response to heparin in the range of 1 U/mL ~ 5 U/mL ($Y = 0.1881*X+1.833$, $p = 0.0017$) and higher sensitivity compare to the thick-gel probe. This suggests that the dye incorporated in the gel matrix is not completely charge compensated and still remains certain degree of freedom for binding with the heparin.

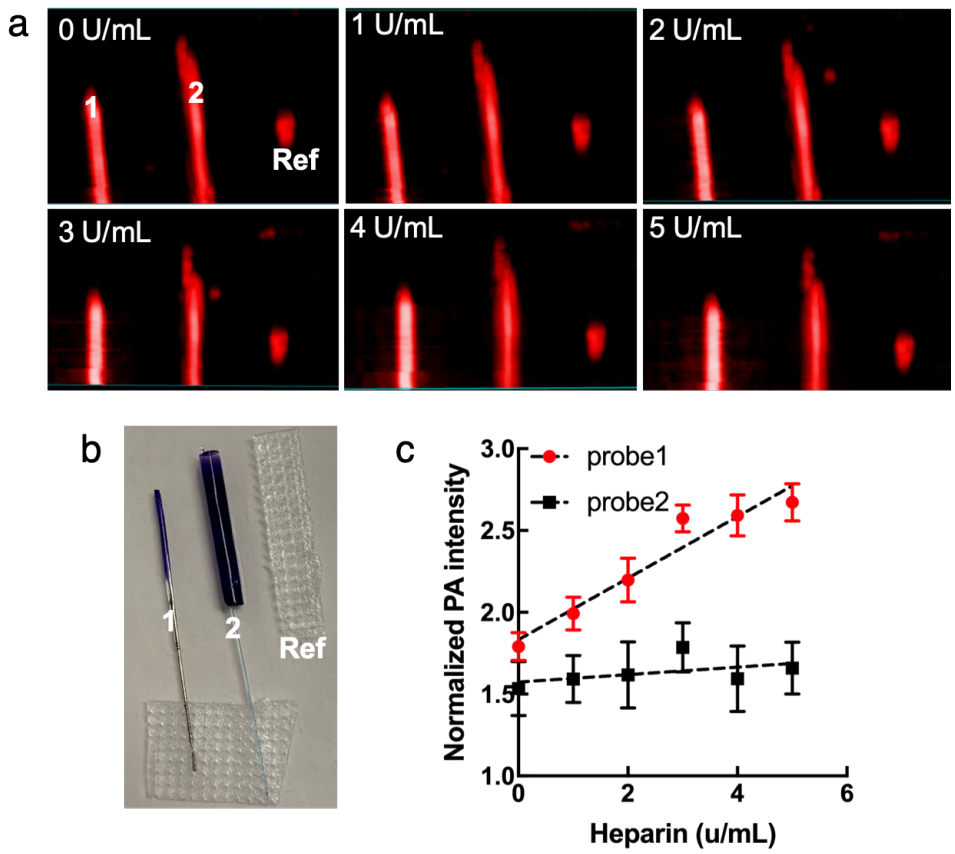

Figure 4.14. (a) Photoacoustic images of two agarose gel coated fiber shows that the photoacoustic response increased with increasing amounts of heparin. (b) Photo of the two probes tested with PA. A graphite stick was used as reference point for intensity normalization. (c) Normalized photoacoustic intensity as a function of heparin concentration.

4.5 Conclusion

In this chapter, we used the electrostatic binding between cationic dyes and heparin for electrochemical sensing of heparin. First, 7 cationic dyes in free solution were tested using GCE electrode to understand the electrochemical response of the heparin-dye binding. Decreasing SWV peak current was observed for all dyes confirmed the heparin-dye binding which decrease the concentration of free electroactive dyes for electron transfer. Among all the dyes, Azure A shows the highest sensitivity and linear response to heparin in plasma. Nile

Blue shows the largest linear response dynamic range in buffer solution. MB and TBO are only sensitive to heparin in solution above 4 U/mL. We've also noticed a hematocrit level dependent response for Azure A in whole blood.

We then introduced using multi-cycle cyclic voltammetry to active incorporate cationic dye molecules on the electrode surface using a porous conductive polymer coating. Increasing peak current during the progressive cycling indicates the dye adsorption process. Electrochemical kinetic study of the dye immobilized electrode suggests fast electron transfer due to the conductive polymer matrix that facilitates ion transport and electron transfer. Immobilized dye stability was also evaluated using different matrix. Among all the dyes, NB molecules shows the highest stability in PBS solution likely due to the extra benzene ring that reduce its solubility. While in plasma, loss through pipetting cannot be completely eliminated due to the inherent system noise and dye instability. Further measurements to increase dye stability in plasma solution such as ion-selective polymer coating could be applied.

At last, Agarose gel offers a versatile platform for dye incorporation that could also maintain the degree of freedom of the dye for heparin binding. Different loading methods were evaluated, and the results suggest that PEDOT coating is an important factor for stabilizing the dye in the agarose gel matrix. Active coating through cyclic voltammetry also facilitates the mass transfer for effective dye incorporation into the gel matrix. The gel-electrode prepared was stable up to two weeks and was sensitive to heparin validated through photoacoustic imaging.

Chapter 5

Conclusion

We leveraged the unique light interaction and physical property of the nano/micro fiber optics to construct miniaturized sensing platforms. In this dissertation, I detailed three such platforms using optical wave guides of different dimensions for chemical or nanomechanical sensing.

In chapter 2, a nanofiber optic force transducer was introduced. The transducer is based on a sharp decaying optical field of the SnO_2 nanofiber. The distance dependent scattering could be transformed to force detection using a compressible polymer cladding acting as a pseudo-spring. The nanomechanical event detection was evaluated using a PZT disk as the acoustic source. We were able to capture a acoustic power of ˜ 163 pW actuating on the transducer. We also proposed a free-standing structure to further transform the proposed transducer for more versatile applications.

In chapter 3, utilizing micro fiber optic, a multifunctional electro-optical microprobe for neurotransmitter detection was introduced. We were able to achieve a LOD of 800 nM, and 1.2 μM for dopamine and serotonin respectively. The microprobe of a coaxial structure with both optical and electrical pathway was able to acquire highly localized spectroelectrochemical recording. We also applied PEDOT:PSS coating that could significantly enhance the electrochemical property of the microprobe with antifouling merits. We were able to demonstrate the multimodality of the probe through microfiber based spectroelectrochemical platform for various redox active species.

In chapter 4, I used the electrostatic binding between cationic dyes and heparin for the detection of heparin. I constructed a microfiber electrode that has a flexible and small foot print that is ideal for in situ measurement. After investigating the cationic dye and heparin interaction electrochemically, I then applied porous PEDOT:PSS coating along with the cyclic voltammetry to actively immobilize these sensing dye molecules on the surface. Different dye immobilization strategy were evaluated and discussed. While the 2D immobilization impose certain limiations on our sensing limit, we further use agarose gel coating to immobilize dye in a 3D matrix that has increased dye degree of freedom. The sensitivity towards heparin was then validated through photoacoustic imaging.

Bibliography

[1] G. Keiser and P. P. Shum, "Review of diverse optical fibers used in biomedical research and clinical practice Review of diverse optical fibers used in biomedical research and clinical practice,"

[2] S. Korposh, S. W. James, S. W. Lee, and R. P. Tatam, "Tapered Optical Fibre Sensors: Current Trends and Future Perspectives," *Sensors (Basel, Switzerland)*, vol. 19, no. 10, 2019.

[3] D. Littlejohn, D. Lucas, and L. Han, "Bent silica fiber evanescent absorption sensors for near-infrared spectroscopy," *Applied Spectroscopy*, vol. 53, no. 7, pp. 845–849, 1999.

[4] M. Ahmad and L. L. Hench, "Effect of taper geometries and launch angle on evanescent wave penetration depth in optical fibers," *Biosensors and Bioelectronics*, vol. 20, no. 7, pp. 1312–1319, 2005.

[5] P. Wang, L. Zhang, Y. Xia, L. Tong, X. Xu, and Y. Ying, "Polymer Nano fi bers Embedded with Aligned Gold Nanorods: A New Platform for Plasmonic Studies and Optical Sensing," pp. 8–13, 2012.

[6] M. Ghandehari and C. S. Vimer, "Fiber optic evanescent field sensors for pH monitoring in civil infrastructure," *Nondestructive Evaluation and Health Monitoring of Aerospace Materials and Civil Infrastructures*, vol. 4704, no. June 2002, pp. 196–205, 2002.

[7] P. K. Choudhury and T. Yoshino, "On the pH response of fiber optic evanescent field absorption sensor having a U-shaped probe: An experimental analysis," *Optik (Jena)*, vol. 114, no. 1, pp. 13–18, 2003.

[8] K. Miyajima, G. Itabashi, T. Koshida, K. Tamari, D. Takahashi, T. Arakawa, H. Kudo, H. Saito, K. Yano, K. Shiba, and K. Mitsubayashi, "Fluorescence immunoassay using an optical fiber for determination of Dermatophagoides farinae (Der f1)," *Environmental Monitoring and Assessment*, vol. 182, no. 1-4, pp. 233–241, 2011.

[9] A. Asanov, A. Zepeda, and L. Vaca, "A platform for combined dna and protein microarrays based on total internal reflection fluorescence," *Sensors*, vol. 12, no. 2, pp. 1800–1815, 2012.

[10] B. D. Gupta and R. K. Verma, "Surface plasmon resonance-based fiber optic sensors: Principle, probe designs, and some applications," *Journal of Sensors*, vol. 2009, 2009.

[11] W. Wang, Z. Mai, Y. Chen, J. Wang, L. Li, Q. Su, X. Li, and X. Hong, "A label-free fiber optic SPR biosensor for specific detection of C-reactive protein," *Scientific Reports*, vol. 7, no. 1, pp. 1–8, 2017.

[12] T. Hu, Y. Zhao, and A. n. Song, "Fiber optic SPR sensor for refractive index and temperature measurement based on MMF-FBG-MMF structure," *Sensors and Actuators, B: Chemical*, vol. 237, pp. 521–525, 2016.

[13] L. Lu, Z. Jiang, Y. Hu, H. Zhou, G. Liu, Y. Chen, Y. Luo, and Z. Chen, "A portable optical fiber SPR temperature sensor based on a smart-phone," *Optics Express*, vol. 27, no. 18, p. 25420, 2019.

[14] R. Tabassum, S. K. Mishra, and B. D. Gupta, "Surface plasmon resonance-based fiber optic hydrogen sulphide gas sensor utilizing Cu-ZnO thin films," *Physical Chemistry Chemical Physics*, vol. 15, no. 28, pp. 11868–11874, 2013.

[15] B. H. Lee, Y. H. Kim, K. S. Park, J. B. Eom, M. J. Kim, B. S. Rho, and H. Y. Choi, "Interferometric fiber optic sensors," *Sensors*, vol. 12, no. 3, pp. 2467–2486, 2012.

[16] W. Lutang and N. Fang, "Applications of Fiber-Optic Interferometry Technology in Sensor Fields in Sensor Fields," *Intech*, vol. i, no. tourism, p. 38, 2012.

[17] U. Utzinger and R. R. Richards-Kortum, "Fiber optic probes for biomedical optical spectroscopy," *Journal of Biomedical Optics*, vol. 8, no. 1, p. 121, 2003.

[18] I. J. Bigio, S. G. Bown, G. Briggs, C. Kelley, S. Lakhani, D. Pickard, P. M. Ripley, I. G. Rose, and C. Saunders, "Diagnosis of breast cancer using elastic-scattering spectroscopy: preliminary clinical results," *Journal of Biomedical Optics*, vol. 5, no. 2, p. 221, 2000.

[19] U. Utzinger, M. Brewer, E. Silva, D. Gershenson, R. C. Blast, M. Follen, and R. Richards-Kortum, "Reflectance spectroscopy for in vivo characterization of ovarian tissue," *Lasers in Surgery and Medicine*, vol. 28, no. 1, pp. 56–66, 2001.

[20] D. C. O. Pickard, G. M. Briggs, C. Saunders, S. Lakhani, P. M. Ripley, I. J. Bigio, and S. G. Bown, "Elastic scattering spectroscopy in vivo: optical biopsies of cancers of the breast and GI tract," *Optical Biopsy III*, vol. 3917, no. April 2000, pp. 67–74, 2000.

[21] P. Farzam, E. M. Buckley, P. Y. Lin, K. Hagan, P. E. Grant, T. E. Inder, S. A. Carp, and M. A. Franceschini, "Shedding light on the neonatal brain: Probing cerebral hemodynamics by diffuse optical spectroscopic methods," *Scientific Reports*, vol. 7, no. 1, pp. 1–10, 2017.

[22] L.-w. Lo, P.-j. Tsai, S. H.-y. Huang, W.-y. Chen, Y.-t. Wang, C.-h. Chang, and C.-s. Yang, "In Vivo Monitoring of Fluorescent Nanosphere Delivery in Anesthetized Rats Using an Implantable Fiber-Optic Microprobe," vol. 77, no. 4, pp. 4465–4471, 2005.

[23] S. Ohayon, A. Caravaca-Aguirre, R. Piestun, and J. J. DiCarlo, "Minimally invasive multimode optical fiber microendoscope for deep brain fluorescence imaging," *Biomedical Optics Express*, vol. 9, no. 4, p. 1492, 2018.

[24] X. I. N. Guo, Y. Ying, and L. Tong, "Photonic Nanowires: From Subwavelength Waveguides to Optical Sensors XIN," *Accounts of chemical research*, vol. 47, no. 2, 2013.

[25] G. Brambilla, G. S. Murugan, J. S. Wilkinson, and D. J. Richardson, "Optical manipulation of microspheres along a subwavelength optical wire," *Optics Letters*, vol. 32, no. 20, p. 3041, 2007.

[26] J. Yu, R. Feng, and W. She, "Low-power all-optical switch based on the bend effect of a nm fiber taper driven by outgoing light," *Optics Express*, vol. 17, no. 6, p. 4640, 2009.

[27] Y. Xu, W. Fang, and L. Tong, "Real-time control of micro/nanofiber waist diameter with ultrahigh accuracy and precision," *Optics Express*, vol. 25, no. 9, p. 10434, 2017.

[28] F. X. Gu and L. M. Tong, "Polymer single-nanowire for optical humidity sensing," *2008 1st Asia-Pacific Optical Fiber Sensors Conference, APOS 2008*, pp. 2007–2009, 2008.

[29] X. Yu, S. Zhang, M. Olivo, and N. Li, "Micro/Nano-Fiber Probes for Optical Sensing, Imaging, and Stimulation in Biomedical Applications," *Photonics Research*, vol. 8, no. 11, 2020.

[30] R. Yan, D. Gargas, and P. Yang, "Nanowire photonics," *Nature Photonics*, vol. 3, no. 10, pp. 569–576, 2009.

[31] F. Gu, L. Zhang, X. Yin, and L. Tong, "Polymer Single-Nanowire Optical Sensors 2008," 2008.

[32] W. Cao and Y. Duan, "Optical fiber-based evanescent ammonia sensor," *Sensors and Actuators, B: Chemical*, vol. 110, no. 2, pp. 252–259, 2005.

[33] Z. Zhang, J. Pan, Y. Tang, Y. Xu, L. Zhang, Y. Gong, and L. Tong, "Optical micro/nanofibre embedded soft film enables multifunctional flow sensing in microfluidic chips," *Lab on a Chip*, vol. 20, no. 14, pp. 2572–2579, 2020.

[34] W. Kaim and J. Fiedler, "Spectroelectrochemistry: The best of two worlds," *Chemical Society Reviews*, vol. 38, no. 12, pp. 3373–3382, 2009.

[35] L. León and J. D. Mozo, "Designing spectroelectrochemical cells: A review," *TrAC - Trends in Analytical Chemistry*, vol. 102, pp. 147–169, 2018.

[36] T. P. Deangelis and W. R. Heineman, "An electrochemical experiment using an optically transparent thin layer electrode," *Journal of Chemical Education*, vol. 53, no. 9, pp. 594–597, 1976.

[37] D. Ibañez, E. C. Romero, A. Heras, and A. Colina, "Dynamic Raman spectroelectrochemistry of single walled carbon nanotubes modified electrodes using a Langmuir-Schaefer method," *Electrochimica Acta*, vol. 129, pp. 171–176, 2014.

[38] J. Garoz-Ruiz, J. V. Perales-Rondon, A. Heras, and A. Colina, "Spectroelectrochemical Sensing: Current Trends and Challenges," *Electroanalysis*, vol. 31, no. 7, pp. 1254–1278, 2019.

[39] S. E. Andria, C. J. Seliskar, and W. R. Heineman, "Spectroelectrochemical sensing based on multimode selectivity simultaneously achievable in a single device. 21. Selective chemical sensing using sulfonated polystyrene-blockpoly(ethylene-ran-butylene)block-polystyrene thin films," *Analytical Chemistry*, vol. 81, no. 23, pp. 9599–9606, 2009.

[40] T. Shtoyko, O. D. Stuart, and H. N. Gray, "Spectroelectrochemical sensing of aqueous iron: An experiment for analytical chemistry," *Journal of Chemical Education*, vol. 84, no. 9, pp. 1467–1470, 2007.

[41] K. Imai, T. Okazaki, N. Hata, S. Taguchi, K. Sugawara, and H. Kuramitz, "Simultaneous Multiselective Spectroelectrochemical Fiber-Optic Sensor: Demonstration of the Concept Using Methylene Blue and Ferrocyanide," 2015.

[42] B. M. Beam, N. R. Armstrong, and S. B. Mendes, "An electroactive fiber optic chip for spectroelectrochemical characterization of ultra-thin redox-active films," *Analyst*, vol. 134, no. 3, pp. 454–459, 2009.

[43] J. Garoz-Ruiz, D. Izquierdo, A. Colina, S. Palmero, and A. Heras, "Optical fiber spectroelectrochemical device for detection of catechol at press-transferred single-walled carbon nanotubes electrodes," *Analytical and Bioanalytical Chemistry*, vol. 405, no. 11, pp. 3593–3602, 2013.

[44] A. Colina, "Spectroelectrochemistry at Screen-Printed Electrodes: Determination of Dopamine," 2012.

[45] K. C. Neuman and A. Nagy, "Single-molecule force spectroscopy: optical tweezers, magnetic tweezers and atomic force microscopy," *Nature Methods*, vol. 5, no. 6, pp. 491–505, 2008.

[46] J. Zlatanova, S. Lindsay, and S. Leuba, "Single molecule force spectroscopy in biology using the atomic force microscope," *Progress in Biophysics and Molecular Biology*, vol. 74, pp. 37–61, 7 2000.

[47] T. T. Perkins, "Optical traps for single molecule biophysics: A primer," *Laser and Photonics Reviews*, vol. 3, no. 1-2, pp. 203–220, 2009.

[48] A. La Porta and M. D. Wang, "Optical torque wrench: Angular trapping, rotation, and torque detection of quartz microparticles," *Physical Review Letters*, vol. 92, no. 19, pp. 9–12, 2004.

[49] J. R. Moffitt, Y. R. Chemla, S. B. Smith, and C. Bustamante, "Recent advances in optical tweezers," *Annual Review of Biochemistry*, vol. 77, pp. 205–228, 2008.

[50] C. Zensen, N. Villadsen, F. Winterer, S. R. Keiding, and T. Lohmüller, "Pushing nanoparticles with light - A femtonewton resolved measurement of optical scattering forces," *APL Photonics*, vol. 1, no. 2, 2016.

[51] O. M. Maragò, P. H. Jones, P. G. Gucciardi, G. Volpe, and A. C. Ferrari, "Optical trapping and manipulation of nanostructures," *Nature Nanotechnology*, vol. 8, no. 11, pp. 807–819, 2013.

[52] A. Ohlinger, A. Deak, A. A. Lutich, and J. Feldmann, "Optically trapped gold nanoparticle enables listening at the microscale," *Physical Review Letters*, vol. 108, no. 1, pp. 1–5, 2012.

[53] E. Evans, K. Ritchie, and R. Merkel, "Sensitive force technique to probe molecular adhesion and structural linkages at biological interfaces," *Biophysical Journal*, vol. 68, no. 6, pp. 2580–2587, 1995.

[54] D. R. Stabley, C. Jurchenko, S. S. Marshall, and K. S. Salaita, "Visualizing mechanical tension across membrane receptors with a fluorescent sensor," *Nature Methods*, vol. 9, no. 1, pp. 64–67, 2012.

[55] C. Grashoff, B. D. Hoffman, M. D. Brenner, R. Zhou, M. Parsons, M. T. Yang, M. A. McLean, S. G. Sligar, C. S. Chen, T. Ha, and M. A. Schwartz, "Measuring mechanical tension across vinculin reveals regulation of focal adhesion dynamics," *Nature*, vol. 466, no. 7303, pp. 263–266, 2010.

[56] Q. Z. Yang, Z. Huang, T. J. Kucharski, D. Khvostichenko, J. Chen, and R. Boulatov, "A molecular force probe," *Nature Nanotechnology*, vol. 4, no. 5, pp. 302–306, 2009.

[57] F. Meng, T. M. Suchyna, and F. Sachs, "A fluorescence energy transfer-based mechanical stress sensor for specific proteins in situ," *FEBS Journal*, vol. 275, no. 12, pp. 3072–3087, 2008.

[58] Q. Huang, J. Lee, F. T. Arce, I. Yoon, P. Angsantikul, J. Liu, Y. Shi, J. Villanueva, S. Thamphiwatana, X. Ma, L. Zhang, S. Chen, R. Lal, and D. J. Sirbuly, "Nanofibre optic force transducers with sub-piconewton resolution via near-field plasmon–dielectric interactions," *Nature Photonics*, vol. 11, no. May, pp. 1–5, 2017.

[59] M. Law, D. J. Sirbuly, J. C. Johnson, J. Goldberger, R. J. Saykally, and P. Yang, "Nanoribbon Waveguides for Subwavelength Photonics Integration," vol. 305, no. August, 2004.

[60] Z. W. Pan, Z. R. Dai, and Z. L. Wang, "Nanobelts of Semiconducting Oxides," *Science*, vol. 291, no. March, pp. 1947–1950, 2001.

[61] D. J. Sirbuly, M. Law, H. Yan, and P. Yang, "Semiconductor nanowires for subwavelength photonics integration," *Journal of Physical Chemistry B*, vol. 109, no. 32, pp. 15190–15213, 2005.

[62] I. Yoon, K. Kim, S. E. Baker, D. Heineck, S. C. Esener, and D. J. Sirbuly, "Stimulus-responsive light coupling and modulation with nanofiber waveguide junctions," *Nano Letters*, vol. 12, no. 4, pp. 1905–1911, 2012.

[63] B. Knoll and F. Keilmann, "Enhanced dielectric contrast in scattering-type scanning near-field optical microscopy," *Optics Communications*, vol. 182, no. 4-6, pp. 321–328, 2000.

[64] Q. Huang, F. Teran Arce, J. Lee, I. Yoon, J. Villanueva, R. Lal, and D. J. Sirbuly, "Gap controlled plasmon-dielectric coupling effects investigated with single nanoparticle-terminated atomic force microscope probes," *Nanoscale*, vol. 8, no. 39, pp. 17102–17107, 2016.

[65] C. Picart, "Polyelectrolyte Multilayer Films: From Physico-Chemical Properties to the Control of Cellular Processes," *Current Medicinal Chemistry*, vol. 15, no. 7, pp. 685–697, 2008.

[66] L. Dunsch, "Recent Advances in in situ multi-spectroelectrochemistry," *Journal of Solid State Electrochemistry*, vol. 15, no. 7-8, pp. 1631–1646, 2011.

[67] V. Gribova, R. Auzely-Velty, and C. Picart, "Polyelectrolyte multilayer assemblies on materials surfaces: From cell adhesion to tissue engineering," *Chemistry of Materials*, vol. 24, no. 5, pp. 854–869, 2012.

[68] C. A. Ghiorghita, F. Bucatariu, and E. S. Dragan, "Influence of cross-linking in loading/release applications of polyelectrolyte multilayer assemblies. A review," *Materials Science and Engineering C*, vol. 105, no. July, p. 110050, 2019.

[69] L. Richert, A. J. Engler, D. E. Discher, C. Picart, and L. Pasteur, "Elasticity of Native and Cross-Linked Polyelectrolyte Multilayer Films," pp. 1908–1916, 2004.

[70] R. Servaty, J. Schiller, H. Binder, and K. Arnold, "Hydration of polymeric components of cartilage - An infrared spectroscopic study on hyaluronic acid and chondroitin sulfate," *International Journal of Biological Macromolecules*, vol. 28, no. 2, pp. 121–127, 2001.

[71] E. K. Dimitriadis, F. Horkay, J. Maresca, B. Kachar, and R. S. Chadwick, "Determination of elastic moduli of thin layers of soft material using the atomic force microscope.," *Biophysical journal*, vol. 82, no. 5, pp. 2798–2810, 2002.

[72] G. Francius, J. Hemmerlé, J. Ohayon, P. Schaaf, J. C. Voegel, C. Picart, and B. Senger, "Effect of crosslinking on the elasticity of polyelectrolyte multilayer films measured by colloidal probe AFM," *Microscopy Research and Technique*, vol. 69, no. 2, pp. 84–92, 2006.

[73] Y. Wang, H. Yuan, X. Liu, Q. Bai, H. Zhang, Y. Gao, and B. Jin, "A Comprehensive Study of Optical Fiber Acoustic Sensing," *IEEE Access*, vol. 7, pp. 85821–85837, 2019.

[74] F. Guo, T. Fink, M. Han, L. Koester, J. Turner, and J. Huang, "High-sensitivity, high-frequency extrinsic Fabry–Perot interferometric fiber-tip sensor based on a thin silver diaphragm," *Optics Letters*, vol. 37, no. 9, p. 1505, 2012.

[75] L. Liu, P. Lu, S. Wang, X. Fu, Y. Sun, D. Liu, J. Zhang, H. Xu, and Q. Yao, "UV adhesive diaphragm-based FPI sensor for very-low-frequency acoustic sensing," *IEEE Photonics Journal*, vol. 8, no. 1, pp. 1–10, 2016.

[76] Q. Dong, H. Bae, Z. Zhang, Y. Chen, Z. Wen, D. A. Olson, M. Yu, and H. Liu, "Miniature Fiber Optic Acoustic Pressure Sensors with Air-Backed Graphene Diaphragms," *Journal of Vibration and Acoustics, Transactions of the ASME*, vol. 141, no. 4, pp. 1–19, 2019.

[77] B. F. Matarèse, J. Lad, C. Seymour, P. N. Schofield, and C. Mothersill, "Bio-acoustic signalling; exploring the potential of sound as a mediator of low-dose radiation and stress responses in the environment," *International Journal of Radiation Biology*, vol. 0, no. 0, pp. 1–43, 2020.

[78] M. Matsuhashi, A. N. Pankrushina, S. Takeuchi, H. Ohshima, H. Miyoi, K. Endoh, K. Murayama, H. Watanabe, S. Endo, M. Tobi, Y. Mano, M. Hyodo, T. Kobayashi, T. Kaneko, S. Otani, S. Yoshimura, A. Harata, and T. Sawada, "Production of sound waves by bacterial cells and the response of bacterial cells to sound," *Journal of General and Applied Microbiology*, vol. 44, no. 1, pp. 49–55, 1998.

[79] A. Fridberger and M. Ulfendahl, "Acute mechanical overstimulation of isolated outer hair cells causes changes in intracellular calcium levels without shape changes," *Acta Oto-Laryngologica*, vol. 116, no. 1, pp. 17–24, 1996.

[80] L. E. Kinsler, A. R. Frey, A. B. Coppens, and J. V. Sanders, *Fundamentals of Acoustics*, vol. 113. 1999.

[81] A. Tricoli, N. Nasiri, and S. De, "Wearable and Miniaturized Sensor Technologies for Personalized and Preventive Medicine," *Advanced Functional Materials*, vol. 27, no. 15, 2017.

[82] Y. Lechasseur, S. Dufour, G. Lavertu, C. Bories, M. Deschênes, and R. Vallée, "Nature Methods A microprobe for parallel optical and electrical recordings from single neurons in vivo,"

[83] C. Chatard, A. Sabac, L. Moreno-Velasquez, A. Meiller, and S. Marinesco, "Minimally Invasive Microelectrode Biosensors Based on Platinized Carbon Fibers for in Vivo Brain Monitoring," *ACS Central Science*, vol. 4, no. 12, pp. 1751–1760, 2018.

[84] A. S. Sadek, R. B. Karabalin, J. Du, M. L. Roukes, C. Koch, and S. C. Masmanidis, "Wiring nanoscale biosensors with piezoelectric nanomechanical resonators," *Nano Letters*, vol. 10, no. 5, pp. 1769–1773, 2010.

[85] A. Y. Zhu, F. Yi, J. C. Reed, H. Zhu, and E. Cubukcu, "Optoelectromechanical multimodal biosensor with graphene active region," *Nano Letters*, vol. 14, no. 10, pp. 5641–5649, 2014.

[86] Siddharth, A. N. Patel, T. P. Jung, and T. J. Sejnowski, "A Wearable Multi-Modal Bio-Sensing System Towards Real-World Applications," *IEEE Transactions on Biomedical Engineering*, vol. 66, no. 4, pp. 1137–1147, 2019.

[87] J. M. Savitt, V. L. Dawson, T. M. Dawson, J. M. Savitt, V. L. Dawson, and T. M. Dawson, "Diagnosis and treatment of Parkinson disease : molecules to medicine Find the latest version : Science in medicine Diagnosis and treatment of Parkinson disease : molecules to medicine," vol. 116, no. 7, pp. 1744–1754, 2006.

[88] A. G. Ludolph, J. Kassubek, K. Schmeck, C. Glaser, A. Wunderlich, A. K. Buck, S. N. Reske, J. M. Fegert, and F. M. Mottaghy, "Dopaminergic dysfunction in attention deficit hyperactivity disorder (ADHD), differences between pharmacologically treated and never treated young adults: A 3,4-dihdroxy-6-[18F]fluorophenyl-l-alanine PET study," *NeuroImage*, vol. 41, no. 3, pp. 718–727, 2008.

[89] R. Brisch, A. Saniotis, R. Wolf, H. Bielau, H. G. Bernstein, J. Steiner, B. Bogerts, K. Braun, J. Kumaratilake, M. Henneberg, and T. Gos, "The role of dopamine in schizophrenia from a neurobiological and evolutionary perspective: Old fashioned, but still in vogue," *Frontiers in Psychiatry*, vol. 5, no. APR, pp. 1–11, 2014.

[90] B. Dubois and B. Pillon, "Cognitive deficits in Parkinson's disease," *Journal of Neurology*, vol. 244, no. 1, pp. 2–8, 1996.

[91] M. Vaswani, F. K. Linda, and S. Ramesh, "Role of selective serotonin reuptake inhibitors in psychiatric disorders: A comprehensive review," *Progress in Neuro-Psychopharmacology and Biological Psychiatry*, vol. 27, no. 1, pp. 85–102, 2003.

[92] E. Bezard, C. E. Gross, and J. M. Brotchie, "Presymptomatic compensation in Parkinson's disease is not dopamine-mediated," *Trends in Neurosciences*, vol. 26, no. 4, pp. 215–221, 2003.

[93] I. N. Mefford, A. F. Oke, and R. N. Adams, "Regional distribution of ascorbate in human brain," *Brain Research*, vol. 212, no. 1, pp. 223–226, 1981.

[94] B. J. Venton and R. M. Wightman, "Psychoanalytical electrochemistry: Dopamine and behavior," *Analytical Chemistry*, vol. 75, no. 19, pp. 414–421, 2003.

[95] Y. Su, S. Bian, and M. Sawan, "Real-time in vivo detection techniques for neurotransmitters: a review," *The Analyst*, vol. 145, no. 19, pp. 6193–6210, 2020.

[96] T. Aosaki, M. Miura, T. Suzuki, K. Nishimura, and M. Masuda, "Acetylcholine-dopamine balance hypothesis in the striatum: An update," *Geriatrics and Gerontology International*, vol. 10, no. SUPPL. 1, 2010.

[97] C. He, M. Tao, C. Zhang, Y. He, W. Xu, Y. Liu, and W. Zhu, "Microelectrode-Based Electrochemical Sensing Technology for in Vivo Detection of Dopamine: Recent Developments and Future Prospects," *Critical Reviews in Analytical Chemistry*, vol. 0, no. 0, pp. 1–11, 2020.

[98] M. K. Zachek, P. Takmakov, J. Park, R. M. Wightman, and G. S. McCarty, "Simultaneous monitoring of dopamine concentration at spatially different brain locations in vivo," *Biosensors and Bioelectronics*, vol. 25, no. 5, pp. 1179–1185, 2010.

[99] M. L. Huffman and B. J. Venton, "Carbon-fiber microelectrodes for in vivo applications," *Analyst*, vol. 134, no. 1, pp. 18–24, 2009.

[100] A. D. Vizva, "A novel carbon tipped single micro-optrode for combined optogenetics and electrophysiology," pp. 1–22, 2018.

[101] S. D. Niyonambaza, P. Kumar, P. Xing, J. Mathault, P. D. Koninck, E. Boisselier, M. Boukadoum, and A. Miled, "A Review of neurotransmitters sensing methods for neuro-engineering research," *Applied Sciences (Switzerland)*, vol. 9, no. 21, pp. 1–31, 2019.

[102] D. L. Robinson, A. Hermans, A. T. Seipel, and R. M. Wightman, "Monitoring Rapid Chemical Communication in the Brain," pp. 2554–2584, 2008.

[103] S. S. Fuglerud, K. Milenko, A. Aksnes, and D. R. Hjelme, "Surface-enhanced absorption spectroscopy for optical fiber sensing," *Materials*, vol. 13, no. 1, pp. 1–13, 2020.

[104] K. C. Liao, T. Hogen-Esch, F. J. Richmond, L. Marcu, W. Clifton, and G. E. Loeb, "Percutaneous fiber-optic sensor for chronic glucose monitoring in vivo," *Biosensors and Bioelectronics*, vol. 23, no. 10, pp. 1458–1465, 2008.

[105] B. A. Flusberg, E. D. Cocker, W. Piyawattanametha, J. C. Jung, E. L. Cheung, and M. J. Schnitzer, "Fiber-optic fluorescence imaging," *Nature Methods*, vol. 2, no. 12, pp. 941–950, 2005.

[106] F. S. Alfonso, Y. Zhou, E. Liu, A. F. McGuire, Y. Yang, H. Kantarci, D. Li, E. Copenhaver, J. B. Zuchero, H. Müller, and B. Cui, "Label-free optical detection of bioelectric potentials using electrochromic thin films," *Proceedings of the National Academy of Sciences of the United States of America*, vol. 117, no. 29, pp. 17260–17268, 2020.

[107] H. Kuramitz, A. Piruska, H. B. Halsall, C. J. Seliskar, and W. R. Heineman, "Simultaneous multiselective spectroelectrochemical sensing of the interaction between protein and its ligand using the redox dye Nile blue as a label," *Analytical Chemistry*, vol. 80, no. 24, pp. 9642–9648, 2008.

[108] K. L. Knoche, C. Hettige, P. D. Moberg, S. Amarasinghe, and J. Leddy, "Cyclic Voltammetric Diagnostics for Inert, Uniform Density Films," *Journal of The Electrochemical Society*, vol. 160, no. 6, pp. H285–H293, 2013.

[109] M. Ganji, A. T. Elthakeb, A. Tanaka, V. Gilja, E. Halgren, and S. A. Dayeh, "Scaling Effects on the Electrochemical Performance of poly(3,4-ethylenedioxythiophene (PEDOT), Au, and Pt for Electrocorticography Recording," *Advanced Functional Materials*, vol. 27, no. 42, pp. 1–12, 2017.

[110] M. Shen and M. L. Colombo, "Analytical Methods Electrochemical nanoprobes for the chemical detection of neurotransmitters," pp. 7095–7105, 2015.

[111] B. J. Venton, K. P. Troyer, and R. M. Wightman, "Response times of carbon fiber microelectrodes to dynamic changes in catecholamine concentration," *Analytical Chemistry*, vol. 74, no. 3, pp. 539–546, 2002.

[112] S. Sharma, N. Singh, V. Tomar, and R. Chandra, "A review on electrochemical detection of serotonin based on surface modified electrodes," *Biosensors and Bioelectronics*, vol. 107, no. February, pp. 76–93, 2018.

[113] P. Hashemi, E. C. Dankoski, J. Petrovic, R. B. Keithley, and R. M. Wightman, "Voltammetric detection of 5-hydroxytryptamine release in the rat brain," *Analytical Chemistry*, vol. 81, no. 22, pp. 9462–9471, 2009.

[114] A. Mendoza, T. Asrat, F. Liu, P. Wonnenberg, and A. G. Zestos, "Carbon nanotube yarn microelectrodes promote high temporal measurements of serotonin using fast scan cyclic voltammetry," *Sensors (Switzerland)*, vol. 20, no. 4, 2020.

[115] A. G. Zestos, C. B. Jacobs, E. Trikantzopoulos, A. E. Ross, and B. J. Venton, "Polyethylenimine carbon nanotube fiber electrodes for enhanced detection of neurotransmitters," *Analytical Chemistry*, vol. 86, no. 17, pp. 8568–8575, 2014.

[116] S. Demuru and H. Deligianni, "Surface PEDOT : Nafion Coatings for Enhanced Dopamine , Serotonin and Adenosine Sensing," vol. 164, no. 14, pp. 129–138, 2017.

[117] B. L. Hanssen, S. Siraj, and D. K. Wong, "Recent strategies to minimise fouling in electrochemical detection systems," *Reviews in Analytical Chemistry*, vol. 35, no. 1, pp. 1–28, 2016.

[118] B. Duran and G. M. Swain, "Electrochemical Activation of Diamond Microelectrodes : Implications for the In Vitro Measurement of Serotonin in the Bowel microelectrodes : implications for the in vitro," no. May, 2014.

[119] P. Takmakov, M. K. Zachek, R. B. Keithley, P. L. Walsh, C. Donley, G. S. McCarty, and R. M. Wightman, "Carbon microelectrodes with a renewable Surface," *Analytical Chemistry*, vol. 82, no. 5, pp. 2020–2028, 2010.

[120] G. Garcia-Belmonte, Z. Pomerantz, J. Bisquert, J. P. Lellouche, and A. Zaban, "Analysis of ion diffusion and charging in electronically conducting polydicarbazole films by impedance methods," *Electrochimica Acta*, vol. 49, no. 20, pp. 3413–3417, 2004.

[121] P. Ferloni, M. Mastragostino, and L. Meneghello, "Impedance analysis of electronically conducting polymers," *Electrochimica Acta*, vol. 41, no. 1, pp. 27–33, 1996.

[122] R. Hass, J. García-Cañadas, and G. Garcia-Belmonte, "Electrochemical impedance analysis of the redox switching hysteresis of poly(3,4-ethylenedioxythiophene) films," *Journal of Electroanalytical Chemistry*, vol. 577, no. 1, pp. 99–105, 2005.

[123] M. R. Abidian and D. C. Martin, "Experimental and theoretical characterization of implantable neural microelectrodes modified with conducting polymer nanotubes," *Biomaterials*, vol. 29, no. 9, pp. 1273–1283, 2008.

[124] G. Sonmez, "Polymeric electrochromics," pp. 5251–5259, 2005.

[125] W. A. Gazotti, G. Casalbore-Miceli, S. Mitzakoff, A. Geri, M. C. Gallazzi, and M. A. De Paoli, "Conductive polymer blends as electrochromic materials," *Electrochimica Acta*, vol. 44, no. 12, pp. 1965–1971, 1999.

[126] A. S. Ribeiro and R. J. Mortimer, "Conjugated conducting polymers with electrochromic and fluorescent properties," *SPR Electrochemistry*, vol. 13, pp. 21–49, 2016.

[127] A. Savva, S. Wustoni, and S. Inal, "Ionic-to-electronic coupling efficiency in PEDOT:PSS films operated in aqueous electrolytes," *Journal of Materials Chemistry C*, vol. 6, no. 44, pp. 12023–12030, 2018.

[128] A. Ejaz, M. M. Ahmed, A. Tasleem, M. R. Khan Niazi, M. F. Ahsraf, I. Ahmad, A. Zakir, and A. Raza, "Thromboprophylaxis in Intensive Care Unit Patients: A Literature Review," *Cureus*, vol. 10, no. 9, 2018.

[129] J. Hirsh and V. Fuster, "Guide to anticoagulant therapy. Part 1: Heparin," *Circulation*, vol. 89, no. 3, pp. 1449–1468, 1994.

[130] T. Baglin, T. W. Barrowcliffe, A. Cohen, and M. Greaves, "Guidelines on the use and monitoring of heparin," *British Journal of Haematology*, vol. 133, no. 1, pp. 19–34, 2006.

[131] T. W. Barrowcliffe, B. Mulloy, E. A. Johnson, and D. P. Thomas, "The anticoagulant activity of heparin: Measurement and relationship to chemical structure," *Journal of Pharmaceutical and Biomedical Analysis*, vol. 7, no. 2, pp. 217–226, 1989.

[132] R. A. Wahking, R. H. Hargreaves, S. M. Lockwood, S. K. Haskell, and K. W. Davis, "Comparing Anti–Factor Xa and Activated Partial Thromboplastin Levels for Monitoring Unfractionated Heparin," *Annals of Pharmacotherapy*, vol. 53, no. 8, pp. 801–805, 2019.

[133] M. D. Lancé, "A general review of major global coagulation assays: thrombelastography, thrombin generation test and clot waveform analysis," *Thrombosis Journal*, vol. 13:1, pp. 1–6, 2015.

[134] F. I. J. J. Bowers J, "The use of activated clotting times to monitor heparin therapy during and after interventional procedures," *Clinical cardiology*, pp. 357–361, 1994.

[135] M. A. Smythe, J. Priziola, P. P. Dobesh, D. Wirth, A. Cuker, and A. K. Wittkowsky, "Guidance for the practical management of the heparin anticoagulants in the treatment of venous thromboembolism," *Journal of Thrombosis and Thrombolysis*, vol. 41, no. 1, pp. 165–186, 2016.

[136] R. C. Gosselin, J. H. King, K. A. Janatpour, W. E. Dager, E. C. Larkin, and J. T. Owings, "Comparing direct thrombin inhibitors using aPTT, ecarin clotting times, and thrombin inhibitor management testing," *Annals of Pharmacotherapy*, vol. 38, no. 9, pp. 1383–1388, 2004.

[137] L. Tan, S. Yao, and Q. Xie, "Electrochemical determination of heparin using methylene blue probe and study on competition of Ba 2 + with methylene blue for binding heparin," *Talanta*, vol. 71, pp. 827–832, 2007.

[138] H. Y. Huo, H. Q. Luo, and N. B. Li, "Electrochemical sensor for heparin based on a poly(thionine) modified glassy carbon electrode," *Microchimica Acta*, vol. 167, no. 3-4, pp. 195–199, 2009.

[139] S. N. Ding, J. F. Chen, J. Xia, Y. H. Wang, and S. Cosnier, "Voltammetric detection of heparin based on anion exchange at electropolymeric film of pyrrole-alkylammonium cationic surfactant and MWCNTs composite," *Electrochemistry Communications*, vol. 34, pp. 339–343, 2013.

[140] L. Tian, H. Zhao, Z. Zhao, J. Zhai, and Z. Zhang, "A facile voltammetric method for detection of heparin in plasma based on the polyethylenimine modified electrode," *Analytical Methods*, vol. 11, no. 10, pp. 1324–1330, 2019.

[141] A. Rengaraj, Y. Haldorai, S. K. Hwang, E. Lee, M. W. Oh, T. J. Jeon, Y. K. Han, and Y. S. Huh, "A protamine-conjugated gold decorated graphene oxide composite as an electrochemical platform for heparin detection," *Bioelectrochemistry*, vol. 128, pp. 211–217, 2019.

[142] F. Meng, W. Liang, H. Sun, L. Wu, X. Gong, and P. Miao, "A Peptide-Based Electrochemical Biosensor for Facile Measurement of Whole-Blood Heparin," *ChemElectroChem*, vol. 4, no. 3, pp. 472–475, 2017.

[143] N. Ramamurthy, N. Baliga, J. A. Wahr, U. Schaller, V. C. Yang, and M. E. Meyerhoff, "Improved protamine-sensitive membrane electrode for monitoring heparin concentrations in whole blood via protamine titration," *Clinical Chemistry*, vol. 44, no. 3, pp. 606–613, 1998.

[144] Y. Yoshimi, Y. Yagisawa, R. Yamaguchi, and M. Seki, "Blood heparin sensor made from a paste electrode of graphite particles grafted with molecularly imprinted polymer," *Sensors and Actuators, B: Chemical*, vol. 259, pp. 455–462, 2018.

[145] G. N. Lim and A. E. Ross, "Purine functional group type and placement modulate the interaction with carbon-fiber microelectrodes," *ACS Sensors*, vol. 4, no. 2, pp. 479–487, 2019.

[146] E. Laviron, "General expression of the linear potential sweep voltammogram in the case of diffusionless electrochemical systems," *Journal of Electroanalytical Chemistry*, vol. 101, no. 1, pp. 19–28, 1979.

[147] A. L. Eckermann, D. J. Feld, J. A. Shaw, and T. J. Meade, "Electrochemistry of redox-active self-assembled monolayers," *Coordination Chemistry Reviews*, vol. 254, no. 15-16, pp. 1769–1802, 2010.

[148] H.-h. L. Iu, M. Z. Hang, and D.-w. P. Ang, "Electrochemical Properties of Nile Blue Covalently Immobilized on Self-assembled Thiol-monolayer Modified Gold Electrodes," *ANALYTICAL SCIENCES*, vol. 18, pp. 1339–1344, 2002.

[149] A. Malinauskas, T. Ruzgas, and L. Gorton, "Electrochemical study of the redox dyes Nile Blue and Toluidine Blue adsorbed on graphite and zirconium phosphate modified graphite," *Journal of Electroanalytical Chemistry*, vol. 484, no. 1, pp. 55–63, 2000.